分光反射率データベースの構築と皮膚組織における光吸収の評価への応用

Construction of Spectral Reflectance Database and its Application to the Evaluation of Light Absorption in Skin Tissue

Dissertation Submitted for the degree of
Doctor of Engineering
December 2020

by
Kaustav Das

Division of Engineering, Doctor's Course
Muroran Institute of Technology
Muroran, Hokkaido, Japan

CONTENTS

Chapter 1

Introductory Remarks

1.1 General Review for Tissue Optics

In recent years, the use of light for clinical diagnostics and therapeutic medicine has been attracted as the non-invasive technique and, thus, various optical methods have been studied. The visible to near-infrared light propagated through the biological tissue is strongly influenced by many chromophores within the tissue. Human skin is a typical example of such biological object. There are many chromophores in the skin tissue such as melanin, carotene, bilirubin, hemoglobin, and so on. These chromophores are related to physiological conditions of the tissue and, have their own optical absorption properties. For example, the color of venous and arterial blood is different in an oxygen state. The pigmentation or tanning of skin is caused by the multiplication of melanin due to the physiological response. Therefore, if the optical properties of the tissue can be successfully measured, the useful information on health states and metabolisms of living tissue can be obtained through the skin. Alternatively, the optical properties may be required to calculate the distribution of light in the tissue during photodynamic therapy or laser surgery. Thus, the optical techniques have a large potential in the biomedical field. In clinical situation, however, there are only a few reliable instruments based on optical methods. This is because the biological tissues are strongly scattering media and, thus, the determination of optical properties is generally difficult by the conventional optical methods such as the ray optics and attenuation according to the Lambert-Beer law. For this reason, various theories and methods have been studied to model the light

propagation in the tissue-like scattering media.

The quantitative distribution of light intensity in scattering media can be described from the solution of Chandrasekhar's radiative transfer equation [1] as,

$$\frac{dI(\mathbf{r},\mathbf{s})}{ds} = -(\mu_a + \mu_s)I(\mathbf{r},\mathbf{s}) + \frac{\mu_a + \mu_s}{4\pi}\int_{4\pi} p(\mathbf{s},\mathbf{s}')I(\mathbf{r},\mathbf{s}')\, d\Omega' \qquad (1.1)$$

where $I(\mathbf{r},\mathbf{s})$ is the intensity per unit solid angle at target location $\mathbf{r}$ in the direction $\mathbf{s}$ ($\mathbf{s}$ is the directional unit vector), μ_a and μ_s are the absorption coefficient and scattering coefficient of medium, respectively. $p(\mathbf{s},\mathbf{s}')$ is the scattering phase function, representing scattering contribution from the direction $\mathbf{s}$ to $\mathbf{s}'$, and $d\Omega'$ is the solid angle. The first term on the right-hand side of Eq. (1.1) represents the loss in $I(\mathbf{r},\mathbf{s})$ per unit length in direction $\mathbf{s}$ due to absorption and scattering. The second term describes the gain in $I(\mathbf{r},\mathbf{s})$ per unit length in direction $\mathbf{s}$ due to scattering from other scattered light $I(\mathbf{r},\mathbf{s}')$ $d\Omega'$ (i.e. light intensity confined in the elemental solid angle $d\Omega'$) from direction $\mathbf{s}'$.

This integro-differential equation expresses the rate of change in the intensity of a narrow incident light beam as a function of the optical properties of the medium involved. Although the radiative transfer theory gives a more adequate description of the distribution of light intensity in the optically turbid medium than does any other model, the general analytic solution is not known yet. However, there are some approximate analytical theories or numerical method in the following.

Diffusion Approximation. The diffusion approximation is obtained by considering the lowest-order approximation of the expansion in spherical harmonics of the radiative transfer equation. The diffusion approximation can be solved for homogeneous diffusing media for different boundary conditions such as infinitely extended medium, semi-infinite slab, finite slab, cylinder, and sphere. Theoretical studies of light propagation in the

multiple scattering media based on the diffusion approximation have been published by Ishimaru [2] and Furustu [3]. The solutions obtained well describe photon propagation when the distance of a detector from the source is larger than about 10 transport mean free paths.

Random Walk Method. The motion of a photon in the scattering medium is approximated as a random walk on a simple cubic lattice. The photon proceeds through the lattice as steps to one of six nearest neighboring lattice points. By using this simple scheme, it is possible to obtain analytical relationships similar to the ones obtained using the diffusion approximation [4].

Kubelka-Munk Theory. The Kubelka-Munk theory has been widely used to determine the absorption and scattering coefficients of turbid media. This theory considers the two opposite fluxes, and can be employed when the scattering is significantly dominant over the absorption. This model is not accurate for forward-directed scattering and complicated geometric media such as a biological tissue because the isotropic scattering is assumed in this theory. Recently, however, 3-, 4-, and 7-flux models are also studied as the special cases of the multi-flux theory [5-9]. Applying to the photon-tissue interactions, 3-flux model includes two diffuse fluxes (forward and backward) and collimated forward flux, and 7-flux model consists of six diffuse fluxes in 3D space and collimated forward flux.

Monte Carlo Method. The Monte Carlo method provides a physical simulation of photon propagation in the scattering medium. The model assumes a non-deterministic, stochastic nature for high scattering and absorption of individual photon [10,11]. By using a random number generating routine, the trajectories of emitted photons are chosen according to the statistical rules relevant for photon propagation through the medium.

The trajectory of any emitted photon is followed until it exits from the scattering medium or it arrives at the detector. The Monte Carlo method allows a full-dimensional description of photon propagation and the actual scattering properties of tissue can be taken into account in the simulation. The parameters of a scattering coefficient, absorption coefficient, and scattering phase function are usually required in this method. This Monte Carlo method requires the long computational time for the reliable results.

Various techniques based on the light propagation model mentioned above have been studied and reported for measuring the optical properties of tissue. They are roughly classified into the three types of measuring technique, the time-resolved measuring technique, the frequency-domain measuring technique, and the spatially resolved measuring technique. An outline of these types is briefly described in the following.

(i) Time-Resolved Measureing Technique

When an ultrashort light pulse (a few picoseconds long) is incident on the scattering medium such as tissues, the received pulse backscattered from, or transmitted thorough the medium is a few seconds long. This temporal spreading of a light pulse is called the temporal spreading function (TPSF) [12], and depends on the optical properties of the medium. Therefore, the TPSF can be used to acquire the absorption and scattering coefficients of tissues. The use of a source emitting ultrashort pulse (picosecond, femtosecond) and an ultrafast detector such as a streak camera makes possible a direct measurement of the TPSF of the received pulse, which is known as the time-resolved measurement. Chance *et al.* [13] have reported the usefulness of the time-resolved technique for measuring the oxygenation state in the brain. Delpy *et al.* [14], Wilson *et al.* [15], and Nomura *et al.* [16] also utilized the time-resolved technique for measuring

the optical properties of tissue. Patterson *et al.* [17] investigated the behavior of light in tissue by using the time-dependent diffusion approximation, whereas Hasegawa *et al.* [18] and Delpy *et al.* [14] employed the Monte Carlo method to analyze the time-resolved transmittance. Jacques [19] described light irradiance at various time intervals after impingement of femtosecond and picosecond light pulses using the Monte Carlo method.

In recent years, some researchers have reported on the possibility of the optical-computed tomography (CT) based on the time-resolved techniques numerically and experimentally. Ito *et al.* [20] have obtained an image of oxygenation change in a rat brain by using the optical-CT scanner based on the conventional X-ray CT algorithm. Araki and Nashimoto [21] developed a deconvolution technique using the point spread functions and succeeded in reconstruction of an optical-CT image experimentally. Using the time dependent diffusion equation, Arridge *et al.* [22] analytically and experimentally studied a reconstruction method as an inverse method. Singer *et al.* [23] proposed numerically a new algorithm for using the six-flux model for radiation and an iterative method for reconstruction. For the instrumentation of optical-CT, Yamada *et al.* [24, 25] have investigated the use of temporal variations of transmittance of a light impulse numerically.

(ii) Frequency-Domain Measuring Technique

Frequency-domain photon migration [FDPM] methods, in which the light source intensity is modulated at high frequency, have been successfully applied to *in vitro* spectroscopy studies of turbid media [26-30]. Analytical solutions to the frequency-domain standard diffusion equation (SDE) have been employed in these studies to deduce the absorption and scattering properties from the frequency-domain data acquired in the

optical turbid media. The frequency-domain SDE has been evaluated to be applicable to the study of thick, turbid, and macroscopically homogenous scattering media when the source-detector separation is typically greater than 1 cm and the source modulation frequency is less than 1 GHz [31]. Fishkin *et al.* [32] measured the optical properties of normal and malignant *in vivo* tissue by using the FDPM method.

(iii) Spatially Resolved Measuring Technique

When a narrow photon beam is incident on the homogeneous scattering medium, the radial dependence of backscattered light depends on the optical properties of the medium. The spatially resolved technique is based on this radial dependence of the diffuse reflectance from the scattering medium. Different physical models have been used to determine expressions for the dependence of the diffuse reflectance on radial distance from the incident point of light. Groenhuis *et al.* [33,34] utilized the diffusion theory to derive the Green's function for photon fluence resulting from an isotropic point source at depth in a semi-infinite tissue as an infinite sum of modified Bessel functions. Shmitt *et al.* [35] extended this approach to express the radial reflectance from a multi-layered tissue such as the skin. Wilson *et al.* [36] proposed the use of the relative reflectance curve to determine the tissue optical properties. Farrell *et al.* [37] conducted the spatially resolved measurement of diffuse reflectance by using the multiple fiber-optic detectors in contact with the tissue surface at varying distances from the source. To avoid the pressure due to the contact probe, Bolt and ten Bosch [38,39] introduced an alternative technique based on a remote, non-contact, video camera detector (video reflectometry). Jacques *et al.* [40] used this technique to measure the *ex vivo* tissue. Results obtained from the similar instrumentations have also been reported by Splinter *et al.* [41], Dogariu

and Asakura [42], and Kienle *et al.* [43]. More recently, Wang and Jacques [44] proposed the use of a laser beam with an oblique incidence to deduce the reduced scattering coefficient of a turbid medium. Lin *et al.* [45] extended this technique to measure the absorption coefficient and reduced scattering coefficient simultaneously.

Spectrophotometry over a broad range from visible to near-infrared wavelength has also become a common method to measure the reflectance spectra of tissue. Edwards *et al.* [46], Kuppenhiem *et al.* [47], Anderson and Parrish [48], and Feather *et al.* [49], employed the reflectance spectra to investigate the relation between the color of human skin and chromophores. Spectral feature analysis has been studied to evaluate the various physiological conditions of living tissue. Diffey *et al.* [50] have studied the vasoconstriction and erythema by using the numerical indices derived from the reflectance spectra of human skin. Dawson *et al.* [51] utilized the reflectance spectrophotometry for measurement of human skin tissue to characterize the spectral properties. Harrison *et al.* [52] also measured the oxygen saturation and concentration of hemoglobin in the human skin tissue during the tuberculin reaction by using the numerical indices based on the reflectance spectra. Marchesini *et al.* [53,54] and Wallace *et al.* [55] have studied the method to discriminate between benign and malignant lesion in the skin tissue by using features of reflectance spectra of human skin.

As the other spectral analysis, chemometrics have been studied for evaluating the chromophores in the skin tissue. Tsumura *et al.* [56] proposed a method using the independent component analysis of color images for visualizing spatial distributions of melanin and hemoglobin in the human skin. Shimada *et al.* [57-59] reported a method for predicting absorption spectra of skin tissue using the multiple regression analysis based on the modified Lambert-Beer law [60-63].

1.2 Motivation

Analysis of spectral reflectance of skin has been widely preferred as an integral part to obtain necessary knowledge of skin conditions and to some extent physiological conditions. As change in physiological and skin conditions [64-67] are believed to be responsible for alteration of chromophores concentration (mainly melanin, and oxygenated and deoxygenated hemoglobin) and tissue micro-structure, it leads to variation in spectral reflectance. Thus, it becomes essential to find some relation between spectral shape, chromophores and tissue morphology. Also, it is well known that melanin corresponds to absorption coefficient in epidermal layer and hemoglobin to absorption coefficients of dermal and subcutaneous layers. Although, such relations are difficult to analyze in general.

In regard to this, many researchers have utilized various methods to evaluate the connection between skin condition and spectral reflectance. For example, diffusion approximation [68,69], solution of radiative transfer equation using auxiliary function [70, 71], and most widely used statistical method including principal component analysis [72], independent component [56] analysis and multiple regression analysis [57-59, 73-76]. All of these method have the common drawback of fitting respective mathematical models to different skin conditions including healthy or normal to diseased or abnormal.

By referring to the idea of Zang *et. al.* [69] to use library-based spectral fitting for identification of optical property from measured spectra, in this dissertation a method has been proposed using spectral mining from database consisting of simulated spectra using a nine-layered skin tissue model. The method is used to evaluate mainly the change of absorption conditions in measured spectra, as change in absorption condition corresponds to change in chromophores concentration.

1.3 Synopsis of Contents

This dissertation is aimed at the investigation on evaluation of changing absorption property of measured spectra using spectral mining from database consisting of simulated spectral reflectance curves. This study can mainly be segregated into two parts. In the first part, construction of the spectral database is discussed including the numerical investigation on the database, In the second part, actual spectral measurements were carried out under some specific conditions in order to analyze mainly absorption property of measured spectra using spectral mining from the database. The fundamental theories and principles that are integral to this dissertation are introduced in the chapter 2.

Chapter 3 highlights the effect of a detecting aperture size on spectral reflectance measurement of human skin through numerical simulation and experiments. To do so, Monte Carlo simulation of light propagation in the nine-layered skin tissue model was employed to generate simulated spectral reflectance curves and photon fluence map, and spectrophotometric experiments was carried out using an optical setup with an integrating sphere. This particular study becomes functional for the study made in chapter 5, where spectra are measured from human subject in order to show the effectiveness of the spectral mining method.

Chapters 4 and 5 are assigned to the proposed method of spectral mining from the spectral reflectance database to analyze unknown optical parameters of measured spectra. In chapter 4, the construction of the database which consists of simulated spectra with varying absorption and scattering coefficients is discussed. To make the construction of database in a convenient way, absorption coefficients are made into two groups and scattering coefficients into three groups. This resulted in five types of spectral change in simulated spectra which are included in the database. Among the five types, two types

presented similar spectral change with different absorption and scattering coefficients, which leads to an ambiguity problem in the constructed database. The possibility of these five types is investigated numerically for spectral change in evaluating unknown optical parameters of measured spectra.

In chapter 5, the five types of spectral change in simulated spectra are validated by observing five types of spectral change in measured spectra from three-layered agarose-gel phantom. Pressure-cuff occlusion and hot water immersion experiments are carried out on human forearm to confirm the applicability to analysis of change in absorption coefficients of measured spectra as both the experiments are supposed to vary hemoglobin concentration or absorption coefficients in dermal and subcutaneous layers. Also, use of application based customized database is briefly described as a possible way to overcome the ambiguity of the original full-size database.

Chapter 6 provides an overall summary of the various results obtained by studies executed in this dissertation.

Chapter 2.

Fundamental Theories and Principles

2.1 Physiology and Anatomy of Human Skin

2.1.1 Introduction

The optical and visual properties of skin components at each level of our taxonomy differ significantly depending on their anatomical characteristics. For example, light scattering behaviors of cells and fibers depend on their sizes and shapes. Light propagation in the skin layers, i.e. the epidermis and the dermis, is very different since their structures, densities and thicknesses vary greatly. Reflection at the surface of skin is influenced by the morphological characteristics of fine wrinkles. The appearances of wrinkles themselves also depend on their morphological characteristics such as depth, width and density variations. Most of these optical and visual properties are different for different body regions and body parts since the anatomical characteristics of the lower-level components vary across the body. The above examples are used to convey the importance of understanding the anatomical properties of each of the skin components.

2.1.2 Cells Elements

Although skin is composed of various types of cellular level elements, cells, fibers and chromophores are of special relevance to us. This is because light scattering and absorption in these fundamental elements are the building blocks of the gross optical phenomena observed at the cellular level. Skin includes various types of cells. The main

cells are keratinocyte, fibroblast, fat cell, melanocyte and red blood cells. These cells are present in different locations and have different structures and functions. Keratinocytes are quantitatively the dominant constituent cells in the epidermis. These cells produce fibriform proteins called keratin which contribute to the rigidity of the outermost layer of skin.

Keratinocytes protect the body from the external environment, for instance from stimulation, friction and viruses, while retaining moisture. Keratinocytes can be further categorized into four types of cells based on their functions and structures: basal cells, prickle cells, granular cells and horny cells. Although these cells have the same origin, they have different shapes, functions and sub-cellular level elements called organelles. For example, the basal cell, which reproduces keratinocytes, is a cylindrical and soft living cell. On the other hand, the horny cell, which mainly acts as a protector from the external environment, is a very flat and hard dead cell in which most organelles are degenerate.

Fibroblasts are long and narrow cells present in the dermis, the second skin layer beneath the epidermis. They produce collagen and elastin fibers which are the primary constituents of the dermis.

Fat cells are quantitatively the most abundant cells of the dermis. These cells accumulate fat and their sizes vary according to the volume of fat contained in them. These cells do not absorb much light. On the other hand, melanocyte and erythrocyte cells, both of which contain chromophores, mainly absorb light.

Melanocytes carry melanin which is one of the main light-absorbing pigments in skin. There are generally 1,000 to 2,000 melanocytes in 1 mm2 of skin. This cell contains specialized organelles called melanosomes. When skin is exposed to sunlight,

melanosomes are activated and produce melanin. The density of melanosomes depends on the body region. For example, regions that are frequently exposed to sunlight, such as the face, have higher density than other regions.

Red blood cells are the carriers of hemoglobin, another light-absorbing pigment in skin. Red blood cells have biconcave structures. The diameter of an erythrocyte is approximately 5 μm. Red blood cells usually contain more than 300 mg/ml of hemoglobin and carry oxygen from the lungs to tissues and carbon dioxide from tissues to the lungs.

A typical cell is composed of a cell membrane and organelles such as nucleus, mitochondria, lysosome, cytoplasm, Gelid apparatus, endoplasmic reticulum, etc. The nucleus, which is the largest spherical organelle, ranges from 3 to 10 μm in size and is enclosed in a membrane called the nuclear envelope. The nucleus includes most of the DNA of a cell and serves as the storage area for genetic information. The mitochondrion is 0.5 to 1.5 μm in size and is an oval-shaped organelle composed of a double membrane. The mitochondrion generates energy from food. The cell membrane is the outermost layer of a cell and has a doubly-layered structure of lipids (bilayer membrane). The thickness of the cell membrane is approximately 15 nm.

2.1.3 Fibers Elements

Skin contains several types of fibers. Keratin, collagen and elastin will be considered here as typical types of fibers found in skin.

Keratin fibers are mainly found in the outer-level epidermal cells, including horny cells. These fibers protect the inner side of skin from the external environment. At the same time, they contribute to moisture-retention in skin by holding water. The length and diameter of these fibers depend on the amount of moisture they actually hold.

Collagen fibers are the main constituents of the dermis. They represent about 70% of the dermis in dry weight. These fibers form vast and tough networks providing the dermis with strength, tension and elasticity. A collagen fiber is 0.5 to 3 μm in diameter and has a very long shape. A collagen fiber has a hierarchical structure [77] and is essentially a bundle of smaller microcables called collagen fibrils. Collagen fibrils are 10 to 300 nm in diameter and many micrometers long. A collagen fibril is a bundle of triple stranded collagen molecules (about 1.5 nm in diameter [77, 78] and 300 nm long [78]), three polypeptide chains that are wrapped around each other as a triple helix. The structure of collagen fibers starts to denature around the age of thirty. Photo-damaging, which occurs with ultraviolet light in sunlight and due to smoking, also denature the structure of collagen fibers. These factors eventually cause morphological changes to the network of collagen fibers. This leads to loss of skin elasticity and finally induces wrinkling [79–83].

Elastin fibers are random coiled proteins that are also present in the dermis. These fibers are thinner than collagen bundles (1 to 3 μm in diameter [78]). They occupy 2 to 4% of the total weight of the dermis. An elastin fiber consists of two components–micro-fibrils and matrix elastin. The micro-fibrils are aggregated at the periphery of elastic fiber (10 to 12 nm thick) and are also present within elastin fibers as strands aligned along the longitudinal direction (15 to 80 nm thick) [78]. Elastin fibers provide skin with elasticity and resilience. Even though the volume of elastin fibers is much smaller than that of collagen fibers, elastin fibers also play an important role in providing structural support to the dermis. Similar to collagen fibers, aging and ultraviolet light degrade elastin fibers, which finally leads to wrinkling. Elastin fibers are extensible and return to their original shapes after stretching. This property is not found in collagen fibers [78].

2.1.4 Chromophores

Skin includes various types of light-absorbing chemical compounds called chromophores. Among these chromophores, melanin and hemoglobin are especially important for understanding the appearance of normal skin since they absorb light particularly in the visible wavelength range [84, 85].

Melanin is the dominant chromophore of the epidermis. It can also be found in hair. Melanin is first produced in melanosomes, then is diffused into the epidermal layer, and moves up towards the surface of skin while denaturing. Through this upward process, melanin changes its color from tan to white. Melanin is divided into two types, eumelanin and pheomelanin, depending on its chemical structure. Eumelanin is a black or dark brown chromophore usually found in dark hair and eyes. Pheomelanin is yellow or reddish brown chromophore that is observed in red hair and feathers. Usually, normal skin contains some amount of eumelanin. Therefore, in most studies on skin, “melanin” is referred to as “eumelanin” [86]. The physiological function of melanin is to protect the inside of skin by absorbing and scattering ultraviolet light. When exposed to sunlight, melanocytes start to produce melanin. This is the biological reaction that eventually makes our skin appear tanned. The color of skin depends on the fraction of the volume of the melanosomes. In the light colored skin of Caucasians, the fraction is only between 1 and 3%. In the skins of well-tanned Caucasians and Mediterraneans, the percentage increases to 11 to 16%. In dark colored African skin, it goes up to 43% [86].

Hemoglobin is a red colored chromophore found in erythrocytes. Hemoglobin represents 95% of the dry mass of an erythrocyte. Hemoglobin binds oxygen effectively and carries oxygen to all body site through vessels and capillaries. When hemoglobin contains oxygen, it is called oxy-hemoglobin. Otherwise, it is called deoxy-hemoglobin.

Usually, in the vein, more than 47% of the hemoglobin is oxy-hemoglobin [87]. Oxy-hemoglobin is a brighter shade of red than deoxy-hemoglobin.

2.2 Constitution of Skin Tissue

2.2.1 Introduction

Skin is the largest body organ and forms the interface between the human body and the environment. Some of its functions are thermo-regulation, protection, metabolic functions, and tactile sensitivity. Skin tissue varies in thickness according to body location and wear-and-tear and this thickness variation contributes to the overall skin reflectance. Skin represents about 12 to 16% of the total body mass and covers an area of about 1.2 to 2 m2 in adults [88]. Skin tissue is also different between men and women, being generally less thick in women. The stratum corneum layer of the epidermis exhibits the greatest variation in thickness: in thin skin there may be fewer than 10 cell layers in the stratum corneum compared to over 100 layers in thick skin. The overall skin structure is constructed from three main layers: the epidermis, dermis, and hypodermis, as shown in Fig. 2.1. Each structure provides a distinct role in the overall function of the skin. Skin reflectance is mainly determined by two pigments: melanin and hemoglobin. Skin optics have been investigated by several authors in medicine, biology, and biophysics [86–93], to name a few. As we will discuss, skin is a highly scattering media, i.e., scattering is much more important than absorption, and it also exhibits a strong forward scattering behavior. Skin models are complicated by the fact that skin is irregularly shaped, inhomogeneous, multi-layered, has anisotropic physical properties, and has hair follicles

and glands [87]. The next sections provide descriptions of the anatomy, physiology, and optics of the various skin layers. The interaction of light with skin plays a metabolic function since the action of light on a precursor compound in the skin produces Vitamin-D which has a role in calcium and phosphate metabolism [94].

Cellular level elements form the three different skin layers: epidermis, dermis and subcutaneous. These layers are composed of different types of cellular level elements. Hence, they are very different in terms of structure and function. As a result, they exhibit different types of light propagation.

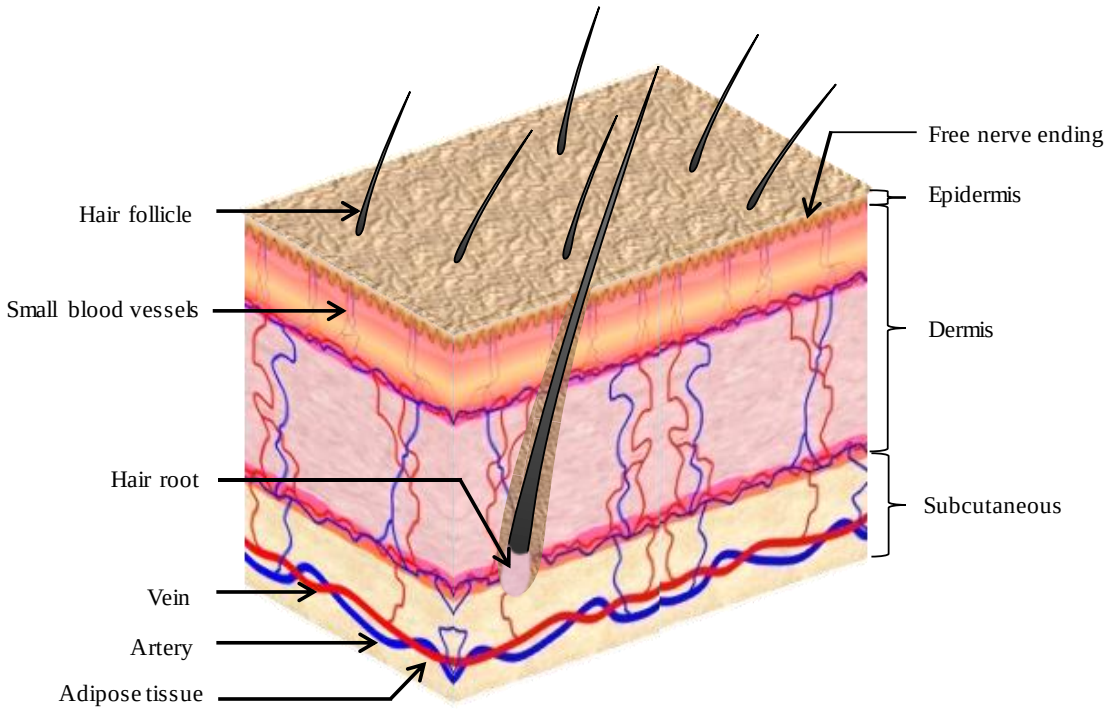

Fig. 2.1. A cross-sectional schematic diagram of skin. Skin is a complex multi-layered tissue consisting of various types of components, including veins, capillaries, hairs, cells, fibers, etc.

2.2.2 Epidermis

The epidermis is the outermost layer of skin. There are no veins and capillaries in this layer. Its thickness is about 0.2 mm on average and this thickness varies depending on the location on the body. Furthermore, the thickness also varies according to the volume of water that the epidermis holds.

The epidermis is further divided into five sublayers. From the bottom (innermost), these sublayers are *stratum basale* (basal cell layer), *stratum spinosum* (prickle cell layer), *stratum granulosum* (granular cell layer), *stratum lucidum* (clear layer) and *stratum corneum* (horny cell layer).

The epidermis is a metabolically active tissue. Keratinocytes produced in stratum basale move upward to the outer surface. This process is called turn-over. During this turn-over, keratinocytes change their structures and physiological functions. One cycle of this turn-over process takes about 28 days. In the following, we will describe the physio-anatomical properties of each sublayer.

Stratum basale (basal cell layer) is the deepest sublayer of the epidermis and is composed of a single layer of basal cells. This sublayer forms the boundary to the dermis. Keratinocytes are produced in this sublayer. It holds approximately 8% of the water in the epidermis. With aging, this layer becomes thinner and loses the ability to retain water. Melanocytes, which were mentioned in the previous section, also lie in this layer.

Stratum spinosum (prickle cell layer) refers to the 10 to 20 layers that lie on top of the basal cell layer. Basal cells, through the process of turn-over, make their shape somewhat flatter (multi-sided) and form these layers. These cells are called prickle cells and have little spines on the outside of their membrane. The thickness of this sublayer is typically from 50 to 150 μm [84].

Stratum granulosum (granular cell layer) is composed of 2 to 4 granular cell layers. The typical thickness is 3 μm [84]. In this sublayer, cornification called keratinization of keratinocytes begins. In this process, organelles such as nuclei and mitochondria start to resolve. Cells are increasingly filled with keratin fibers and contain less moisture than basal and prickle cell layers. The shape of these cells becomes much flatter during this process.

Stratum lucidum (clear layer) can only be found in soles and palms. It is a highly refractive sublayer. Its cells become flatter and more densely packed during turn-over.

Stratum corneum (horny cell layer) is the exterior sublayer of the epidermis. Its thickness ranges from 8 to 15 μm [84]. This sublayer is composed of several layers of hexagonal-shaped flat and hard cells named horny cells or corneocytes. These are dry dead cells without organelles and filled with keratin fibers. This sublayer prevents excessive dehydration of the skin tissue and usually contains 10 to 15% of the mass of water in the epidermis, depending on the skin condition. Horny cells are surrounded by intercellular lipids. A principal constituent is ceramide, which plays a crucial role in water retention [95]. Horny cells also contain special chemical compounds called natural moisturizing factor (NMF) that also plays an important role in retaining skin moisture. NMF is composed of sodium PCA, sphingolipids and ceramides, phospholipids, fatty acids, glycerol, squalane and cholesterol [95]. Skin that lacks NMF and ceramide tends to be very dry.

2.2.3 Dermis

The dermis is the second layer of skin, beneath the epidermal layer. This layer is much thicker than the epidermis (usually 1 to 4 mm [84]). The main components of the

dermis are collagen and elastin fibers. Compared to the epidermis, there are much fewer cells and much more fibers in the dermis. Dermis has the following two sublayers.

Papillary layer is the upper sublayer of the dermis that is clearly demarcated from the epidermis. This sublayer is a loosely connected tissue and includes a large amount of nerve fibers, capillaries, water and cells (e.g fibroblasts). In this sublayer, collagen fibers form a finer network than those of the reticular layer [96].

*Reticular laye*r constitutes the lower part of the dermis and represents a continuous transition to the subcutis. This sublayer has a denser and thicker network than the papillary layer and includes fewer nerve fibers and capillaries. In this sublayer, collagen fibers are aggregated into thick bundles which are mostly aligned parallel to the surface of skin [96].

The micro-anatomical complexity of skin, particularly in cell level, makes quantitative analysis of the optical properties of skin difficult. However, it can be significantly simplified by considering the physio-anatomical characteristics of each skin layers. As mentioned above, the epidermis and the dermis are very different in composition, thickness and functions. Hence, these two layers can be considered to be independent of each other in terms of optical behaviors. Indeed, the epidermis and the dermis are viewed as independent optical media in many early studies on skin optics. For example, melanin is present only in the epidermis. On the other hand, hemoglobin is found only in the dermis since there are no veins and capillaries in the epidermis. Hence, the epidermis can be essentially viewed as a melanin layer and the dermis can be viewed as a hemoglobin layer when analyzing the absorption properties of skin.

2.2.4 Subcutaneous Tissue

Subcutaneous tissue, or hypodermis in histology, is the third layer beneath the dermis. It is important to note that it is not categorized as another skin layer. Subcutaneous tissue is an elastic layer and includes a large amount of fat cells that work as a shock absorber for blood vessels and nerve endings. The thickness of this layer is reported to be 4 to 9 mm on average. However, the actual thickness differs from person to person and also depends on the body region.

2.2.5 Skin Layers

Skin is mainly composed of skin layers, fine wrinkles, hairs and skin surface lipids. Skin layers are the main component of skin. Fine wrinkles, hairs and skin surface lipids are observed on the outermost surface of skin. These components exhibit very different optical behaviors according to their structures. Skin layers usually consist of two different layers, the epidermis and the dermis. There is a very clear wavy boundary between these two layers. The thickness of the skin layers differs quite a bit depending on gender, age, individual, body regions, etc. It has been found that males tend to have thicker skin layers than females [97]. On the other hand, while several studies on the relation between age and the thickness of the skin layers have been reported [98–100], a clear relationship has not yet been found. Conditions of skin such as water-retention also differ depending on region, age and individual. For instance, skin layers of older people have less ability for water-retention, since the NMF tends to decrease with age. It has also been reported that the transparency of the stratum corneum (the outermost sublayer of the epidermis) decreases with the amount of water contained in it [101].

2.2.6 Hairs

Hairs behave as strong scatterers of light and affect the surface reflection of skin. Hairs are distributed all over the surface of the body except for the palms of the hands, the soles of the feet, the tops of the feet and mucocutaneous junctions [102, 103]. Hair grows from a hair follicle which resides in the dermal layer and opens onto the surface of skin. The bottom end of a hair follicle sits close to the boundary between the dermis and the subcutis. The color of hair is determined by the amount of eumelanin (dark brown) or pheomelanin (yellow reddish brown) it contains. Hair that does not contain melanin is white.

Hair can be categorized into two types – terminal thick hair and vellus fine hair. Terminal hair is usually hard and long. Examples include, the hair on the head, eyelashes, and eyebrows. Vellus hairs, sometimes called “peachy fuzz”, are soft and short (approximately 1 mm long). They can be found on the cheek, forehead, arms, etc. In body regions that are covered with vellus hair, the hair plays an important role in the visual appearance of the region.

2.2.7 Skin Surface Lipid

Skin surface lipid plays an important role in surface reflection from skin. It reflects incident light specularly and makes skin appearance shinier. Skin surface lipid can be observed in most body regions, but its volume varies from one region to another. Furthermore, it also varies with respect to gender, age, etc.

Skin surface lipid forms a thin film called the skin surface lipid film (SSLF) on skin layers. The SSLF protects excess evaporation of water from skin and keeps skin moisturized and smooth. The basis of the SSLF is sebum, which is a yellowish oily liquid

secreted by sebaceous glands. Sebaceous glands are present in the dermal layer and are connected to hair follicles. They cover a large region of the face, the middle of the back and the chest [102]. Although the contents of sebum vary depending on the body region, the composition of sebum is roughly estimated to be 30% of free fatty acid, 33% of triglycerides, 15% of wax, 5% of sterol esters, 5% of squalene and 7% of paraffin [104]. After sebum is secreted, it gets mixed with sweat and lipid. This results in an emulsified film over the surface of skin [104]. The SSLF spreads over the skin surface as an unevenly distributed amorphous sheet. The thickness of the SSLF varies from one body region to another and is roughly estimated to range from 0.01 to 2.1 μm [104]. The degree of sebum secretion depends on age, gender, body regions, etc. Sebum secretion starts to decrease from the mid-twenties and at the age of fifty becomes similar in degree to that in the case of a ten years old [104].

2.3 Optical Propagation Theory in Biological Tissue

2.3.1 Spectral Reflectance and Transmittance

The reflection is the return of radiation intensity by a surface, without a change in wavelength. The reflection is usually divided into two components, the specular reflection, in which the angle of incidence is equal to the angle of reflection, and diffuse reflection, in which the angle of incidence is not equal to the angle of reflection. Every surface returns both specular and diffuse reflections. Some surfaces may return mostly specular reflection, others more diffuse reflection. The glossier the surface, the more specular the reflection. Spectral reflectance is the ratio of the spectral radiant intensity or

luminous flux reflected in a given cone, whose apex is on the surface considered, to that reflected in the same directions by the perfect diffuser identically irradiated, and is expressed as

$$R(\lambda) = \frac{I_s(\lambda) - I_D(\lambda)}{I_R(\lambda) - I_D(\lambda)}, \tag{2.1}$$

where I_S is the sample intensity at wavelength λ, I_D is the dark intensity at wavelength λ, I_R is the reference intensity at wavelength λ.

The transmission is the percentage of the radiant intensity passing through a system considered relative to the amount that passes through the reference (such as air). The spectral transmittance is the ratio of the spectral transmitted radiant intensity or luminous flux to the incident flux under specified conditions of irradiation, is expressed as

$$T(\lambda) = \frac{I_s(\lambda) - I_D(\lambda)}{I_R(\lambda) - I_D(\lambda)}, \tag{2.2}$$

where I_S is the sample intensity at wavelength λ, I_D is the dark intensity at wavelength λ, I_R is the reference intensity at wavelength λ.

2.3.2 Lambert-Beer's Law

The absorbance spectrum $A(\lambda)$ is a measure of how light is absorbed by a absorbing sample such as a solution. The absorbance spectrum of a solution is related to the concentration of the absorber within it. This relationship is known as the Lambert-Beer law, and is given as

$$A(\lambda) = \log_{10}(1/T(\lambda)) = \varepsilon(\lambda) \cdot C \cdot l, \tag{2.3}$$

where $T(\lambda)$ is the transmittance spectrum, $\varepsilon(\lambda)$ is the molar extinction coefficient of

absorbers at wavelength λ, C is the molar concentration of absorber, and l is the optical pathlength.

2.3.3 Spectrocolorimetry

Spectrocolorimetry [105, 106] is a typical method for calculating the colorimetric value from the measured spectral power, reflectance, or transmittance. The most popular color system is the CIEXYZ color system [105, 106], which recommended by Commission Internationale de l'Éclairage, CIE. In this color system, the tristimulus values, X, Y, and Z corresponding to so-called **R** (red), **G** (green), and **B** (blue), respectively, are treated as the colorimetric values. For the surface color of an object, these tristimulus values are expressed as

$$X = K\sum S(\lambda)\cdot\bar{x}(\lambda)\cdot R(\lambda), \tag{2.4}$$

$$Y = K\sum S(\lambda)\cdot\bar{y}(\lambda)\cdot R(\lambda), \tag{2.5}$$

$$Z = K\sum S(\lambda)\cdot\bar{z}(\lambda)\cdot R(\lambda), \tag{2.6}$$

where $S(\lambda)$ and $R(\lambda)$ denote the spectral power distribution of illuminant and spectral reflectance of object, respectively. $\bar{x}(\lambda)$, $\bar{y}(\lambda)$, and $\bar{z}(\lambda)$ are the color matching functions [105, 106] as shown in Fig. 2.2. The values of the constant K which results in Y being equal to 100 for the perfect diffuser is given by

$$K = 100/\sum S(\lambda)\cdot\bar{y}(\lambda). \tag{2.7}$$

In Eqs. (2.4)-(2.7), the summation can be carried out using data at every 20 nm, from 400 to 700 nm. For the most applications, it is necessary to take values either at every 10 nm, or preferably at every 5 nm, and use a rage of wavelengths from 380 to 780 nm.

The retina of human eye varies considerably in its properties from one point to

another, and matches if the field size is altered. If the field size is reduced, the ability to discriminate one color from another becomes less marked. Hence, 2º matches tend to break down. For this reason, CIE recommended a different set of color matching functions for the samples having field sizes greater than 4º. These supplementary color matching functions, $\bar{x}_{10}(\lambda)$, $\bar{y}_{10}(\lambda)$, and $\bar{z}_{10}(\lambda)$, are also shown in Fig. 2.2. It can be seen that the two sets of functions are similar, but the differences are large enough to be significant. The $\bar{x}_{10}(\lambda)$, $\bar{y}_{10}(\lambda)$, and $\bar{z}_{10}(\lambda)$ functions can be used as weighting functions to obtain the tristimulus values X_{10}, Y_{10}, and Z_{10}, by means of procedures analogous to those adopted to obtain X, Y, and Z. All measures are distinguished by the presence of a subscript 10. The tristimulus value Y represents the percentage luminance factor, and this is an approximate correlation of the perceptual attribute of lightness. The values then range from 100 for white, or transparent objects, that absorb no light, to zero for objects that absorb all the light. It is sometimes convenient to use the ratio Y/Y_n, where Y_n is the value of Y for a suitable chosen reference white or reference transparent specimen. If the reference object absorbs some light, as is usually the case, Y/Y_n will be slightly more that 1 for the perfect diffuser.

The CIE *x*-*y* chromaticity diagram and the CIE 1976 uniform chromaticity scale diagram have many uses. However, as they show only proportions of the tristimulus values and not their actual magnitudes, they are only strictly spplicable to color all having the same luminance. In general, colors differ in both chromaticity and luminance, and therefore, some method of combining these variables is required. To meet this need for luminance factor (but not for luminance), the CIE has recommended the use of one of two alternative color spaces, CIELUV color space and CIELAB color space [105, 106]. Here, only CIELAB color space shown in Fig. 2.3 is described. It is produced by plotting along

three axes at right angles to one another as,

$$L^* = 116(Y/Y_n)^{1/3} - 16 \qquad \text{for } Y/Y_n > 0.008856, \tag{2.8}$$

$$L^* = 903.3(Y/Y_n) \qquad \text{for } Y/Y_n \le 0.008856, \tag{2.9}$$

$$a^* = 500\left[(X/X_n)^{1/3} - (Y/Y_n)^{1/3}\right], \tag{2.10}$$

$$b^* = 200\left[(Y/Y_n)^{1/3} - (Z/Z_n)^{1/3}\right], \tag{2.11}$$

where X_n, Y_n, and Z_n are the tristimulus value of perfect diffuser, and is equal to or less than 0.008856.

The CIELAB color space is intended to apply to object colors of the same size and shape, viewed in identical white to mid-gray surroundings, by an observer photopically adapted to a field of chromaticity not too different from that of average daylight. If the samples considered have an angular substance greater than 4º, then X_{10}, Y_{10}, and Z_{10} should be used instead of X, Y, and Z.

If the differences between two colors in L^*, a^*, and b^*, respectively, the total color difference ΔE^*_{ab} may be evaluated as

$$\Delta E^*_{ab} = \left[(\Delta L^*)^2 + (\Delta a^*)^2 + (\Delta b^*)^2\right]^{1/2}. \tag{2.12}$$

Thus, the value of ΔE^*_{ab} is equal to the distance between the two points representing the color in the CIELAB color space.

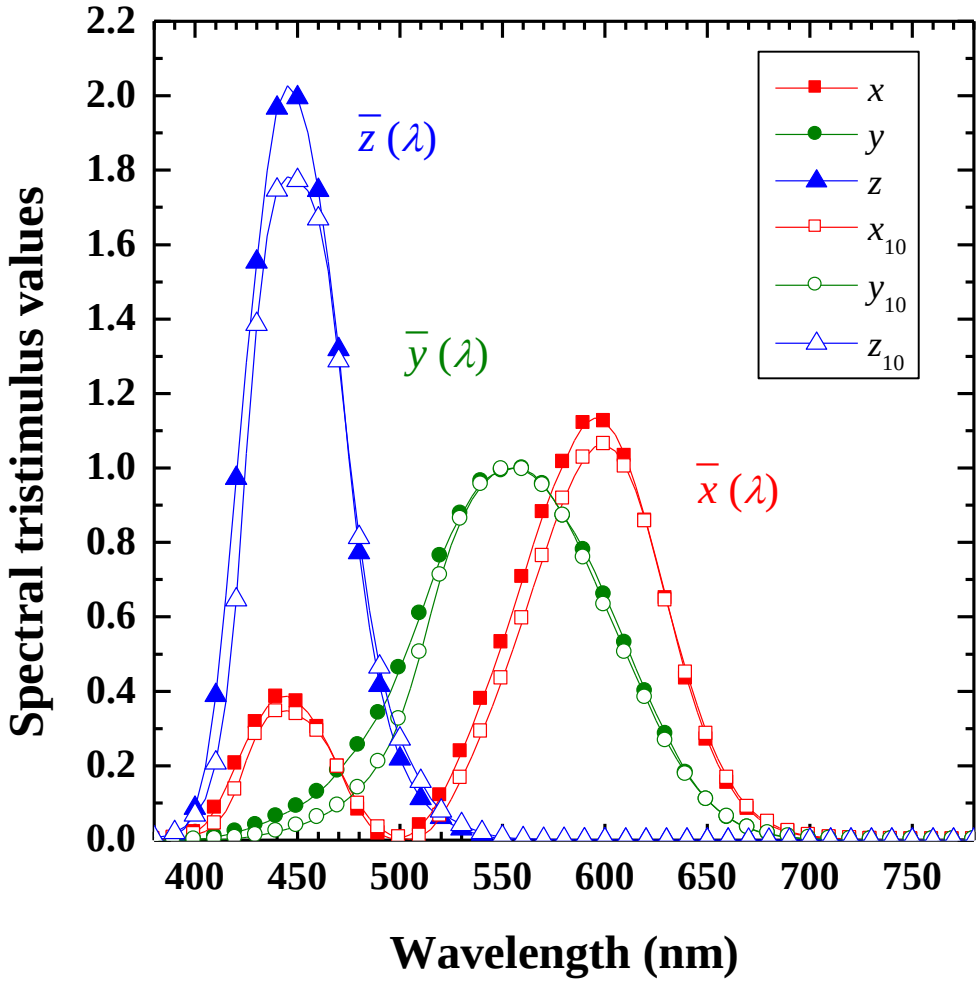

Fig.2.2. Color matching functions.

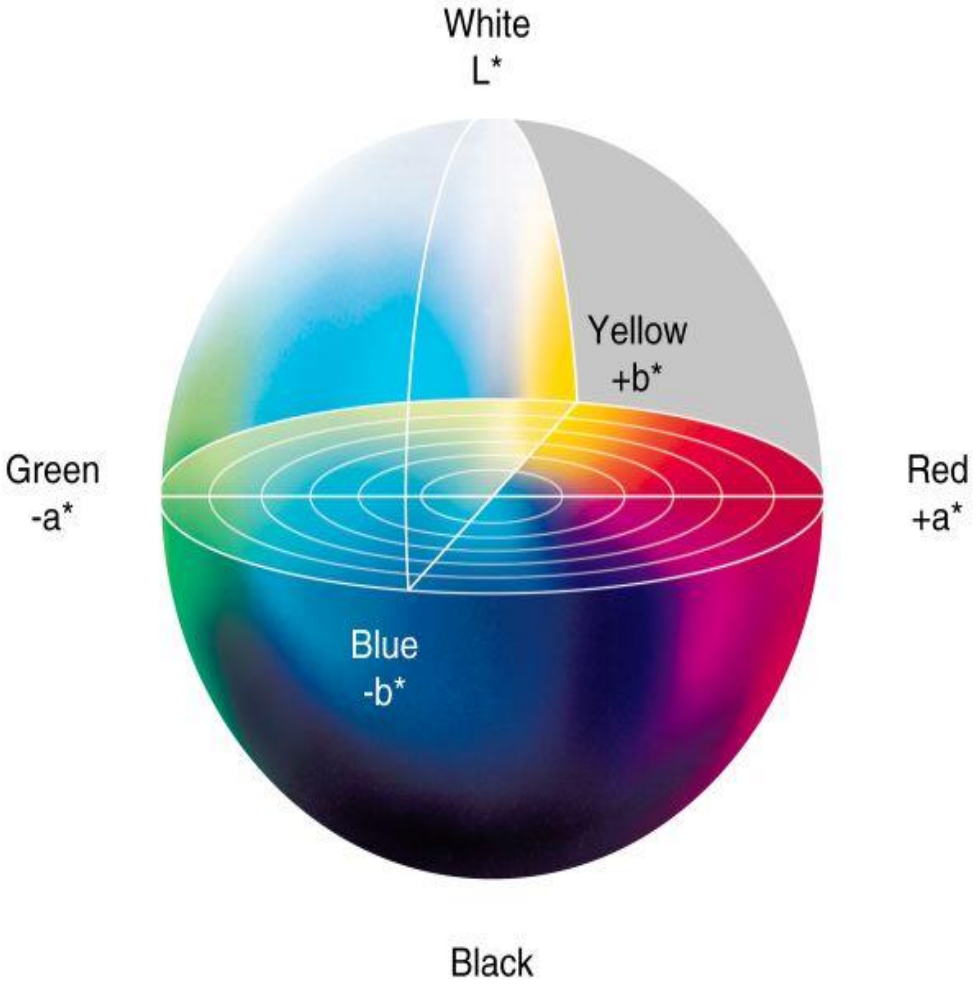

Fig.2.3. A three dimensional representation of the CIE LAB color space.

2.3.4 Photon Fluence

Photon fluence ϕ [11] represents the amount of light absorption in each volume element of skin tissue model, and is calculated by,

$$\phi[i_x, i_y, i_z] = \frac{A[i_x, i_y, i_z]}{\mu_a} \ [\mathrm{cm}^{-2}] \tag{2.13}$$

Where A denotes the probability density of amount of light absorption per unit volume with μ_a being the local absorption coefficient, and i_x, i_y and i_z indicate the element number of each grid in the horizontal (i_x, i_y) and vertical (i_z) direction in the skin tissue model. The fluence is usually resolved along the depth (i_z) and such examples are shown in Fig. 2.4, where photon fluence is mapped along x-z plane, and x direction represents skin surface and z direction depth of tissue model. The fluence near the photon incident has a larger value due to the addition of back scatter light. Also, medium with refractive index mismatched boundary has higher fluence rate because of internal reflection compared to refractive index matched boundary (detailed explanation is given in chapter 3). Two types of flucence calculation are used in this study. One is a fluence map of the total components which consist of all the reflected, absorbed and transmitted components and the other fluence map is of the detected components consisting only reflected components, as shown in Fig. 2.4.

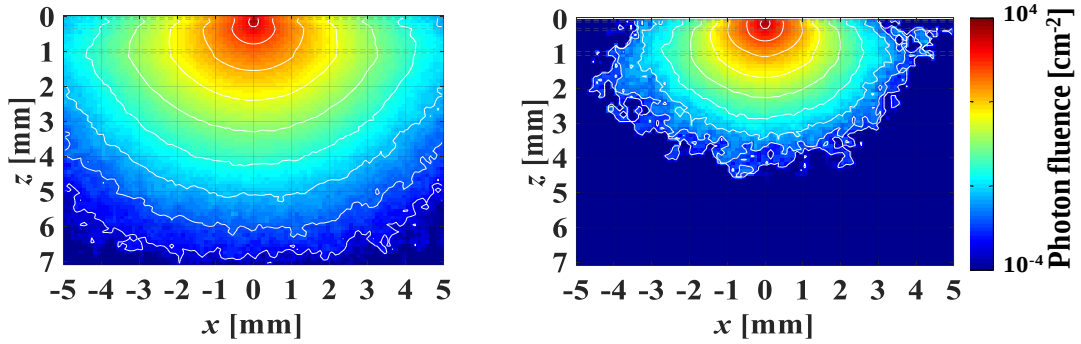

(a) Fluence of the total components. **(b)** Fluence of the detected components.

Fig.2.4. Two typical maps of simulated photon fluence along z direction.

2.3.5 Point Spread Function of Reflected Intensity

When an infintely narrow photon beam incident on the surfacr of the skin tissue model, it strats propagating inside the skin model with random steps in random direction. After the endo of propagation, if the backscattered photons are recorded on the skin surface, it generates an intensity decaying map which has maximum intensitynear the point of incident. From this intensity map, point spread function (PSF) of reflected intensity on the skin surface can be calculated. Typical examples of simulated PSF at 400nm, 550nm and 700nm are shown in Fig. 2.5, in which x= 0 means center of point like illumination. PSF has wavelength dependency because of varying optical path length in tissue. Owing to this property PSF of longer wavelength (700nm) shows broaddening nature and is suitable for evaluating change of skin condition in deeper layers, as can be seen in Fig. 2.5(c) (detailed explanation is given in chapter 4).

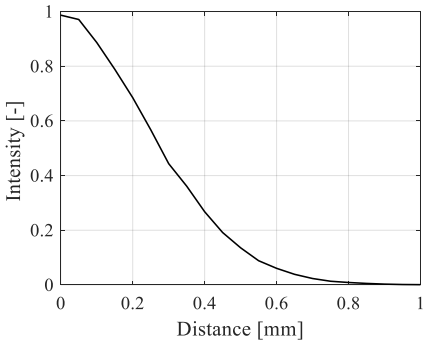

(a) At 400nm

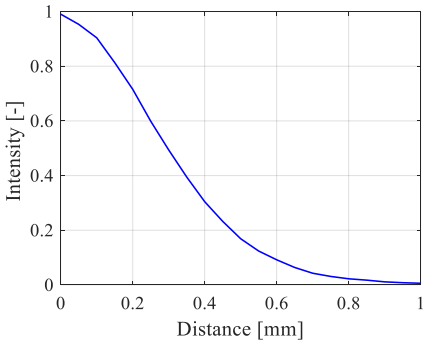

(b) At 550nm

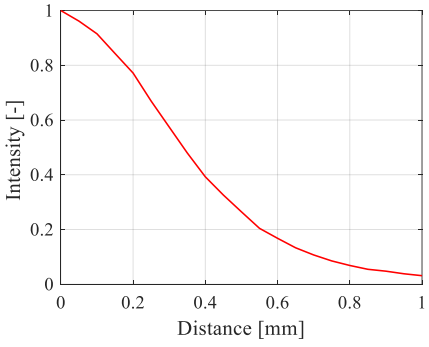

(c) At 700nm

Fig.2.5. Typical examples of simulated PSF at three different wavelengths.

2.4 Multiple Regression Analysis

In the multiple regression analysis [107], a relationship between two variable sets y_k (k =1, 2, …, p) and x_{jk} (j =1, 2, …, q) is assumed to be given by the following linear equation,

$$y_k = \alpha_0 + \sum_{j=1}^{q} \alpha_j \cdot x_{jk} + e_k, \tag{2.14}$$

where y_k and x_{jk} represent response variables and predictor variables, respectively, α_0 means a constant component, and e_k expresses unknown error components. In this multiple regression model, p is the number of sample data being analyzed and q is that of predictor variables. The regression coefficients $\alpha_j (j = 0, 1, 2, \cdots, q)$ are unknown values that are estimated by the method of least squares in the analysis. Let us denote the estimated regression coefficients by $\hat{\alpha}_j$, then the corresponding multiple regression equation is expressed as

$$\hat{y}_k = \hat{\alpha}_0 + \sum_{j=1}^{q} \hat{\alpha}_j \cdot x_{jk}, \tag{2.15}$$

$$y_k = \hat{y}_k + r_k \tag{2.16}$$

where $\hat{y}_k$ means the response variables estimated with using $\hat{\alpha}_j$, and r_k is the residual. A measure for suitability of the regression equation is given by the parameter P^2, which is defined as the square of the multiple correlation coefficient P, that is,

$$P^2 = \left[\frac{\sum_k \left(y_k - \bar{y}_k\right)\left(\hat{y}_k - \bar{\hat{y}}_k\right)}{\sqrt{\sum_k \left(y_k - \bar{y}_k\right)^2} \sqrt{\sum_k \left(\hat{y}_k - \bar{\hat{y}}_k\right)^2}} \right]^2, \tag{2.17}$$

where $\bar{y}_k$ and $\bar{\hat{y}}_k$ denote the average of y_k and $\hat{y}_k$, respectively, over the p number of

data. The value of P means the correlation coefficient between y_k and $\hat{y}_k$. The value of P^2 ranges from 0 to 1, and the linear approximation becomes better as P^2 approaches to 1.

2.5 Monte Carlo Modeling of Light Transport in Scattering Medium

2.5.1 Optical Properties

The simple concept of absorption of light can be explained as following description. Consider a chromophore idealized as a sphere with a particular geometrical size. Consider that this sphere blocks incident light and casts a shadow, which constitutes absorption. The size of the absorption shadow is called the effective cross-section, σ_a (cm^2), and can be smaller or larger than the geometrical size of the chromophore, A (cm^2), related by the proportionality constant called the absorption efficiency, Q_a (dimensionless), as,

$$\sigma_a(\text{cm}^2) = Q_a(\text{-}) \cdot A_a(\text{cm}^2) . \tag{2.18}$$

The absorption coefficient μ_a (cm^{-1}) describes a medium containing many chromophores at a concentration described as a volume density, ρ_a (cm^3). The absorption coefficient is essentially the cross-sectional area per unit volume of medium.

$$\mu_a(\text{cm}^{-1}) = \rho_a(\text{cm}^{-3}) \cdot \sigma_a(\text{cm}^2) . \tag{2.19}$$

Experimentally, the units (cm^{-1}) for μ_a are inverse length, such that the product $\mu_a \cdot L$ is dimensionless, where L (cm) is a photon's path length of travel thorough the medium. The probability of survival or transmission T of the photon after a path length L is:

$$T = \exp(-\mu_a \cdot L). \tag{2.20}$$

This expression for survival holds true regardless of whether the photon path is a straight line or a highly tortuous path due to multiple scattering in an optically turbid medium.

The simple concept of scattering of light can be explained as following description. Consider a scattering particle idealized as a sphere with a particular geometrical size. Consider that this sphere redirects incident photons into new directions and so prevents the forward on-axis transmission of photons, thereby casting a shadow. This process constitutes scattering. The size of the scattering shadow is called the effective cross-section, σ_s (cm^2), and can be smaller or larger than the geometrical size of the scattering particle, A (cm^2), related by the proportionality constant called the scattering efficiency, Q_s (dimensionless), as,

$$\sigma_s(\mathrm{cm}^2) = Q_s(\text{-}) \cdot A_s(\mathrm{cm}^2). \tag{2.21}$$

The scattering coefficient μ_s (cm^{-1}) describes a medium containing many scattering particles at a concentration described as a volume density, ρ_s (cm^3). The scattering coefficient is essentially the cross-sectional area per unit volume of medium.

$$\mu_s(\mathrm{cm}^{-1}) = \rho_s(\mathrm{cm}^{-3}) \cdot \sigma_s(\mathrm{cm}^2). \tag{2.22}$$

Experimentally, the units (cm^{-1}) for μ_s are inverse length, such that the product $\mu_s \cdot L$ is dimensionless, where L (cm) is a photon's path length of travel thorough the medium. The probability of transmission T of the photon without redirection by scattering after a path length L is:

$$T = \exp(-\mu_s \cdot L) \tag{2.23}$$

Biological tissue can be assumed to be a random turbid medium, with variations

in the optical properties small enough to prevent localized absorption. In other words, tissue is considered to have volumetric scattering and absorption properties rather than being composed of discrete scattering and absorption centers distributed in a non-scattering, non-absorbing medium. The advantage to the distributed scattering center approach is that for perfect spheres the phase function is known, however there is little similarity between perfect spheres and tissue. Volumetric absorption or scattering is obtained by multiplying an absorption or scattering cross section with the density of absorbers or scatterers [108]. This is how the absorption coefficient μ_a and scattering coefficient μ_s are defined. The scattering and absorption coefficient are typically measured in inverse centimeters and the reciprocal of these coefficients is the average distance that light will travel before being scattered or absorbed, respectively.

The anisotropy factor g (dimensionless) is a measure of the amount of forward direction retained after a single scattering event. Considering that a photon is scattered by a particle so that its trajectory is deflected by a deflection angle θ, as shown in Figure 2.6. Then the component of the new trajectory which is aligned in the forward direction is shown in a dash line as $\cos(\theta)$. On average, there is an average deflection angle and the mean value of $\cos(\theta)$ is defined as the anisotropy. A scattering event causes a deflection at angle θ from the original forward trajectory. There is also an azimuthal angle of scattering, ψ. But it is the deflection angle θ which affects the amount of forward direction, $\cos\theta$, retained by the photon. Consider an experiment in which a laser beam strikes a target such as a cylindrical cuvette containing a dilute solution of scattering particles. The scattering phase function $p(\theta)$ is measured by a detector that is moved in a circle around the target while always facing the target. Hence the detector collects light

scattered at various deflection angle θ in a horizontal plane expectation value for cos(θ):

$$g = \int_0^{\pi} p(\theta)\cos\theta \; 2\pi \sin\theta \; d\theta = <\cos\theta>, \tag{2.24}$$

where

$$\int_0^{\pi} p(\theta) 2\pi \sin\theta \; d\theta = 1. \tag{2.25}$$

It is common to express the definition of anisotropy in an equivalent way:

$$g = \int_{-1}^{1} p(\cos\theta) \; \cos\theta \; d(\cos\theta), \tag{2.26}$$

where

$$\int_{-1}^{1} p(\cos\theta) \; d(\cos\theta) = 1. \tag{2.27}$$

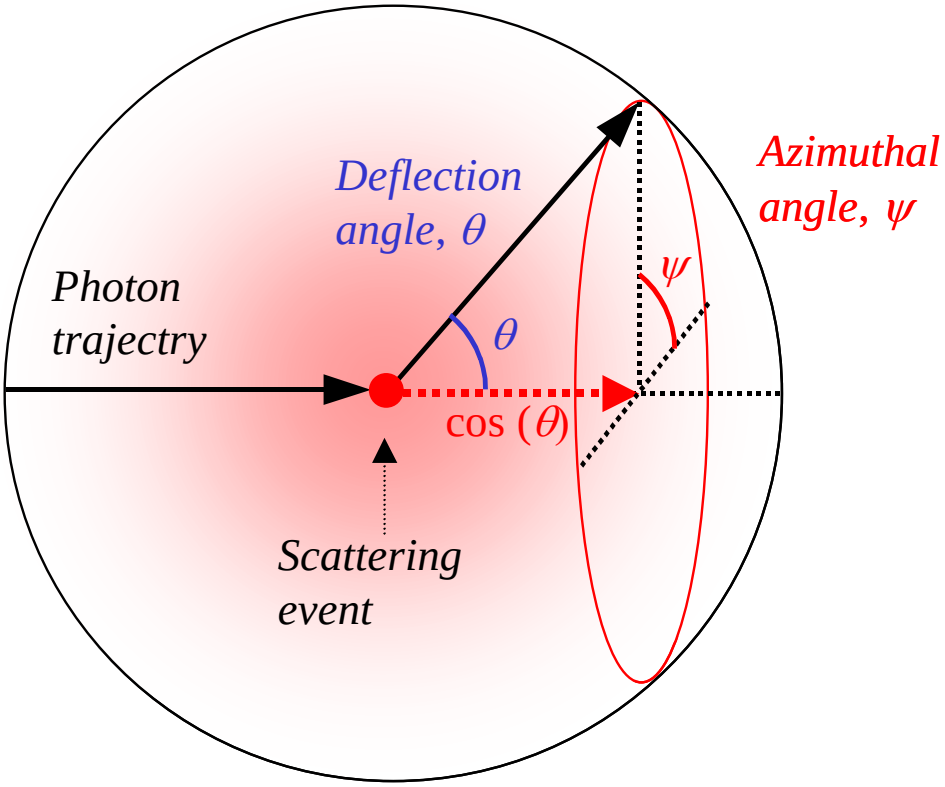

Fig.2.6. Schematic of the definition of anisotropy factor *g*. A scattering event causes a deflection at angle θ from the original forward trajectory. There is also an azimuthal angle of scattering, ψ. However, it is the deflection angle θ which affects the amount of forward direction, cos (θ), retained by the photon.

2.5.2 Scattering Phase Function

The angular dependence of scattering is called the scattering phase function, $p(\theta)$ which has units of [sr $^{-1}$] and describes the probability of photon scattering into a unit solid angle oriented at an angle θ relative to the photons original trajectory. Note that the function depends only on the deflection angle θ and not on the azimuthal angle ψ. Such azimuthally symmetric scattering is special case, but is usually adopted when discussing scattering. However, it is possible to consider scattering which does not exhibit azimuthal symmetry.

The simplest scattering phase function is the isotropic phase function:

$$p(\theta) = \frac{1}{4\pi}. \tag{2.28}$$

The isotropic phase function would scatter light with equal efficiency into all possible directions.

The Henyey-Greenstein scattering phase function [109] has proven to be useful in approximating the angular scattering dependence of single scattering events in biological tissues. The Henyey-Greenstein scattering phase function allows the anisotropy factor g to specify $p(\theta)$ such that calculation of the expectation value for $\cos(\theta)$ returns exactly the same value of g. This scattering phase function is given as,

$$p(\theta) = \frac{1}{4\pi} \cdot \frac{1-g^2}{\left(1+g^2-2g\,\cos\theta\right)^{\frac{3}{2}}}. \tag{2.29}$$

It is common practice to express the Henyey-Greenstein function as the function $p(\cos\theta)$;

$$p(\cos\theta) = \frac{1}{2} \cdot \frac{1-g^2}{\left(1+g^2-2g\,\cos\theta\right)^{\frac{3}{2}}}. \tag{2.30}$$

2.5.3 Monte Carlo Method

Monte Carlo method [10, 11] has been used to simulate the photon migration in the random scattering media such as a biological tissue. In all applications of the Monte Carlo method, a stochastic model is constructed in which the expected value of a certain random variable is equivalent to the value of a physical quantity to be determined. The Monte Carlo method describes local rules of photon propagation that are expressed, in the simplest case, as probability distributions that describes the step size of photon movement between sites of photon-tissue interaction, and the angles of deflection in a photon's trajectory when scattering event occurs. Since, the Monte Carlo method is statistical in nature and, thus, relies on calculating the propagation of a large number of photons by the computer, the method requires a large amount of computational time.

The Monte Carlo simulations are based on the macroscopic optical properties that are assumed extend uniformly over small units of tissue volume. In this dissertation, the photons are treated as classical particles, and polarization and wave phenomenon are neglected. Once photon which has the weight w launched in the tissue, it is moved a step size s where it may be scattered, absorbed, internally reflected, or transmitted out of the medium. The photon is repeatedly moved until it either escapes from or is absorbed completely in medium. This process is repeated until the desired number of photons has been propagated. The physical quantities such as the diffuse reflectance, total transmittance, and internal absorption are scored during the simulation. In this section, the algorithms of Monte Carlo simulation reported by Prahl *et al*. [10], and Wang *et al*. [11], are mainly referred.

A. Coordinate Systems

The simplest Monte Carlo simulation deals with the transport of an infinitely narrow photon beam, perpendicularly incident on a simple- or multi-layered tissue. Each layer is infinitely wide, and is described by the following parameters: the scattering coefficient μ_s(cm^{-1}), absorption coefficient μ_a(cm^{-1}), anisotropy factor g, refractive index n, and thickness t (cm). The refractive indices of the ambient medium above the tissue (e.g. air) and the ambient medium below the tissue (if existing) need to be given as well. The layers are parallel to each other. For the simplicity of notation, the total interaction coefficient μ_t, which is the sum of the scattering coefficient μ_s and the absorption coefficient μ_a, is sometimes used in this dissertation. The interaction coefficient means the probability of photon interaction per unit infinitesimal path length.

Three coordinate systems shown in Fig.2.7 are used in the Monte Carlo simulation [10, 11] at the same time. A Cartesian coordinate system is used to trace photon movements. The origin of the coordinate system is the photon incident point on the tissue surface; the z-axis is the normal of the surface pointing toward the inside of the tissue; and the xy-plane is on the tissue surface.

As the infinitely narrow photon beam is perpendicular to the tissue surface, the problem has cylindrical symmetry. Therefore, a cylindrical coordinate system is set up to score internal photon absorption as a function of radial r and z. The cylindrical coordinate system share and Cartesian coordinate system share the origin and z-axis. The r coordinate of cylindrical coordinate system is also utilized for the diffuse reflectance and diffuse transmittance as a function of r and α, where α is the angle between the photon exiting direction and the normal (-z-axis and z-axis) to the tissue surface.

A moving spherical coordinate system, whose *z*-axis is dynamically aligned with the photon propagation direction, is used for sampling of the propagation direction change of a photon. In this spherical coordinate system, the deflection angle θ and the azimuthal angle ψ due to scattering are first sampled. Then, the photon direction is update in terms of the directional cosines in the Cartesian coordinate system.

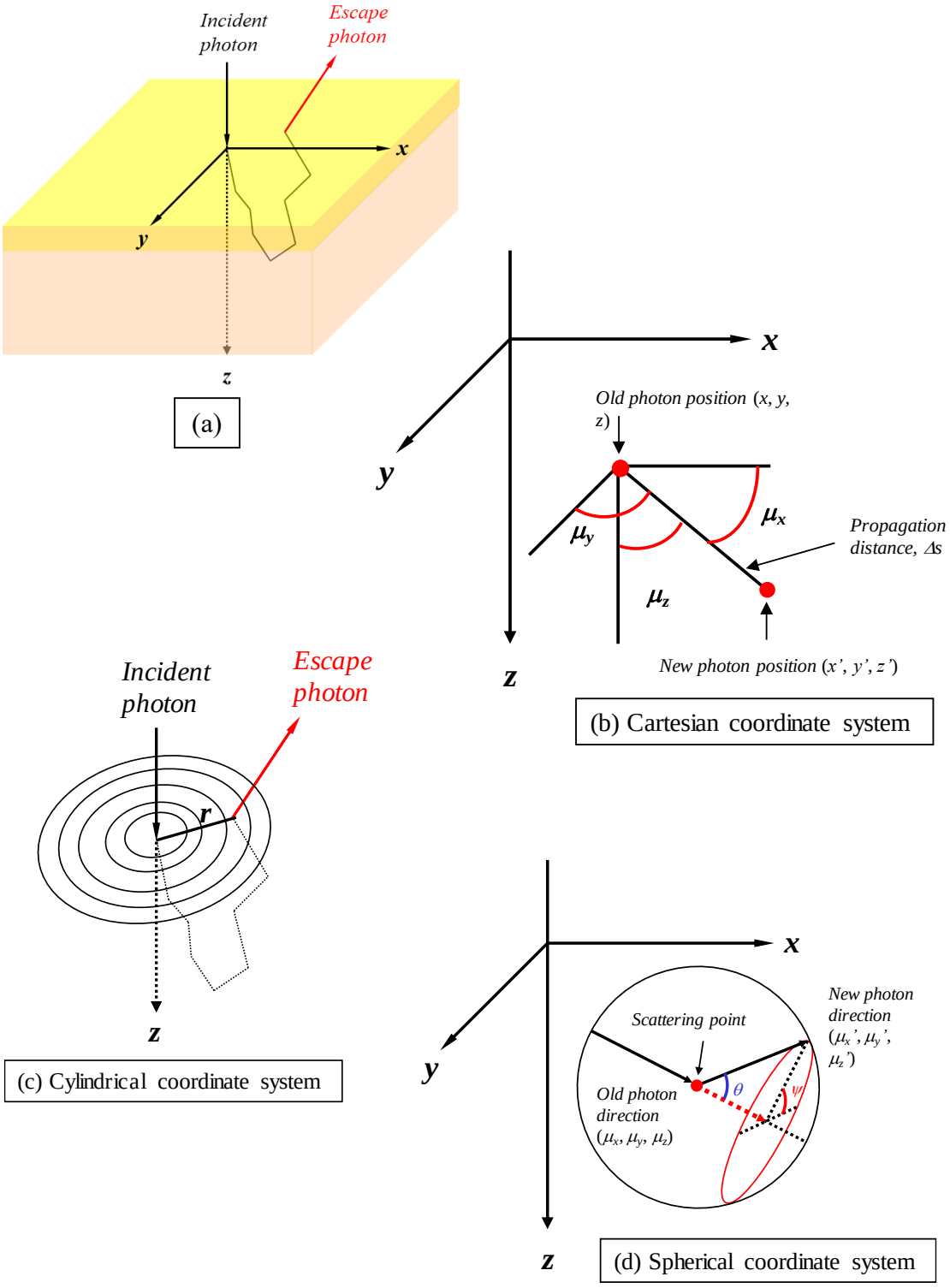

Fig.2.7. The three coordinate systems used in the Monte Carlo simulation.

B. Launch of the Photon

The location of a photon is described by the Cartesian coordinates (x, y, z). The propagating direction of a photon is described by the directional cosines (μ_x, μ_y, μ_z). Each photon is initially assigned a weight w, equal to unity. The photon is injected orthogonally onto the tissue at the origin. The photon position (x, y, z) is initialized to (0, 0, 0), and directional cosines (μ_x, μ_y, μ_z) are se to be (0, 0, 1). The weight w is initialized to be 1.

Once the photon is launched, if there is a refractive-index-mismatched interface between the tissue and ambient medium, some specular reflectance will occur. When the refractive indices of the ambient medium and tissue are n_1 and n_2, respectively, the specular reflectance, R_{sp}, is specified as,

$$R_{sp} = \frac{(n_1 - n_2)^2}{(n_1 + n_2)^2}. \tag{2.31}$$

If the first layer is clear medium, which is on top of layer of medium whose refractive index is n_3, multiple reflections and transmissions on the twp boundaries of the clear layer are considered. The specular reflectance in this case is calculated as,

$$R_{sp} = r_1 + \frac{(1 - r_1)^2 \cdot r_2}{1 - r_1 \cdot r_2} \tag{2.32}$$

where r_1 and r_2 are the Fresnel reflectance on the two boundaries of the clear layer:

$$r_1 = \frac{(n_1 - n_2)^2}{(n_1 + n_2)^2}, \tag{2.33}$$

$$r_2 = \frac{(n_3 - n_2)^2}{(n_3 + n_2)^2}. \tag{2.34}$$

After the specular reflection, the photon weight initialized to 1 is decreased by R_{sp} for the

photon to enter the tissue as

$$w = 1 - R_{sp} . \tag{2.35}$$

C. Moving of the Photon

The step size Δs represents the distance between two successive interactions, or scattering in the tissue. The step size for each photon step Δs follows Beer's law, that is to say, it is more likely for a photon to travel a short distance than a long distance and the probability is proportional to $\exp(-\mu_t \cdot \Delta s)$. A function of a random variable (ξ_1) uniformly distributed between 0 and 1, which yields a random variable with this distribution [10, 11] is

$$\Delta s = \frac{-\ln \xi}{\mu_t} . \tag{2.36}$$

Once a step size Δs is determined, the photon is moved in the tissue. The position of photon is update by:

$$\begin{aligned} x &\leftarrow x + \mu_x \cdot \Delta s \\ y &\leftarrow y + \mu_y \cdot \Delta s , \\ z &\leftarrow z + \mu_z \cdot \Delta s \end{aligned} \tag{2.37}$$

where the arrows indicate quantity substitutions. The variables on the left-hand side have the new updated values, and the variables on the right-hand side have the old values.

D. Absorption of the Photon

Once the photon has reached an interaction site, a fraction of the photon weight (energy of photon) Δw, absorbed by the interaction site is calculated as

$$\Delta w = \left(\frac{\mu_a}{\mu_t} \right) \cdot w, \tag{2.38}$$

which will be deposited in the local grid element. The photon weight Δw is scored into $A(r, z)$ at the local grid element:

$$A(r,\ z) \leftarrow A(r,\ z) + \Delta w. \tag{2.39}$$

The current photon weight is updated as well by:

$$w \leftarrow w - \Delta w. \tag{2.40}$$

The photon with new weight w will suffer scattering at the interaction site.

E. Scattering of the Photon

Once the photon has reached an interaction site and its weight decreased, the photon with new weight is ready to be scattered. There will be a deflection angle, $\theta (0 \le \theta < \pi)$, and an azimuthal angle, $\psi (0 < \psi < 2\pi)$, to be sampled statistically. The probability distribution for the cosine of the deflection angle, $\cos\theta$, is dscribed by the scattering phase function. When the Henyey-Greenstein function [110] is employed, the scattering phase function is described as

$$p(\cos\theta) = \frac{1 - g^2}{2(1 + g^2 - 2g\cos\theta)^{\frac{3}{2}}}, \tag{2.41}$$

where the anisotropy, g, equals $< \cos\theta >$ and has a value between –1 and 1. A value of 0 indicates isotropic scattering and a value near 1 indicates forward-directed scattering. The

$\cos\theta$ is expressed as a function of the random number, ξ_2:

$$\cos\theta = \frac{1}{2g}\left\{1+g^2-\left[\frac{1-g^2}{1-g+2g\xi_2}\right]\right\} \text{ if } g \neq 0, \tag{2.42}$$

$$\cos\theta = 2\xi - 1 \qquad \text{if } g = 0. \tag{2.43}$$

The azimuthal angle, ψ, is uniformly distributed over the interval 0 to 2π, is sampled as

$$\psi = 2\pi\xi_3. \tag{2.44}$$

Once the deflection and azimuthal angles are chosen, the new direction of the photon can be calculated [10, 11] as

$$\begin{aligned}
\mu_x' &= \frac{\sin\theta}{\sqrt{1-\mu_x^2}}(\mu_x \cdot \mu_z \cos\psi - \mu_y \sin\psi) + \mu_x \cos\theta \\
\mu_y' &= \frac{\sin\theta}{\sqrt{1-\mu_x^2}}(\mu_y \cdot \mu_z \cos\psi - \mu_x \sin\psi) + \mu_y \cos\theta. \\
\mu_z' &= -\sin\theta\cos\psi\sqrt{1-\mu_z^2} + \mu_z\cos\theta
\end{aligned} \tag{2.45}$$

If the photon direction is sufficiently close to the z-axis (e.g. $|\mu_z| > 0.99999$), then the following formulas should be used:

$$\begin{aligned}
\mu_x' &= \sin\theta\cos\psi \\
\mu_y' &= \sin\theta\sin\psi. \\
\mu_z' &= \frac{\mu_z}{|\mu_z|}\cos\psi
\end{aligned} \tag{2.46}$$

F. Internal Reflection of Photon

The internal reflection may occur when the photon in the current layer is across a boundary into another layer with a different index of refraction. The possibility that the photon will be internally reflected is determined by the Fresnel's formulas [111, 112]:

$$R(\alpha_i) = \frac{1}{2}\left[\frac{\sin^2(\alpha_i - \alpha_t)}{\sin^2(\alpha_i + \alpha_t)} + \frac{\tan^2(\alpha_i - \alpha_t)}{\tan^2(\alpha_i + \alpha_t)}\right], \tag{2.47}$$

where $\alpha_i = \cos^{-1}(|\mu_z|)$ is the angle of incidence on the boundary and the angle of transmission α_t is given by Snell's law as

$$n_i \sin\alpha_i = n_t \sin\alpha_t\,, \tag{2.48}$$

where n_i and n_t are the indices of refraction of the medium from which the photon is incident and transmitted, respectively. A random number ξ_4 uniformly distributed between 0 and 1 is used to decide whether the photon is reflected or transmitted, that is,

$$\text{If } \xi_4 \le R(\alpha_i)\text{, then the photon is internally reflected.} \tag{2.49}$$

$$\text{If } \xi_4 > R(\alpha_i)\text{, then the photon transmits.} \tag{2.50}$$

If the photon is internally reflected, the photon stays on the boundary and its directional cosines (μ_x, μ_y, μ_z) are updated by reversing the z component:

$$(\mu_x,\ \mu_y,\ \mu_z) \leftarrow (\mu_x,\ \mu_y,\ -\mu_z)\,. \tag{2.51}$$

If the photon transmits across the boundary, it is determined whether the photon has entered another layer of tissue or ambient medium. If the photon is transmitted to another layer of tissue, it continues propagation with an updated direction and step size. The new directional cosines are given as

$$\begin{aligned}
\mu_x' &= \sin\alpha_t \cdot \mu_x / \sin\alpha_i \\
\mu_y' &= \sin\alpha_t \cdot \mu_y / \sin\alpha_i \\
\mu_z' &= \frac{\mu_z}{|\mu_z|}\cos\alpha_t
\end{aligned} \tag{2.52}$$

or employing Snell's law, Eq.(2.52) rewritten as

$$\begin{aligned} \mu_x' &= \mu_x \cdot n_i / n_t \\ \mu_y' &= \mu_y \cdot n_i / n_t \\ \mu_z' &= \frac{\mu_z}{|\mu_z|} \cos\alpha_t \end{aligned} \tag{2.53}$$

G. Scoring Physical Quantities

In this section, two scored physical quantities; diffuse reflectance R and transmittance T are described. The other quantities such as the internal absorption and fluence rate are excluded because this dissertation does not treat these quantities. If the photon escapes the tissue into the ambient medium, the photon weight is scored into diffuse reflectance or transmittance. If the photon has not been scattered, the photon weight is scored into unscattered reflectance or transmittance depending on the where the photon escapes. If the photon has been scattered at least once, the diffuse reflectance, $R(r, \alpha_t)$, or diffuse transmittance, $T(r, \alpha_t)$, at particular grid element (r, α_t) is incremented by the amount of escapes photon weight, W:

$$\begin{aligned} R(r,\ \alpha_t) &\leftarrow R(r,\ \alpha_t) + w \quad \text{if } z = 0 \\ T(r,\ \alpha_t) &\leftarrow T(r,\ \alpha_t) + w \quad \text{if } z = \text{the bottom of the tissue.} \end{aligned} \tag{2.54}$$

Because the photon has completely escaped, the tracing of this photon ends here. A new photon may be launched into the tissue and traced thereafter. After tracing multiple photons, the total diffuse reflectance R and transmittance T are calculated from the array of $R(r, \alpha_t)$ and $T(r, \alpha_t)$. They are represented by $R_{r\alpha}[i_r, i_\alpha]$ and $T_{r\alpha}[i_r, i_\alpha]$, respectively. The coordinates of the center of a grid element are calculated by:

$$r = (i_r + 0.5) \cdot \Delta r \quad \text{(cm)}, \tag{2.55}$$

$$\alpha = (\mathrm{i}_\alpha + 0.5) \cdot \Delta\alpha \quad \text{(rad)}, \tag{2.56}$$

where i_r and i_α are the indices for r and α, respectively. The raw data give the total photon weight in each grid element in the two-dimensional grid system. To obtain the total photon weight in the grid elements in each direction of the two-dimensional grid system, the 2D arrays are summed in the other dimension:

$$R_r[\mathrm{i}_r] = \sum_{\mathrm{i}_\alpha=0}^{\mathrm{N}_\alpha-1} R_{r\alpha}\ [\mathrm{i}_r,\ \mathrm{i}_\alpha], \tag{2.57}$$

$$R_\alpha[\mathrm{i}_\alpha] = \sum_{\mathrm{i}_r=0}^{\mathrm{N}_r-1} R_{r\alpha}\ [\mathrm{i}_r,\ \mathrm{i}_\alpha], \tag{2.58}$$

$$T_r[\mathrm{i}_r] = \sum_{\mathrm{i}_\alpha=0}^{\mathrm{N}_\alpha-1} T_{r\alpha}\ [\mathrm{i}_r,\ \mathrm{i}_\alpha], \tag{2.59}$$

$$T_\alpha[\mathrm{i}_\alpha] = \sum_{\mathrm{i}_r=0}^{\mathrm{N}_r-1} T_{r\alpha}\ [\mathrm{i}_r,\ \mathrm{i}_\alpha]. \tag{2.60}$$

To obtain the raw data of total diffuse reflectance and transmittance, the 1D arrays are summed again:

$$R = \sum_{\mathrm{i}_r=0}^{\mathrm{N}_r-1} R_r\ [\mathrm{i}_r], \tag{2.61}$$

$$T = \sum_{\mathrm{i}_r=0}^{\mathrm{N}_r-1} T_r\ [\mathrm{i}_r]. \tag{2.62}$$

Finally, the total diffuse reflectance and transmittance are obtained by dividing the raw total diffuse reflectance and transmittance by the total number of photons as

$$R \leftarrow R / N \quad [-], \tag{2.63}$$

$$T \leftarrow T / N \quad [-], \tag{2.64}$$

where [-] indicates dimensionless units.

2.5.4 Inverse Monte Carlo Method

As mentioned section 2.5.3, the Monte Carlo method is generally used for simulation of measurable physical quantities such as the reflectance, transmittance, and internal absorption using given parameters. On the other hand, it can also be a means to estimate those parameters of the tissue such as the absorption coefficient μ_a, scattering coefficient μ_s, and anisotropy factor g, from the measured quantities such as the measured reflectance, transmittance, and/or collimated transmittance. This approach is called the inverse Monte Carlo method [88,113]. In the inverse Monte Carlo method, to determine the unknown optical parameters from measurable macroscopic values, the Monte Carlo simulation is inverted. First of all, the Monte Carlo simulation taking the set of initial values for the optical parameters μ_a, μ_s, and/or g calculates the reflectance, transmittance, and/or collimated transmittance. Then, the calculated quantities are compared with the measured ones. If the significance deviations, the optical parameters are varied slightly, and the new forward simulation are performed. This process is repeated until the deviation between measured and calculated values is within the predetermined threshold.

2.6 Optical Properties of Skin Tissue Components

2.6.1 Scattering by Tissue

The light scattered by a tissue has interacted with the ultrastructure of the tissue. The tissue ultrastructure extends from membranes to membrane aggregates to collagen fibers to nuclei to cell. The light are most strongly scattered by those structures whose

size matches the wavelength of light. For the human skin tissue, the major scatters are the keratin fibers of epidermis, collagen fibers of dermis, and red blood cell, or erythrocyte in blood. The epidermis with its keratin fibers appears to behave somewhat like dermis with collagen fibers, and the scattering coefficient of epidermis is tentatively approximated by that of dermis [7, 88]. The scattering coefficient of dermis have been studied theoretically, as the combination of Mie and Rayleigh scattering primarily from the collagen fibers [88]. The scattering of blood is mainly caused by a refractive index mismatch between the hemoglobin solution within the erythrocyte and the surrounding plasma. In the visible to near-infrared wavelength region, the typical values of anisotropy scattering parameter *g* of the skin tissue are in the range of 0.7-0.95, while that of red blood cell in human blood is the range of 0.985-0.995 [111,113,114]. These values vary with wavelength. Fig. 2.8 shows the published values of (a) scattering coefficient of epidermis and dermis, (b) scattering coefficient of blood, (c) anisotropy scattering parameter of epidermis and dermis, and (d) anisotropy factor of blood.

2.6.2 Absorption by Biological Chromophores

Molecules that absorb light are called chromophores. The major biological chromophores in the human skin tissue are melanin and hemoglobin. Melanin is a polymer built by condensation of tyrosine molecules and usually found in melanosome at basal layer of epidermis. Melanin has a broad absorption spectrum exhibiting stronger absorption at shorter wavelengths [115-117] as shown in Fig.2.9. Melanosomes may contain a variable amount of melanin. The average epidermal absorption coefficient depends on both the absorption coefficient of melanosome and the volume concentration of melanosome in epidermis. Figure 2.10 shows the average absorption coefficient of

melanosome as the function of wavelength [117]. For the human skin, typical ranges for the volume concentration of melanosome C_{mel} in epidermis have been reported [118]: C_{mel} = 1-3% for light-skinned Caucasian, 11-16% for Mediterranean, and 18-43% for darkly pigmented African.

Hemoglobin exists in the erythrocyte and its absorption spectrum changes according to the binding. Hemoglobin molecule bound to oxygen is called oxygenated hemoglobin, while one bound to nothing is deoxygenated hemoglobin. Their spectra of molar extinction coefficients are shown in Fig.2.11. These spectral data are listed in Appendix A1. Hematocrit (Hct) is expressed as the volume fraction or volume concentration of the red blood cells in the whole blood. Typical human whole blood consists of 55% plasma and 45% red blood cells, and, thus, its hematocrit is Hct=45%. In such a condition, hemoglobin has the concentration of 150g/liter of blood. The absorption coefficient of whole blood having Hct=45% can be derived from the following expression:

$$\mu_a(\mathrm{cm}^{-1}) = \frac{2.303 \cdot \varepsilon(\mathrm{cm}^{-1} \cdot \mathrm{M}^{-1}) \cdot (150\ \mathrm{g/liter})}{64500\ (\mathrm{g/mol})}. \tag{2.65}$$

where 2.303 is the conversion constant from the common logarithm to natural logarithm, and 64500 is the gram molecular weight of hemoglobin. The unit M is the molar concentration, that is, (mol/liter). The absorption coefficient of dermis depends on both the absorption coefficient of whole blood and its volume concentration C_b of in dermis.

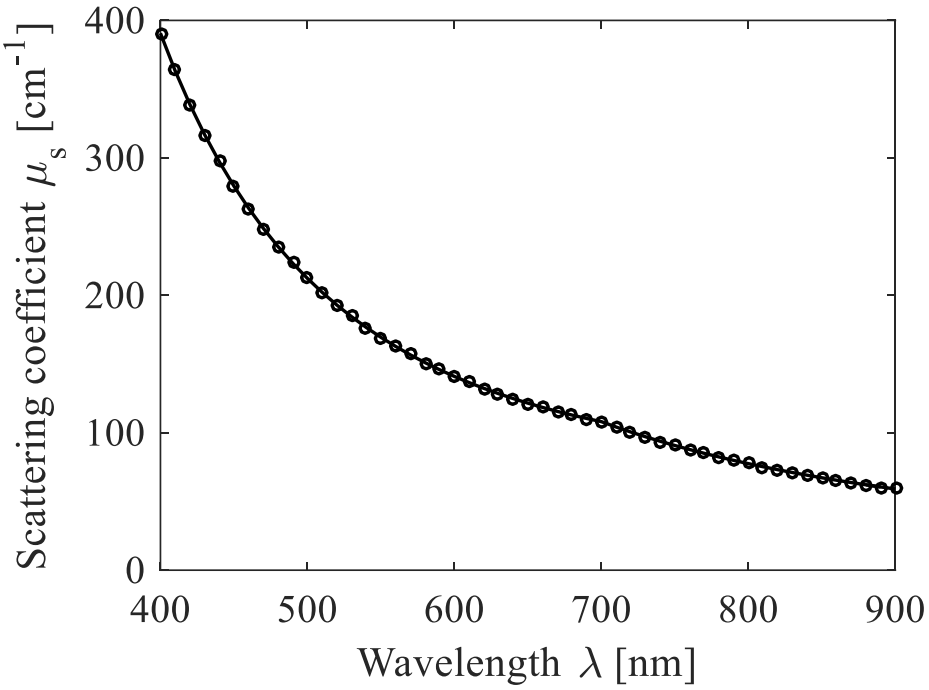

(a) Scattering coefficient of epidermis and dermis.

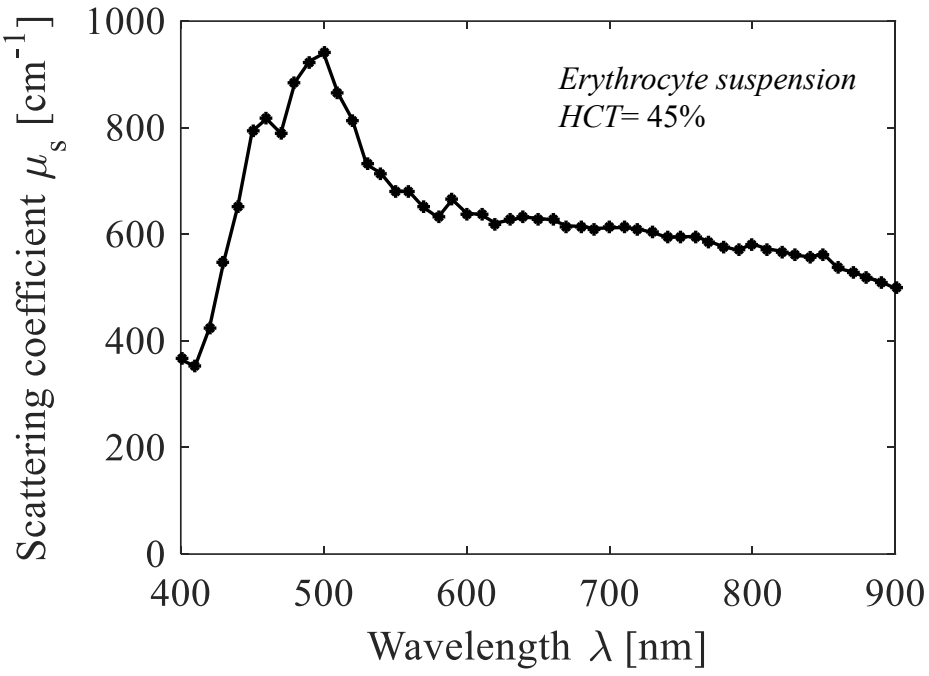

(b) Scattering coefficient of blood.

Fig. 2.8. The published values of (a) scattering coefficient of epidermis and dermis, (b) scattering coefficient of blood, (c) anisotropy scattering parameter of epidermis and dermis, and (d) anisotropy factor of blood.

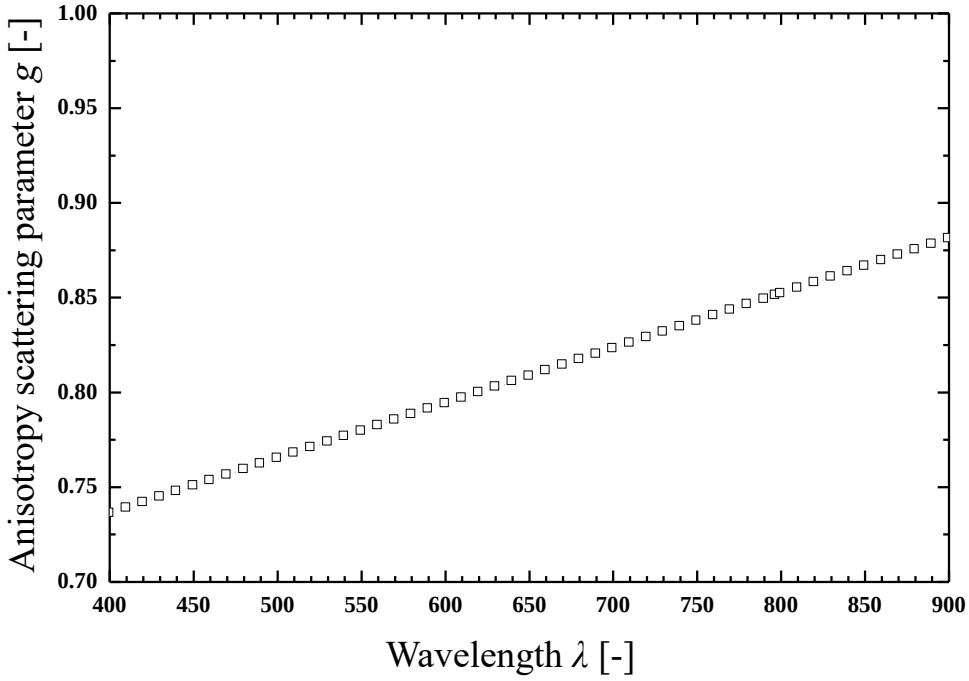

(c) Anisotropy scattering parameter of epidermis and dermis.

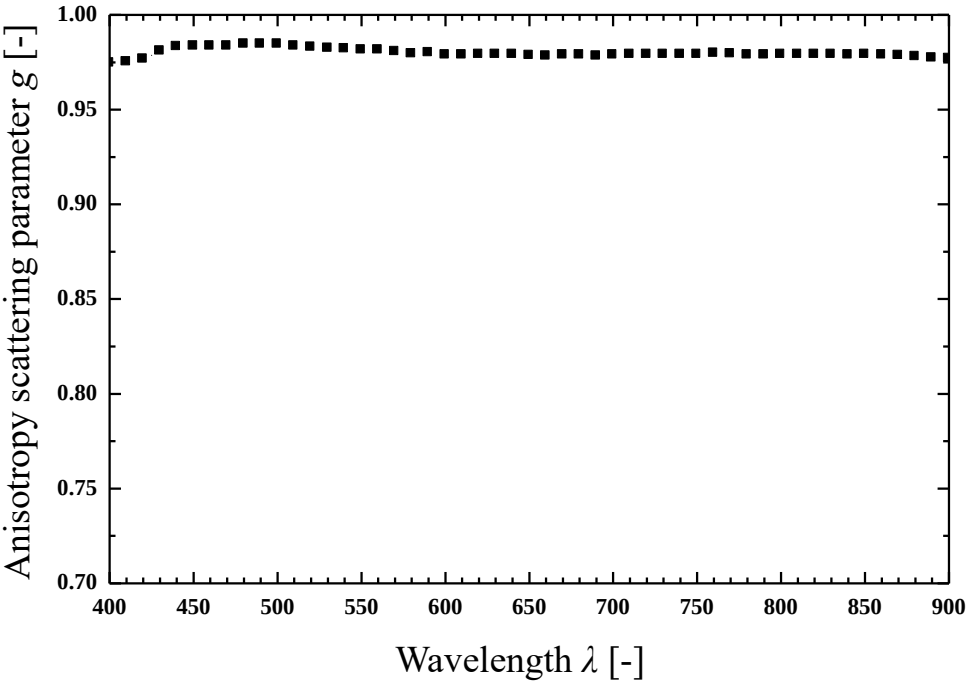

(d) Anisotropy scattering parameter of blood.

Fig. 2.8. The published values of (a) scattering coefficient of epidermis and dermis, (b) scattering coefficient of blood, (c) anisotropy scattering parameter of epidermis and dermis, and (d) anisotropy factor of blood.

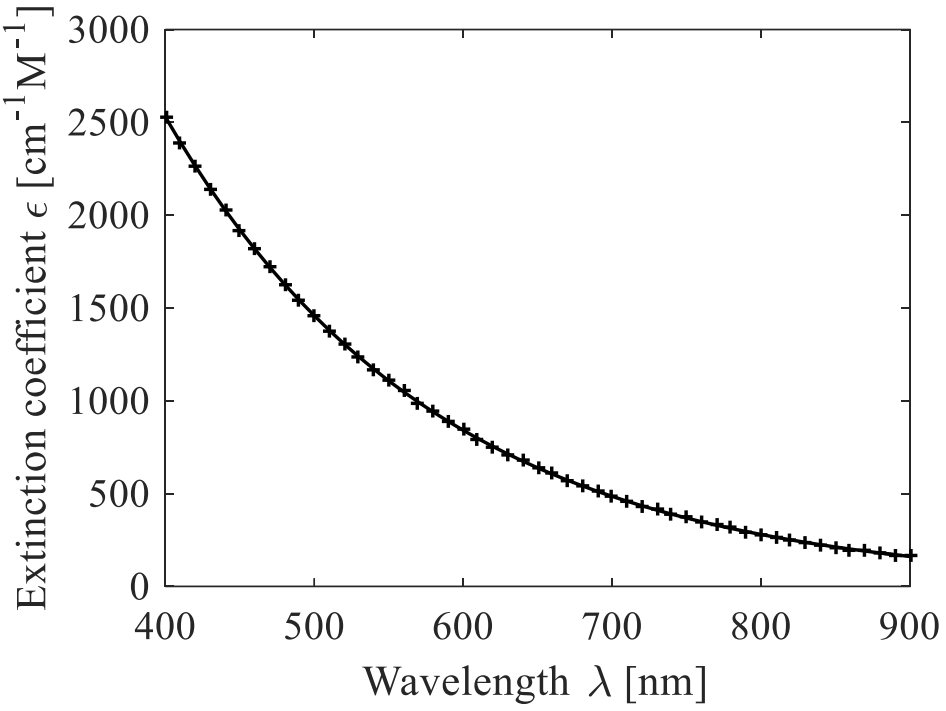

Fig. 2.9. The published values of molar extinction coefficient of melanin.

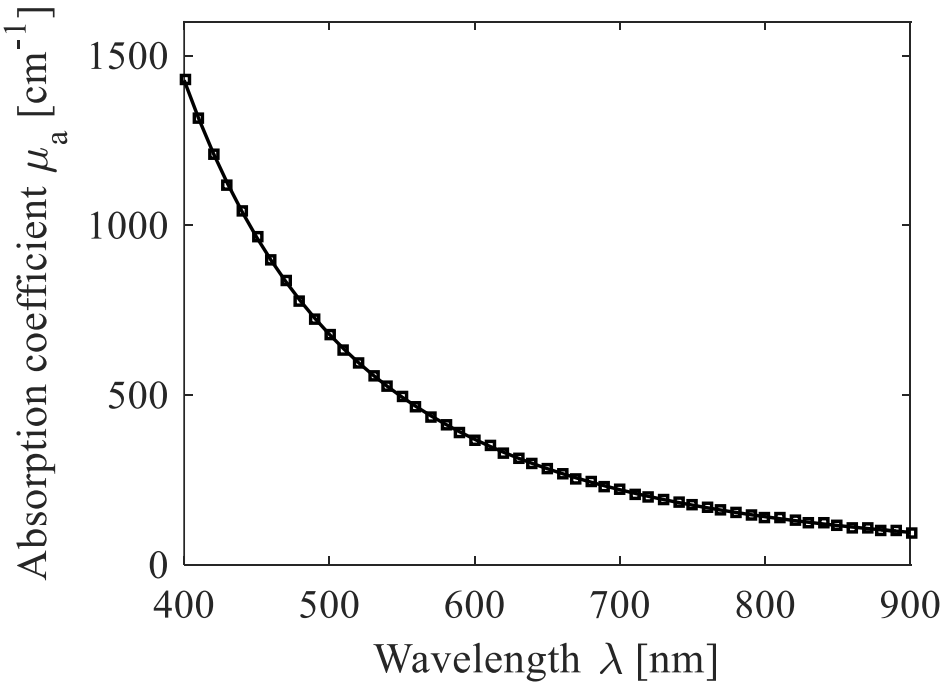

Fig. 2.10. The published values of absorption coefficient of single melanosome.

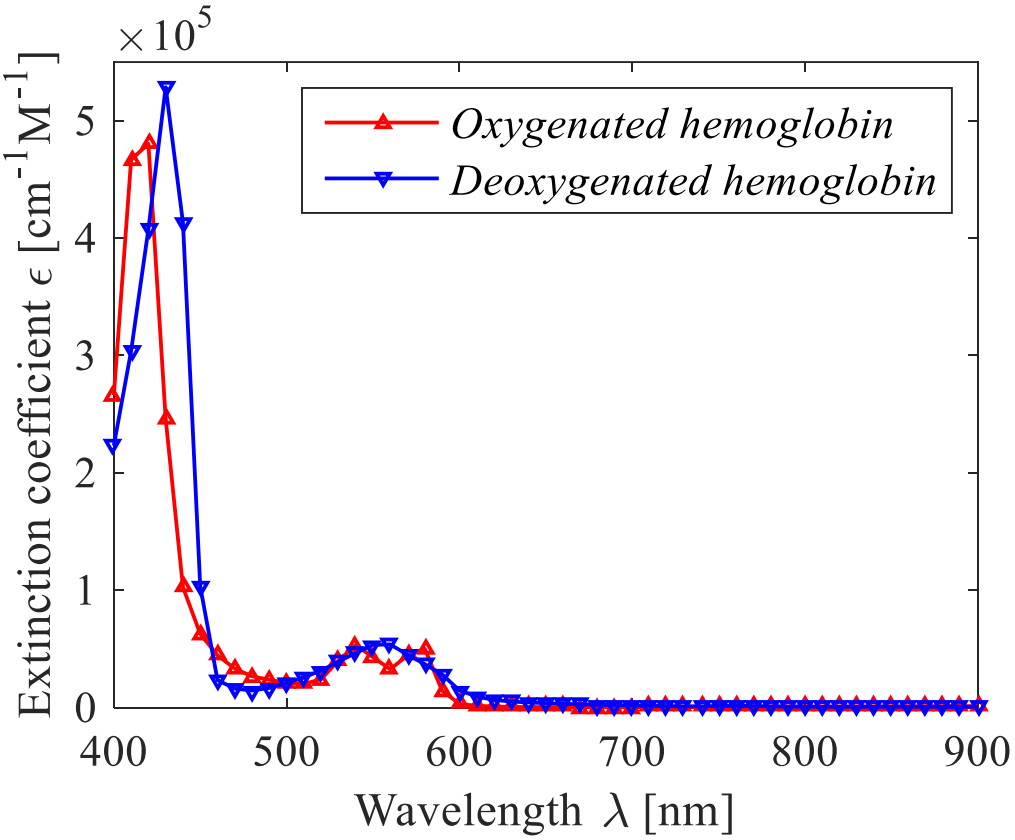

Fig. 2.11. The published values of molar extinction coefficient of oxygenated hemoglobin and deoxygenated hemoglobin.

2.6.3 Refractive Index of Tissue

The refractive index n for the tissue has been studied theoretically and experimentally. Takatani and Graham [119] have studied the values of refractive index for the primary compounds which make up tissue theoretically and reported these values range from 1.47 to 1.49. On the other hand, Jacques *et. al*, [92] calculated $n = 1.37$ at $\lambda = 632.8$ nm for tissue using a predictive method based on the water content of tissue. Parrish *et. al*, [120] have reported a value of $n = 1.55$ for the stratum corneum. Bolin *et. al*, [121] have investigated the refractive index for some mammalian tissues (bovine, porcine, canine, and human) experimentally, and their results showed that the values of n for most tissues range form 1.38-1.42 in the visible to near-infrared wavelength region.

2.7 Layered Skin Tissue Model

It is known that human skin has complex structure as shown schematically in Fig. 2.12(a). Studies of light propagation in skin tissue usually employ a two- or three-layered model which consists of epidermis, dermis, and subcutaneous fat tissue for simplicity. However, the three-layered model is insufficient for reliable investigation of various changes in skin conditions. For example, melanin in epidermis and hemoglobin in dermis have inhomogeneous distribution in a vertical direction. Regarding this aspect, Maeda *et. al.* [122] developed a nine-layered skin tissue model on the basis of histological classification. Figure 2.12 shows the nine-layered model of human skin tissue. There is stratum corneum (layer L_1) of about 10 μm in thickness in the top of skin tissue, and epidermis exists under stratum corneum. Epidermal layer is composed of stratum granulosum and stratum spinosum (layer L_2), and stratum basale (layer L_3). We consider

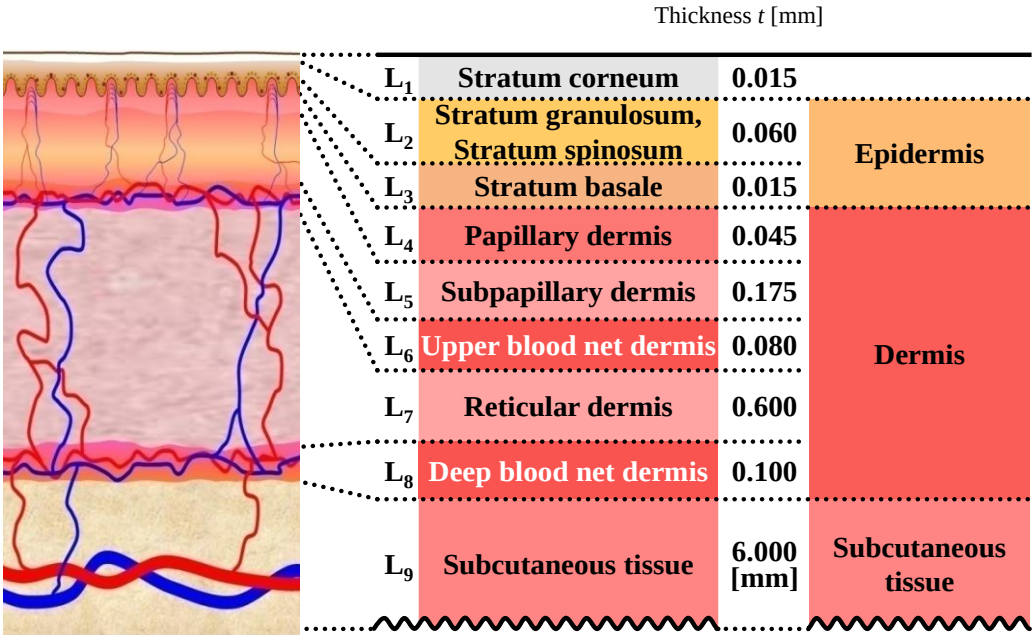

Fig. 2.12 (a) Illustration of skin tissue having complex structure, (b) nine-layered and (c) three-layered models.

that stratum granulosum and stratum spinosum have close histological nature, and treat them as a single layer. The thickness of epidermis is about 100 μm or less usually. Dermis extends under epidermis and is classified into five layers consisting of papillary dermis (layer L_4), subpapillary dermis (layer L_5), upper blood net dermis (layer L_6), reticular dermis (layer L_7), and deep blood net dermis (layer L_8). Dermis is totally about 1.5 mm thick. Subcutaneous fat tissue (layer L_9) is several millimeters in thickness and extends under dermis. Layers L_1 to L_9 are in parallel and we assume that scattering and absorption properties are uniform within each of the nine layers.

If inhomogeneous distribution should be considered, layers may be increased occasionally, to be specific by dividing any such layers into sublayers having different absorption and scattering coefficients from one another. Inclusion of a specific blood region such as an internal blood layer or a blood vessel may be possible as necessary. Blood vessels in the skin tissue are mainly arteriole and venule in layers L_6 and L_8, and capillary loop in layer L_4. These blood vessels may contribute to absorption through the presence of hemoglobin, as well as to scattering due to their network structure. So the effect of these contributions may not be negligible, but it is difficult to treat the distribution of vessels in this model. So, we assume that the overall effects of these contributions are captured as a part of values of absorption and scattering coefficients through the proposed model, which reduces the complexity in calculation of light propagation. Moreover, a lot of fiber components such as collagen and elastin exist in dermis and keep elasticity of the skin. It is known that both of these are also related to scattering properties in tissue, and are characterized by a scattering coefficient in this scheme. On the other hand, pigments such as melanin in epidermis and hemoglobin in dermis are closely related to absorption properties which depend on their concentration,

and are characterized by an absorption coefficient. In this way, the nine-layered structure is considered to give more realistic skin tissue model than the conventional three-layered type used so far. Taking account of various conditions in scattering, absorption, and geometry for each of the nine layers, one can settle various skin conditions. Thickness of layers in Fig. 12 shows typical values obtained by modifying data of Meglinski and Matcher [123], which in this study referred to cheek or forearm area.

2.8 Spectral Reflectance Database

Spectral reflected database is constructed with various simulated reflectance curves using a certain skin model. Through the process of spectral mining from this database one or more simulated spectra can be extracted for a measured spectrum using a basic criterion of root mean square error. From the known optical parameter information of the extracted spectrum, the unknown parameter information of measured spectrum is estimated. To construct the database with simulated spectra in a reasonable size, only absorption coefficient μ_a and scattering coefficient μ_s are changed, keeping other parameters refractive index n, anisotropy scattering parameter g and layer thickness t fixed at the standard condition. Figure 2.13 represents some typical simulated spectra that exists in the database. Furthermore, details of spectral database are discussed in chapters 4 and 5.

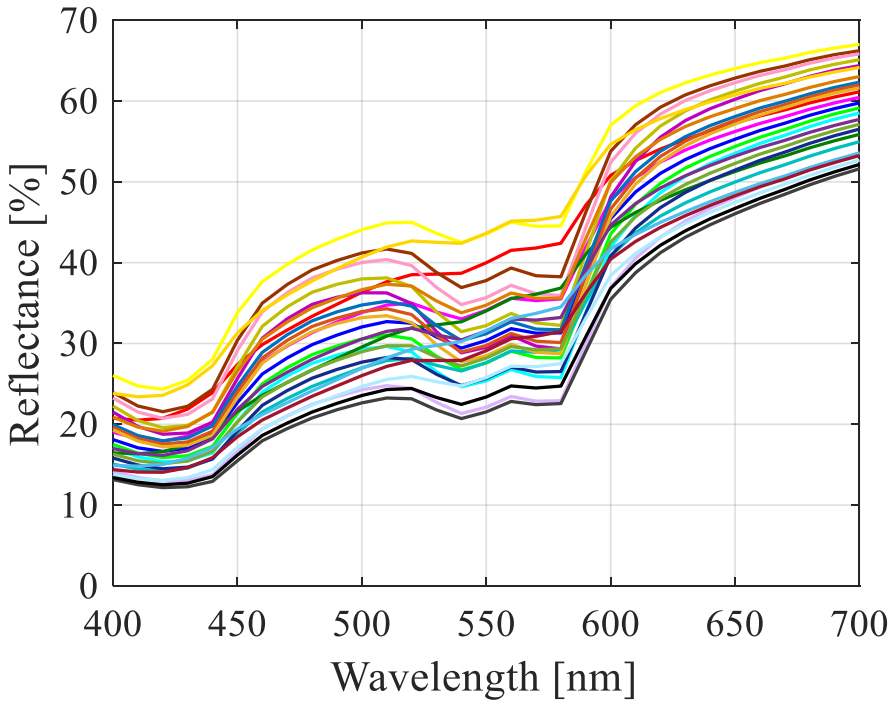

Fig. 2.13 Selected example of simulated spectra in the constructed database.

2.9 Agarose-gel Phantom

To confirm the feasibility of the proposed method, experiments on agarose-gel phantoms has been carried out. To produce skin-alike phantoms a three-layered phantom model is considered, in which layer L_p1, layer L_p2 and L_p3 represents epidermal layer, dermal layer and subcutaneous-fat tissue, respectively. The thickness of layers are: 0.6mm for L_p1, 6.8mm for L_p2 and 4.65mm for L_p3. This set of selected thickness for layers comes from the investigation of various other phantom model with different thickness, where the main prority was given to the nature of the phantom model in recreating the specteal characteristics of human skin tissue. The current selected model with thickness set mentioned above was by far the closest in generating spectral characteristics similar to that of human skin.

In order to accumulate absorption effect or as an melanosome substitute, coffe solution is used in layer L_p1. In case of layers L_p2 and L_p3, horse blood (Nihon Biotest Kenkyujo, Saitama, Japan) with 44% of hematocrit is used as absorber. To achive the scattering effect in all the three layers of phantom different volume concentration (vol. conc.) of 20% intralipos solution (Otsuka Pharmacutical Co. Ltd, Tokyo, Japan) are incorporated. Agar solution is used as the base material in each of the three layers. The agar solution is prepared through the infusion of agar powdre (Ina Shokuhin Kogyo, Nagano, Japan) in saline with a weight ration of 0.8%. No deoxygenetaing agent (for example $Na_2S_2O_4$) is added in layers L_p2 and L_p3, as most of the time it produces chemical imbalance and influences change in optical properties of these layers. So, it is assumed that the oxygeneation level of layers L_p2 and L_p3 is of 100%. Figure 2.14 shows an example of stacked three-layered agarose-gel phantom.

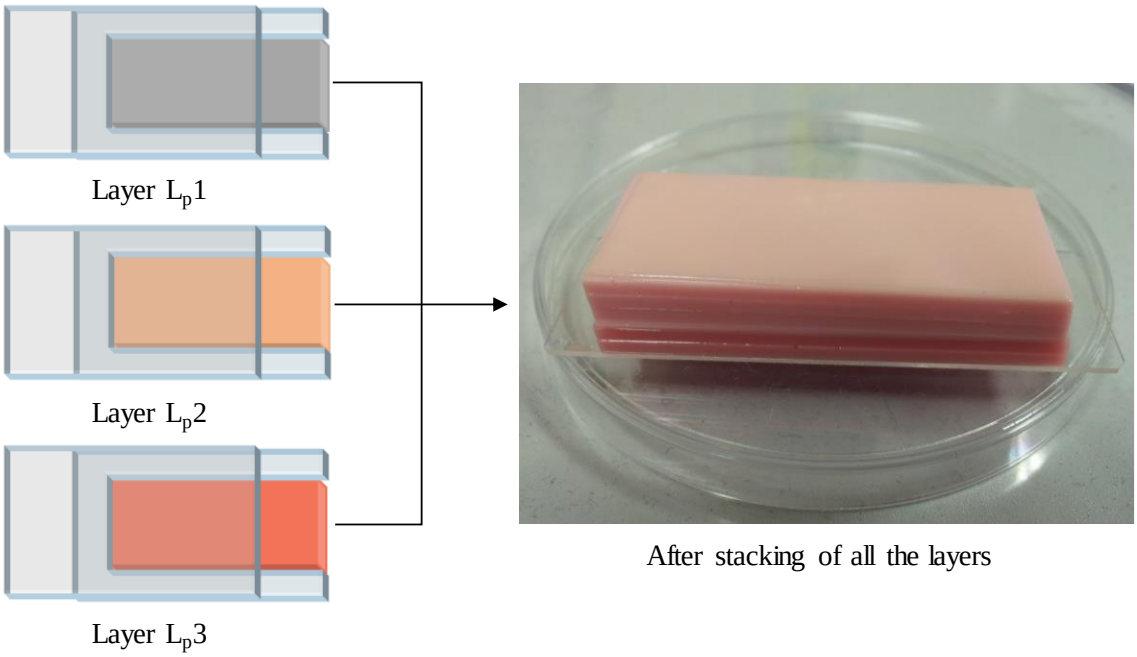

Fig. 2.14 Example of an agarose-gel phantom used in this study.

Chapter 3

Effects of Detection Area on Measurements of Spectral Reflectance in Human Skin Tissue

3.1 Introduction

Light propagation in biological media is interesting physical phenomenon. Human body is especially an important medium in which light is absorbed and scattered in the wavelength-dependent manner. In a visible (VIS) to near-infrared (NIR) range of wavelength, light is known to penetrate in the human tissue in depth of 1~3 mm [124]. This region corresponds successfully to human skin tissue. From this nature, light propagation in human skin tissue have received much attention from researchers who study and develop techniques for measuring concentrations of chromophores such as melanin and hemoglobin [74,125], tissue structural abnormality [126,76,127,128], and skin color [128]. These give useful information for dermatology and cosmetic industry.

In general, propagation of light in VIS-NIR wavelength is investigated by spectrophotometry which gives spectral reflectance. By this typical instrumental approach, many researchers studied the method for estimating melanin and hemoglobin concentration and blood oxygenation dynamics [74,125,128] from analysis of spectral curves. Various types of spectrophotometric systems are commercially available and can easily be used for spectral reflectance measurements.

It should be noticed, however, that measured spectral reflectance contains contribution of light component coming back from a diffusing object and condition of measurements depends on property of light diffusion inside the object. Most direct

measuring condition relating to the light diffusion is a size of a detecting aperture and secondary an area of illumination. When the skin spectral reflectance is measured, the size of a detecting aperture should appropriately be set by considering diffusion properties of light in skin tissue. However, general-purpose spectrophotometer contains only two or three preset sizes of the detecting aperture. Therefore, the necessary size should be investigated for appropriate use of the spectrophotometer which is specific to human skin tissue.

In this study, we investigate the effect of a detecting aperture size on measurements of spectral reflectance in human skin tissue by numerical simulation followed by experiment. For this, we employed Monte Carlo simulation of light propagation in a layered skin tissue model [11], and discussed results of simulated spectral reflectance and photon fluence map. A result of experiment with an integrating sphere demonstrates the same tendency with that of the simulation, though values of reflectance changes are different between simulation and experiment.

3.2 Model of Light Propagation in Skin Tissue

3.2.1 Skin Tissue Model

As introduced in chapter 2, skin tissue has complex structure which is inhomogeneous and shaped irregularly, and has anisotropic physical properties. From a histological point of view, skin tissue is often considered by multi-layered structure which is useful for numerical modelling. Though the conventional studies generally employ a

three-layered model consisting of epidermis, dermis, and subcutaneous fat tissue as shown in Fig. 2.12(c), Maeda *et. al.* developed a nine-layered skin tissue model [122] as shown in Fig. 2.12(b) on the basis of detailed histological knowledge. In Fig. 2.12, typical thickness of each layer is given by literatures [7,122,123,127,129]. Chromophores such as melanin in epidermis and oxygenated or deoxygenated hemoglobin in dermis and subcutaneous tissue are main factors of light absorption properties which depend on their concentration. Cells and fiber components such as blood cells, collagen, and elastin are closely related to light scattering properties due to difference in refractive index. In this model, we assume that absorption and scattering properties are uniform in each of the nine layers. The nine-layered skin tissue model is successfully used for Monte Carlo simulation of light propagation. By setting of values for necessary optical and geometrical parameters in each layer, realistic spectral reflectance curves and visual photon fluence distributions are obtained.

3.2.2 Monte Carlo Simulation

Figure 3.1 shows a concept of Monte Carlo simulation (MCS) for light propagation in multi-layered tissue [11]. The MCS treats light as a bundle of photons. A photon of unit weight enters at the origin of *x, y,* and *z* axes on the tissue surface and begins propagation. Random numbers generated by a computer give a propagating length *S* and direction (θ and ψ) step by step, which are characterized by five input parameters specified to each layer at each wavelength: scattering coefficient μ_s, absorption coefficient μ_a, anisotropy scattering parameter *g*, refractive index *n*, and thickness *t*. Typical values of the parameters can be given by those in literatures [7,122,123,127,129].

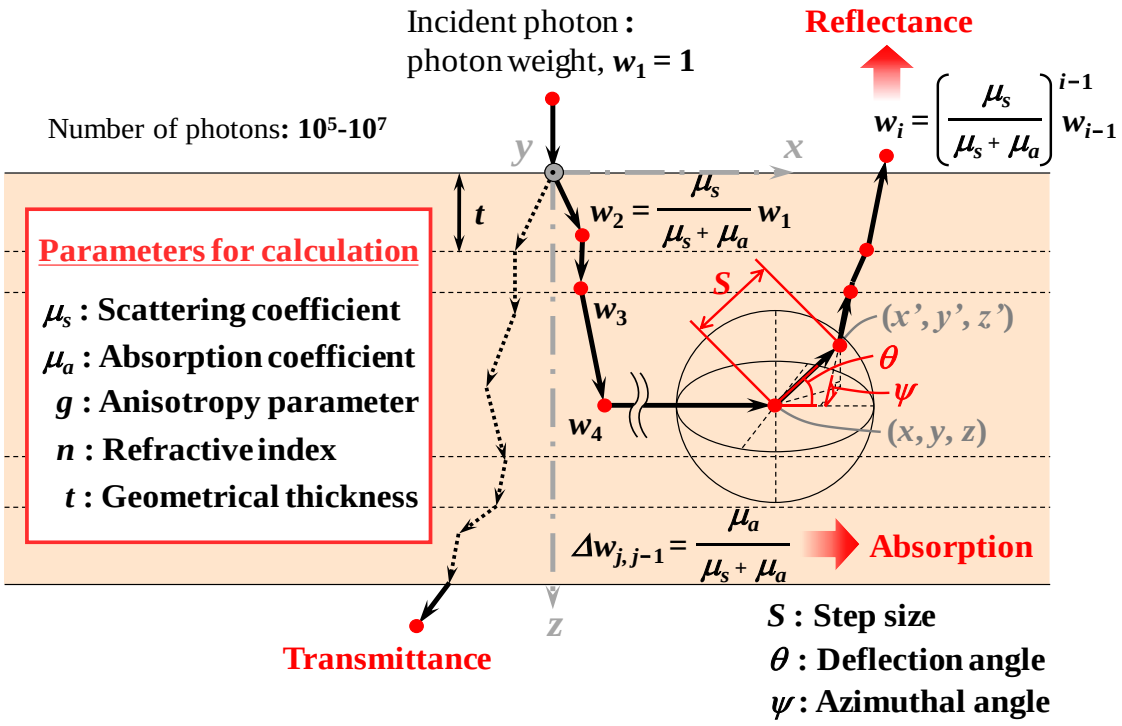

Fig. 3.1 Concept of Monte Carlo simulation of light propagation in multi-layered tissue.

A traveling length in which the photon undergoes neither an absorbing event nor a scattering event is considered as a free path length. After traveling the path length of one step, the photon weight is attenuated at a rate determined by absorption and scattering coefficients. This step-like propagation is repeated by continuous generation of random numbers. When traveling on many steps and the resultant weight is smaller than a preset threshold (10^{-6} in this study), then this photon is regarded as negligibly attenuated, and the second photon enters the tissue. By accumulating values of the weight that are re-emitted from the top surface, reflectance is calculated with reference to the total values

of incident photon weight. We used 10^6 photons to obtain a stable reflectance result at each wavelength. This process is carried out at each of the necessary wavelength points, and finally spectral reflectance is obtained. We took the process in the wavelength range 380-780 nm at an interval of 10 nm.

During the MCS process mentioned above, the computer records and stores all the values of the photon weight with its position in the three-dimensional manner. Thus, the MCS algorithm [11] used in this study provides the amount of light absorption in each volume element of the skin tissue model. This amount is referred to as photon fluence ϕ [11] given by

$$\phi[i_x, i_y, i_z] = \frac{A[i_x, i_y, i_z]}{\mu_a} \quad [\text{cm}^{-2}] \qquad (3.1)$$

where A denotes the amount of light absorption per unit volume, and i_x, i_y, and i_z indicate the element number of each grid in the horizontal (i_x, i_y) and vertical (i_z) directions in the numerical skin tissue model. Here, we investigate the fluence in x-z plane with $y = 0$ in this paper.

We have two different modes in the calculation of photon fluence. One is the total fluence which include all the reflected, absorbed, and transmitted components of light, and another is the detected fluence which contains only reflected component returning to the skin surface. The latter fluence presents light component which is measurable instrumentally on the skin surface. Both these two can visually be expressed by illustration as energy distribution pattern of light propagation.

3.3 Numerical Investigation

3.3.1 Method and Condition

A surface of a skin tissue model is designated by x and y axes, and a direction of penetration into the deep layers is given by z axis. As shown in Fig. 3.2, photons of incident light are launched one by one into the tissue perpendicularly. We investigated three different areas of illumination by a point, circular-spot with 2 and 4 mm in diameter d_i. As for the detection area, we investigated various diameters d of 0.2-40 mm, and all the direction of photons re-emitted from the surface into space are accounted as it is with an integrating sphere. No polarization is considered, but Fresnel reflection law is included in the algorithm. In this study, we assume human forearm skin as an object to be measured and employed its typical values of the MCS parameters from the literature [7,122,123,127,129].

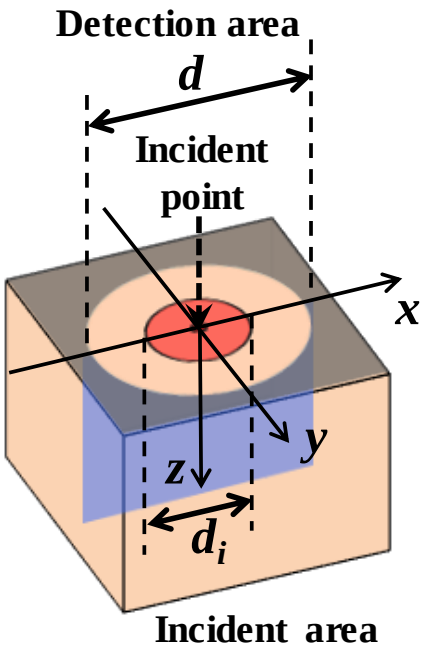

Fig. 3.2 Definition of a point and area for illumination and detection on the skin surface.

3.3.2 Point-like Illumination

Figure 3.3 shows simulated spectral reflectance curves with various diameters of the detection area in the case of point illumination. Results with the large detection area having d = 6 - 40 mm in diameter demonstrate no significant difference in the curves which are overlapped. With reducing the diameter d, reflectance is decreased especially in the longer wavelength range. Figure 3.4 demonstrates the photon fluence maps in x-z plane for the case of 550nm wavelength. The map in (a) of Fig. 3.4 gives the total fluence distribution, while that in (b), (c), and (d) gives the detected fluence distributions. The latter maps are found to depend on diameter d of the detection area. Figure 3.5 demonstrates the photon fluence maps for a case of 700 nm wavelength in the same way as Fig. 3.4. It is clear that light penetrates into the deeper and is diffused more widely. This property indicates that light component penetrated into the deeper layers and diffused and coming back to the surface is not sufficiently detected in cases of using small diameters of the detecting aperture. This tendency is significant in the longer wavelength range in which light penetrates into the deeper and broadens widely in the skin tissue. It is found that the smaller area of detection is unacceptable for appropriate spectral reflectance measurements. The results of Figs.4 to 6 are specific to an ideal situation of the point-like illumination. More realistic situation is to use a circular-spot illumination.

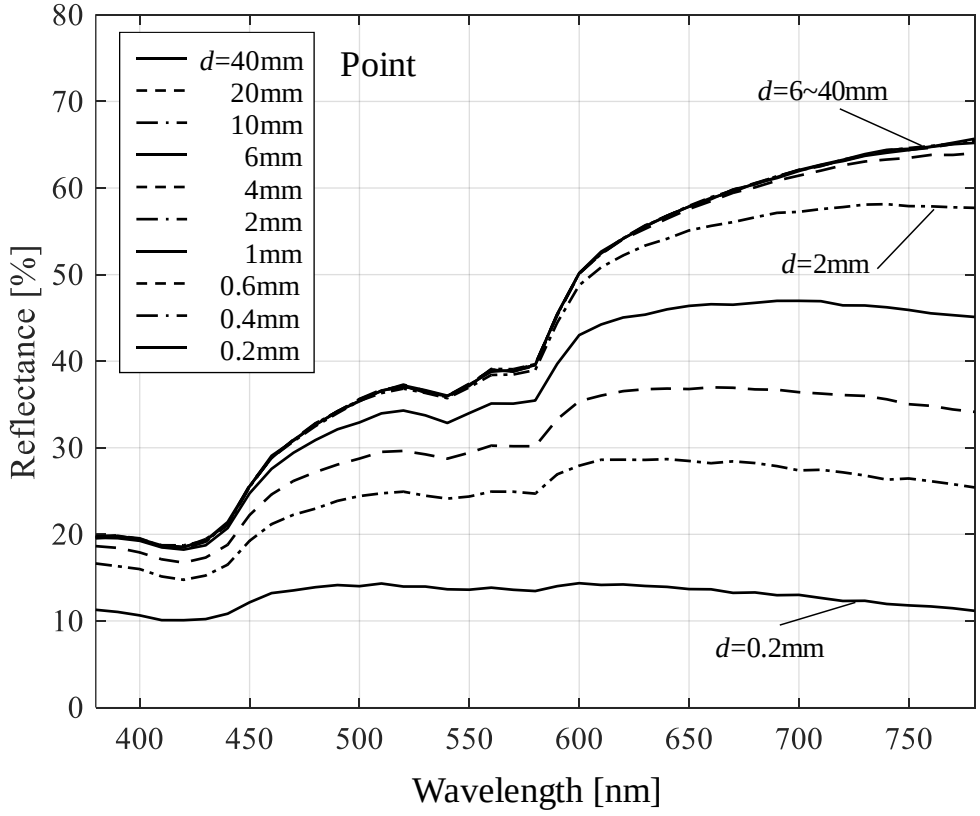

Fig. 3.3 Simulated spectral reflectance curves with different diameters *d* of a detecting aperture for a point-like illumination.

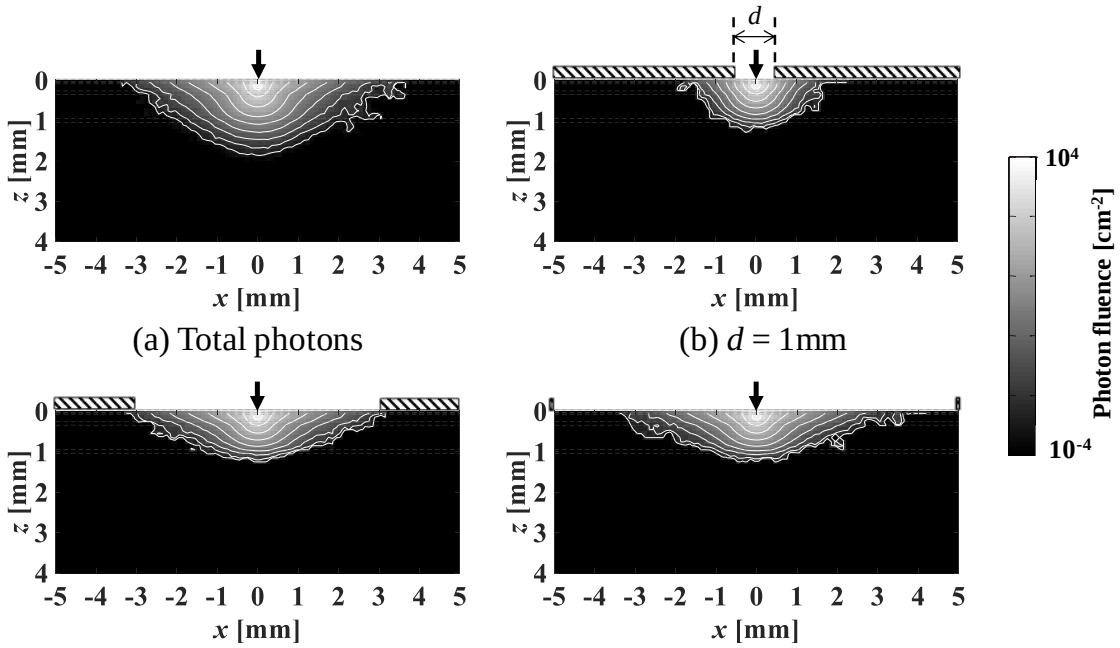

Fig. 3.4 Two-dimensional distribution maps of (a) the total photon fluence and (b) – (d) the detected photon fluence with d = 1, 6, and 10mm in diameter of the aperture, respectively, in 550 nm wavelength of a point-like illumination.

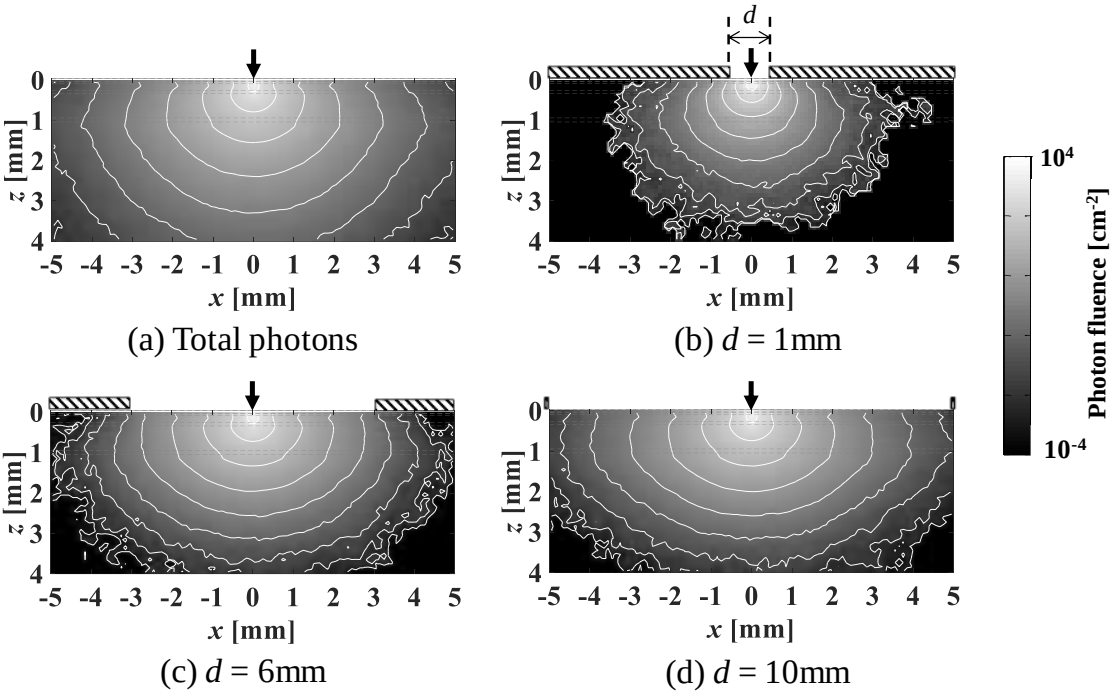

Fig. 3.5 Two-dimensional distribution maps of (a) the total photon fluence and (b) – (d) the detected photon fluence with d =1, 6, and 10mm in diameter of the aperture, respectively, in 700 nm wavelength of a point-like illumination.

3.3.3 Circular-spot Illumination

Figures 3.6 and 3.7 show simulated spectral reflectance curves with various diameters d of the detection area in cases of circular-spot illumination having d_i = 2 and 4 mm in diameter, respectively. In Fig. 3.6, reflectance curves for $d \leq 4$ mm significantly than those in Fig. 3.3. This is probably due to insufficient detection area with respect to the diffused light component which is produced by d_i = 2 mm diameter illumination. In Fig. 3.7, reflectance curves for $d \leq 6$ mm are clearly reduced in the same way as those for $d \leq 4$ mm in Fig. 3.6. This is also because of insufficient diameter for the detection with respect to d_i = 4 mm diameter illumination.

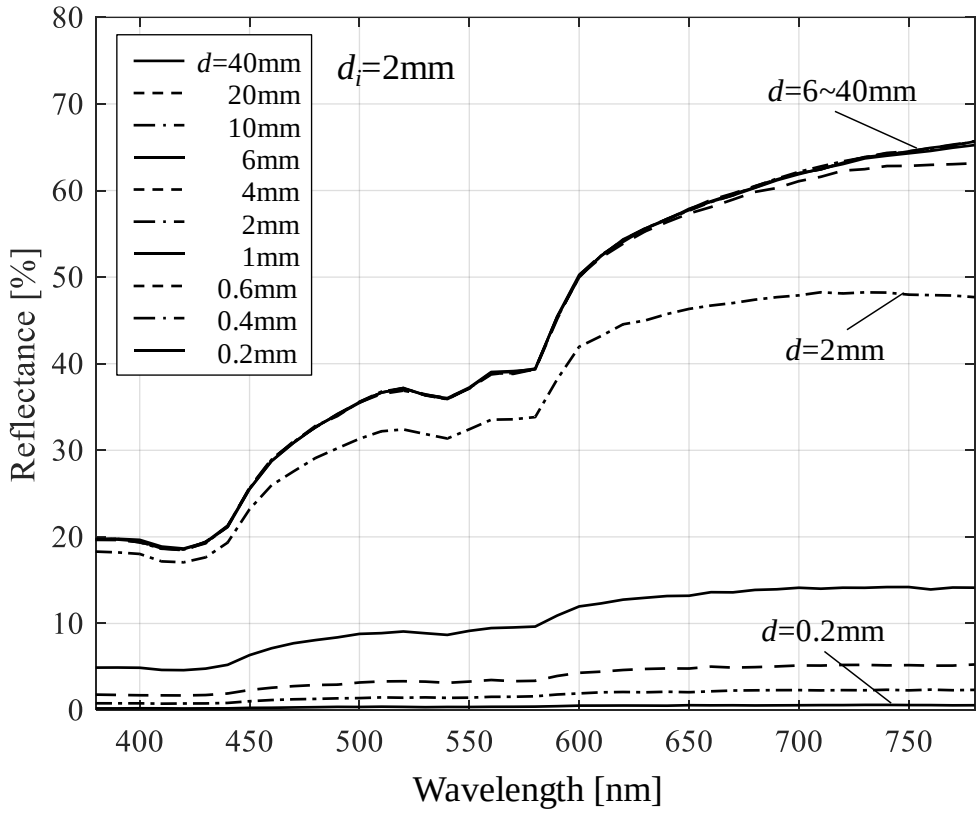

Fig. 3.6 Simulated spectral reflectance curves with different diameters d of a detecting aperture for a circular spot illumination of d_i = 2 mm in diameter.

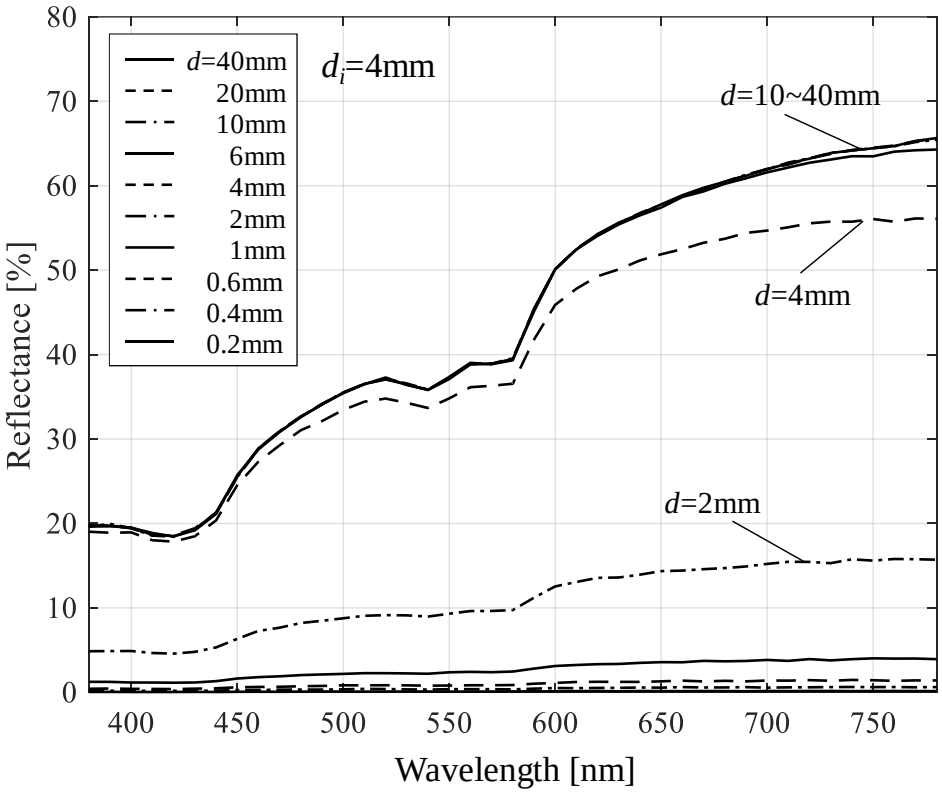

Fig. 3.7 Simulated spectral reflectance curves with different diameters d of a detecting aperture for a circular spot illumination of d_i = 4 mm in diameter.

Figures 3.8 and 3.9 give the photon fluence maps in 550 nm and 700 nm wavelength cases for d_i = 2 mm circular spot illumination. The maps in (a) of Figs. 3.8 and 3.9 show the total fluence while those in (b) to (d) show the detected fluence. By an areal illumination with d_i = 2 mm in diameter, the photon fluence demonstrates horizontally broaden distribution in comparison with those of Figs. 3.4 and 3.5. The fluence maps in 700 nm are again found to be more widely diffused than those in 550 nm.

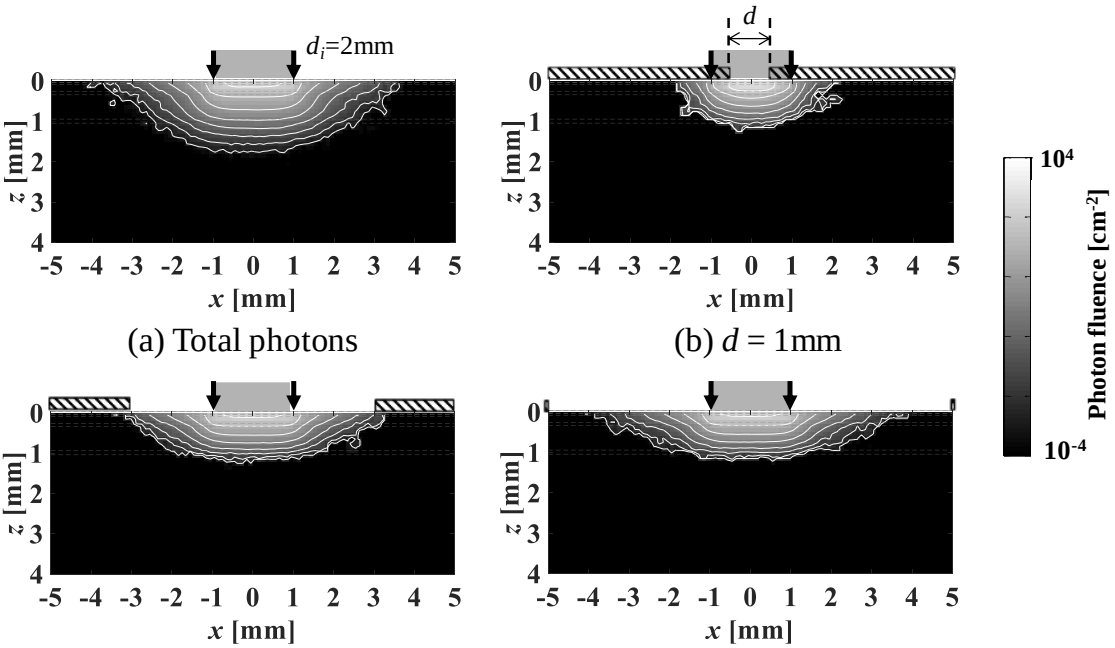

Fig. 3.8 Two-dimensional distribution maps of (a) the total photon fluence and (b) – (d) the detected photon fluence with d = 1, 6, and 10mm in diameter of the aperture, respectively, in 550 nm wavelength of a circular spot illumination of d_i = 2 mm in diameter.

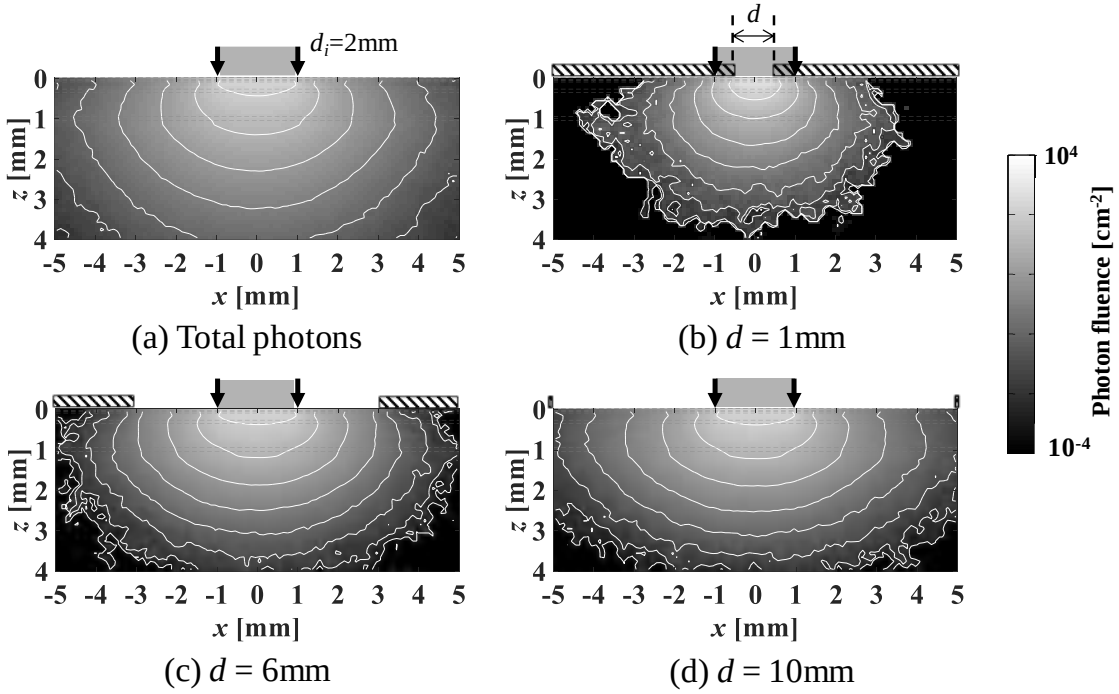

Fig. 3.9 Two-dimensional distribution maps of (a) the total photon fluence and (b) – (d) the detected photon fluence with d = 1, 6, and 10mm in diameter of the aperture, respectively, in 700 nm wavelength of a circular spot illumination of d_i = 2 mm in diameter.

Figures 3.10 and 3.11 show the maps in 550 and 700 nm wavelength cases for d_i = 4 mm circular spot illumination. An increase of diameter from 2 to 4 mm results in further broadening of the photon fluence distribution in a horizontal direction. The diameter d of 6 mm or more in the detection area is probably necessary for receiving substantial amount of the diffused light component coming back to the surface.

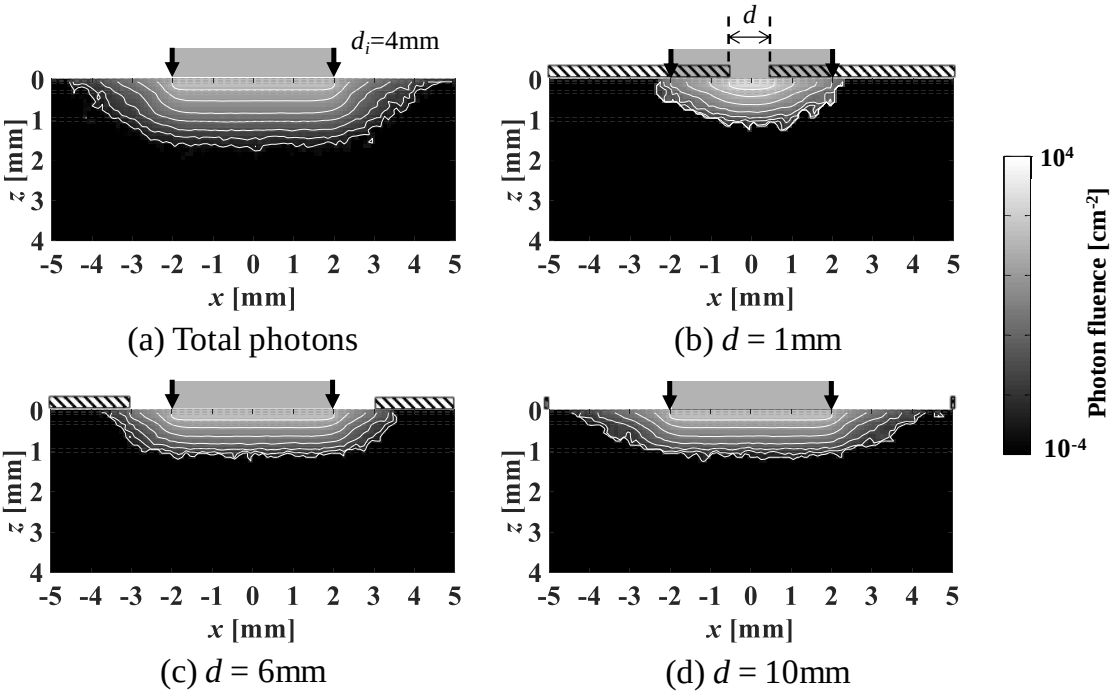

Fig. 3.10 Two-dimensional distribution maps of (a) the total photon fluence and (b) – (d) the detected photon fluence with d = 1, 6, and 10mm in diameter of the aperture, respectively, in 550 nm wavelength of a circular spot illumination of d_i = 4 mm in diameter.

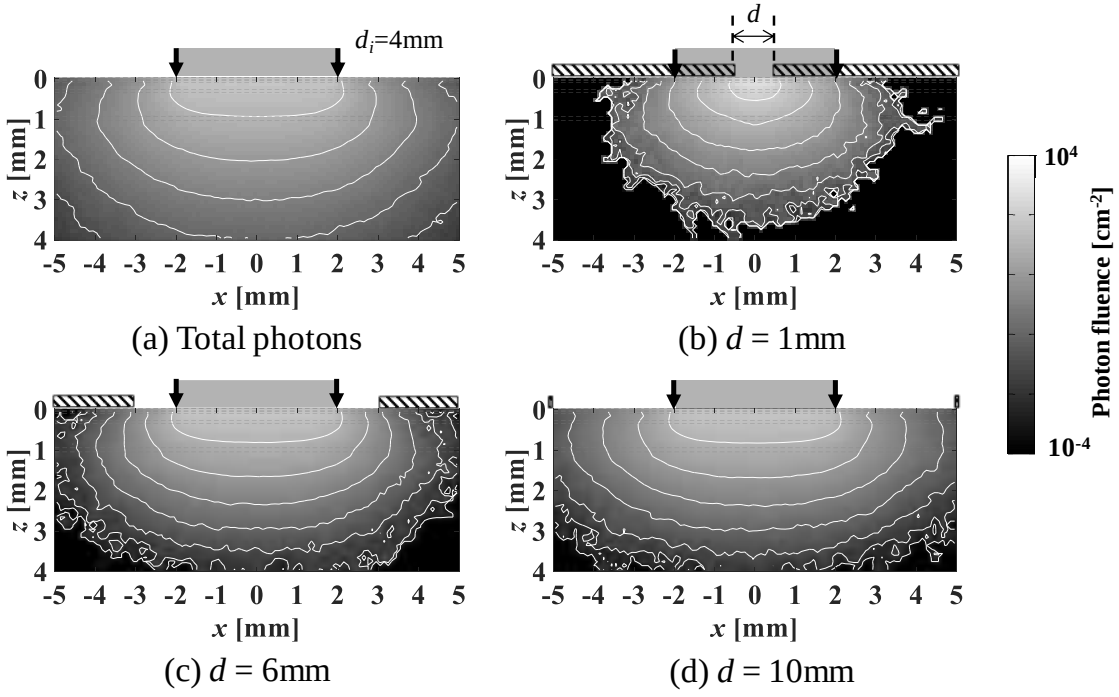

Fig. 3.11 Two-dimensional distribution maps of (a) the total photon fluence and (b) – (d) the detected photon fluence with d =1, 6, and 10mm in diameter of the aperture, respectively, in 700 nm wavelength of a circular spot illumination of d_i = 4 mm in diameter.

3.4 Experimental Investigation

3.4.1 Method and Apparatus

Figure 3.12 shows a measuring apparatus for the spectral reflectance using an integrating sphere and spectrophotometer. Light from a halogen lamp source (Hayashi LA-150UX) was focused by lens to skin surface with a circular spot of d_i = 4 mm in diameter via a sample window of a 6-inch integrating sphere (Labsphere RT-060-SF). Diffusely reflected light from the skin was received at the detection port by a fiber probe having 400 μm diameter. The detected area was changed by setting detecting aperture having diameters d = 4, 5, 6, 8, 10, 15, and 22 mm on the sample window. The received light was transmitted into a multichannel spectrophotometer (Ocean optics USB-4000), which measures spectral reflectance in a visible wavelength range of 380-780 nm.

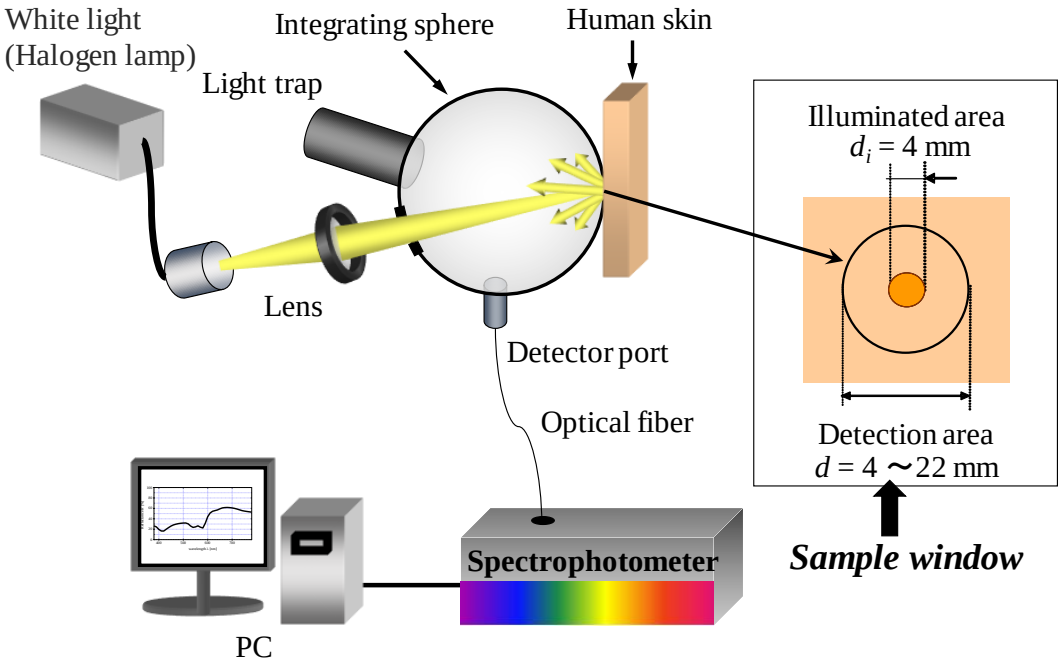

Fig. 3.12 Measuring apparatus for spectral reflectance using a 6-inch integrating sphere.

3.4.2 Results

Figure 3.13 shows spectral reflectance curves measured by different diameters d of the detecting aperture on the human forearm skin. Measured reflectance decreases as the detecting aperture becomes small. This decrease is significant in the wavelength range longer than 600 nm. The curves with d = 10, 15, and 22 mm seem to have almost the same behavior. The absolute values in reflectance are different between simulated curves in Fig. 3.7 and measured ones in Fig. 3.13 for the same detecting aperture diameter. However, the simulation and measurement demonstrate the same reduction behavior in reflectance especially in the longer wavelength range with insufficient size of the detection area. It can be seen that the appropriate diameter of a detecting aperture is estimated to be 10 mm or more from both the simulated and measured results in case of d_i = 4 mm spot illumination. This estimation is of course dependent on the size of illuminating spot. However, a necessary margin of the detection area is supposed to be about 4 to 6 mm by considering the broadening in the diffused light in skin tissue. Therefore, the appropriate diameter for detection area is estimated to be the sum of illuminating spot diameter and this margin of 4 to 6 mm for human skin.

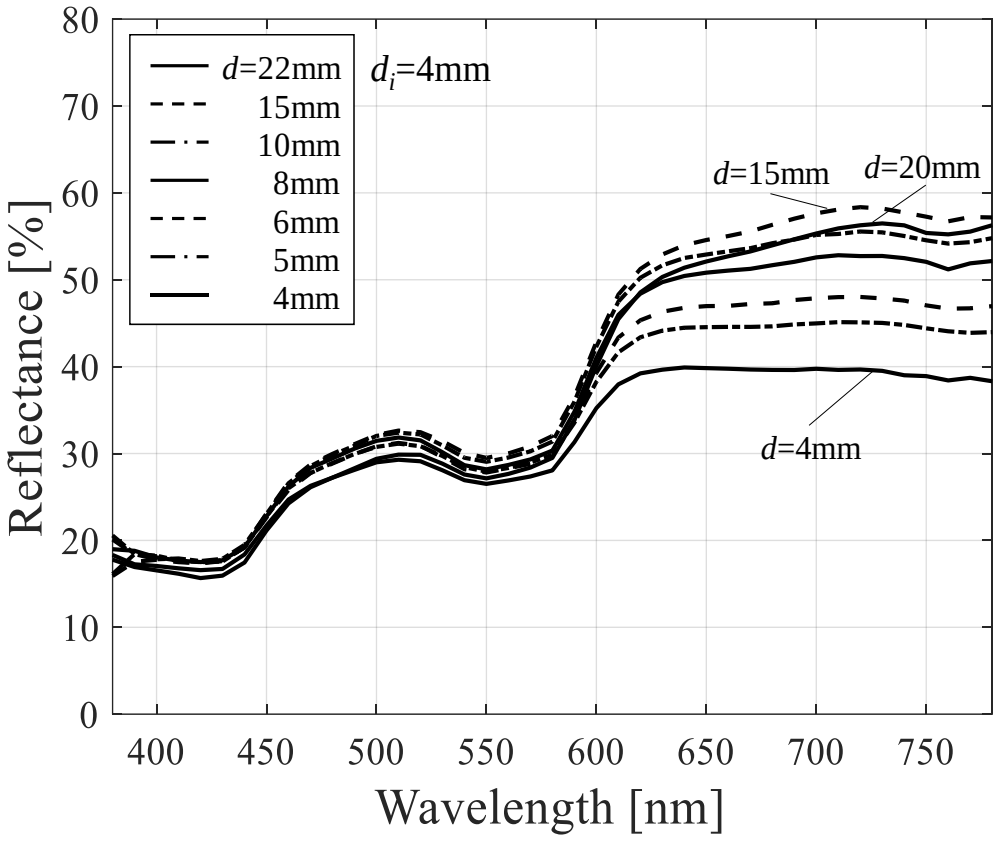

Fig. 3.13 Measured spectral reflectance curves with different diameter d of a detecting aperture for a circular spot illumination of d_i = 4 mm in diameter on a human forearm skin.

3.5 Conclusion

This chapter investigated effects of the detecting aperture size on spectral reflectance curves in human skin tissue by Monte Carlo simulation and simple spectrophotometric experiments on human forearm. Undesirably small size of detecting aperture causes reduction of measured reflectance especially in the longer wavelength range. The necessary size is probably given by the sum of an illuminating spot size and a detection margin of 4 to 6 mm which results from the broadening of diffused light in the skin tissue. This estimation is useful for reliable measurement of spectral reflectance in skin tissue in the fields of dermatology and cosmetic product development. The study presented in this chapter is specific to human skin and may have some different properties for different objects to be measured. However, the same kind of investigation and discussion may be effective for the other objects.

Chapter 4

Simulated Reflectance Spectra and Point Spread Functions in Database Constructed by Moderate Grouping of Nine Layers in Skin Model

4.1 Introduction

Over the years, multiple studies [49,51,52,55,125,130] have been carried out on how the appearance of human skin reflects physiological condition in the tissue, using optics as an effective tool. Generally, the skin tissue is analyzed by measuring spectral reflectance in a visible wavelength range. Analysis of spectral reflectance provides a variety of knowledge about skin condition such as skin color, skin diseases and skin aging. The spectral reflectance is governed mainly by absorption and scattering coefficients in the skin tissue which are very closely related to the concentration of typical chromophores as melanin and hemoglobin and the tissue morphology which may alter under various skin diseases and conditions [64-67]. In this respect, the skin spectral reflectance is a definitely useful measure for diagnostics of skin diseases in dermatology and monitoring of the skin color and tissue conditions in the cosmetic field. It is, however, generally difficult to analyze directly skin tissue conditions including pigment concentration and tissue structural abnormality from measured spectral reflectance. Thus, several different methods have been studied on a relation between the skin condition and spectral reflectance [131-132].

Shimada *et al*. [57-59] presented studies on the multiple regression analysis for assessment of melanin and blood concentration in human skin. This type of linear

regression method became popular and further studied by some groups [73-76] for estimation of skin conditions. Tsumura *et al*. [56] studied independent-component analysis of skin color image for evaluating melanin and hemoglobin distribution on human face. The regression methods are influenced by ranges of parameters used to derive the regression equation. In contrast to these approaches, Zhang *et al*. [68,69] presented the method using the diffusion approximation, and Magnain *et al*. [70,71] studied the solution of the radiative transfer equation by use of the auxiliary function method for determination of skin optical properties and skin color. These approaches are theoretically clarified, but have some limit in application. Ohtsuki *et al*. [133] reported application of the Kubelka-Munk theory for estimation of pigment concentrations. This method has difficulty in use for an inhomogeneous skin tissue model.

The above-mentioned various approaches have the common drawback of difficulty in application to various skin conditions including normal to abnormal. To overcome the difficulty, a group of Zhang *et al*. [68,69] developed their idea to library based spectral fitting for determination of optical properties in their framework of the diffusion model. They showed reasonable estimation of nine skin parameters by genetic algorithms, but their skin model was limited to the layers of epidermis and dermis. Magnain *et al*. [70,71] tried to develop their skin model from 5 to 22 layers in their treatment of the radiative transfer equation with the auxiliary function method. They discussed the shape of reflectance spectra in detail with relation to skin parameters. In their model, however, the optical parameters are not discriminated layer by layer. Thus, the effect of absorption and scattering in each layers are only qualitatively discussed on the total spectral shape.

Changes of skin condition from normal to abnormal are primarily estimated by

absorption and scattering coefficients in skin tissue. The absorption coefficient is defined as a product of molar extinction coefficient and molar concentration of chromophore such as melanin in epidermis and oxygenated and deoxygenated hemoglobin in dermis. The scattering coefficient is closely related to tissue structure having various cells since light scattering occurs at the boundary between different refractive-index media. It is, thus, desirable that a method for analysis of spectral reflectance guarantees a scalable range of values estimated for the absorption and scattering coefficients. To this aim, the Monte Carlo method is advantageous for numerical simulation of light propagation in skin tissue [11]. Meglinski and Matcher [123,129] presented simulation of reflectance spectra using a seven-layered skin model. Their approach is useful for analyzing elemental factors of absorption and scattering layer by layer, but they assumed wavelength-independency of scattering condition. To make more realistic simulation, Maeda *et al*. [122] developed the nine-layered model with the set of five parameters (absorption coefficient, scattering coefficient, anisotropy scattering parameter, refractive index, and thickness) layer by layer. By adjusting a value of each parameter, they demonstrated well simulated spectra similar to the measured spectra. We use this approach to estimate the absorption and scattering coefficients layer by layer, since we consider that the five parameters used for producing the well-simulated spectrum give reasonable candidate values for the measured spectrum. However, a manual iteration is quite time-consuming and unstable process for finding a simulated spectrum well similar to the measured spectrum.

By referring to the idea used in the work of Zhang [69], in this study, a skin reflectance spectral database has been constructed in the framework of the nine-layered skin tissue model which is used for determining the absorption and scattering coefficients of a measured spectrum by spectral mining in the database. To build a reasonable size of

database, we propose a moderate grouping method [134] for nine layers by using two magnification factors to the absorption and scattering coefficients. This database suffers from uncertainty or ambiguity in identification of a simulated spectrum which seems close to a measured spectrum since two or more different combinations of absorption and scattering coefficients produce similar reflectance spectra [135] in simulation. To resolve this situation, we also discuss in this paper possibility of using a point spread function (PSF) of reflected intensity on the skin surface, which strongly exhibits scattering property of skin tissue rather than the absorption.

4.2 Simulation Model for Spectral Reflectance

4.2.1 Skin Tissue Model

Human skin tissue has a very complex structure with different optical properties to contribute to its light propagation nature. Previously it was known that human skin tissue was modeled of three layers such as epidermis, dermis and subcutaneous layers, as can be seen in Fig. 2.12(c). To imitate human skin condition with better accuracy, a nine-layer model [122] has been taken into account as shown in Fig. 2.12(b) and each layer has its own separate thickness and optical properties. This nine-parallel layered model was used for performing simulation of spectral reflectance and PSF in this study. More detailed explanation regarding nine-layered skin model has been described in Section 2.7 of Chapter 2, including information about all the necessary optical properties.

4.2.2 Monte Carlo Method for Simulation of Reflectance

In the Monte Carlo simulation (MCS) of light propagation in tissue media [10,136-140], light is treated as a bundle of photons. Pseudo random numbers generated by a computer statistically determine trajectories of photons in the media, which are characterized by optical properties such as absorption coefficient and scattering coefficient. A conceptual diagram of the MCS method for light propagation in multi-layered tissue is described in Fig. 3.1 [11]. A photon bundle of unit energy (W_1=1) enters the tissue and undergoes scattering and absorption. A travel distance in which the photon undergoes neither an absorbing event nor a scattering event is defined as the free path length and denoted by a step size s. This length s is given by $-\ln(\xi) / (\mu_s + \mu_a)$ with a random number ξ ranging from 0 to 1 with scattering coefficient μ_s and absorption coefficient μ_a. After traveling the path length, the photon energy is assumed to be attenuated at a rate of $\mu_s / (\mu_s + \mu_a)$ determined by scattering and absorption coefficients. If the resultant energy is smaller than a preset threshold (10^{-6} used in this study), then this photon bundle is regarded as negligibly attenuated, and the second photon bundle enters the tissue. When the energy is still larger than the threshold, propagation continues and new traveling direction (θ, ψ) is given by random numbers, where θ is the deflection or polar angle and ψ is the azimuthal angle. By accumulating the energies of photons that are emitted from the top surface to the detection side, reflectance is calculated with reference to the total energy of incident photons. This process is performed at each of the necessary points of wavelength λ, and thus spectral reflectance is obtained numerically.

In this study, the above process is performed in the wavelength range of 400-700nm at an interval of 10 nm. To obtain stable simulation results, 10^5-10^7 photons are

usually necessary from our experience. For the MCS, we used the algorithm of Wang *et al*. [11], in which the five input parameters must be specified at each wavelength for each layer: scattering coefficient μ_s, absorption coefficient μ_a, anisotropy scattering parameter g, refractive index n, and thickness t. Furthermore, oxygen saturation Sat-O_2 should also be specified. g is the average cosine value of the phase function P(θ), and it ranges from −1 to +1, corresponding to the perfect backscattering and forward scattering. By following the algorithm of Wang *et al*., we employ the Henyey-Greenstein function [110] as a well-known approximated form of the phase function, thus, g is characterized by this function. As is known usually, typical resultant values of g are 0.7-0.8 for tissue and greater than 0.9 for blood. Each value of g for each layer is set by published data [123,141-144] and our experience, which is shown later in this chapter. The refractive index n is a wavelength-dependent function but is assumed to be constant in the wavelength range used, while set different layer by layer. For specifying values of these input parameters, we surveyed several articles having some plausible values at specific wavelength points [76,123,127,141-146] and, then modified them in experiments and simulations so that some simulated spectra could match measured sample spectra [122]. We employ these values as a standard condition, as can be seen in Section 4.3. Then, one of the parameters in a specified layer was varied from the standard value and the others were fixed to be the standard, and MCS was carried out to produce many spectral reflectance curves for various cases.

4.3 Simulated Reflectance Spectra and PSF in a Standard Condition

Figure 4.1 depicts a typical example of simulated reflectance spectrum and point spread functions in three different wavelengths in the standard condition. Table 4.1 represents example of the input data set (5 parameters in each of nine layers) in a specific wavelength (700nm) used as the standard condition. It is noticed that four optical parameters except for thickness have wavelength dependency nature. Their spectral properties are shown in our preceding work [122]. In Fig. 4.1(a), the spectral reflectance is low in the shorter wavelength range and large in the longer wavelength range while showing a well-known 'W'-like shape coming from the absorption characteristics of oxygenated hemoglobin [147]. These features of the spectrum resemble to typical appearance of a human skin spectrum. For the PSFs in Fig. 4.1(b), the vertical axis is normalized by the maximum intensity of each PSF curve and also its intensity decay is presented in a range of 0-1mm in x axis, in which x=0 means the center point of an illuminating spot having a diameter of 0.8 mm. As it is known that the PSF has wavelength dependency due to the nature of optical path length in tissue. With the longer wavelength, the PSF curve becomes broadened and is desirable for estimating change of skin condition, which is described later. By this reason, the wavelength of 700nm is chosen for the investigation on simulated PSF conducted in this study.

Table 4.1 Input data-set for nine layers at 700nm in the standard condition.

Layer	Refractive Index (n)	Absorption coefficient (μ_a) [cm^{-1}]	Scattering coefficient (μ_s) [cm^{-1}]	Anisotropy factor (g)	Thickness (t) [cm]
L1	1.5	0.27	108.10	0.88	0.0015
L2	1.34	2.35	81.10	0.82	0.006
L3	1.34	21.1	432.30	0.82	0.0015
L4	1.4	0.37	1426.60	0.92	0.0045
L5	1.4	0.30	2118.20	0.92	0.0175
L6	1.39	0.41	2593.74	0.97	0.008
L7	1.4	0.29	2377.60	0.82	0.06
L8	1.38	0.37	2550.51	0.97	0.01
L9	1.44	0.32	2191.43	0.77	0.6

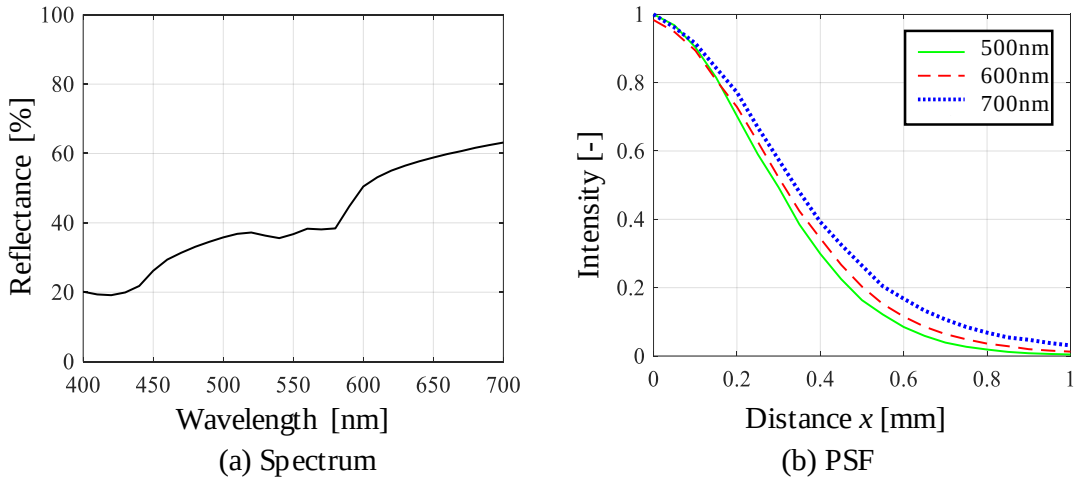

(a) Spectrum (b) PSF

Fig. 4.1 Typical spectrum and PSFs in different wavelengths simulated with standard values in parameters.

4.4 Construction of Database

4.4.1 Spectral Fitting

It is known that a measured reflectance spectrum is used to derive the content of melanin and hemoglobin in skin tissue by using, for example, multi-variate analysis. However, preparation of regression matrix is usually a difficult task for general purposes. We studied the MCS-based spectral fitting method [148] in which a simulated spectrum can be produced so that it agrees well with the measured spectrum by means of manual iteration in the MCS. Finally-accepted spectrum is referenced to provide its absorption and scattering coefficients, μ_a and μ_s in each of nine layers. This approach provides flexible fitting potentiality, but it is difficult to adjust appropriately values of five parameters in each of the nine layers. Knowledge obtained from the simulated spectral library [149] may probably be helpful for decreasing the iteration cost, but it requires sufficient experience. So, the fitting is yet time-consuming and less reproducible.

4.4.2 Spectral Database

To improve the process of identifying the spectrum agreeing well to a measured spectrum, we employ a spectral database method in which the most plausible spectrum is extracted from the database with a criterion of root mean square error (RMSE), which is defined here by

$$RMSE = \sqrt{\frac{1}{m}\sum_{i=1}^{m}\{R_s(\lambda_i) - R_t(\lambda_i)\}^2} \quad , \tag{4.1}$$

where $R_s(\lambda_i)$ and $R_t(\lambda_i)$ are simulated and target (measured) spectra, respectively, and λ_i indicates an i-th discrete value of wavelength and m is the total number of discrete wavelength points contained in the spectral data. We recognize a condition of RMSE ≤ 1% as acceptable agreement criterion in the beginning for all the target spectra, since this criterion extracts simulated spectra very close to the target spectrum in our preceding works [134,135]. With this criterion, we consider that one or more simulated spectra can be extracted from the database for the measured spectra in general. However, it may also be the case with no extraction for RMSE ≤ 1%. For this case, we consider two optional approaches. One is to increase the number of data by enlarging the range of optical parameters in simulation. Another is to loosen the condition of RMSE, for example ≤ 2 ~ 3%, though the estimation accuracy may be degraded.

To construct the database, we intended to prepare a great number of spectral data by using various values uniformly for all the five parameters (μ_a, μ_s, g, n, and t) in each of the nine layers. However, this is unrealistic since the database may potentially contain a number of useless spectral data, which correspond to unreal skin conditions, and cause unnecessary effort for spectral matching. Then, we carefully considered the behaviors of reflectance spectra in the above-mentioned library [149]. Among the five parameters, the absorption coefficient μ_a and scattering coefficient μ_s are considered as the primary factors to find changes in the skin condition. The rest three parameters g, n, and t are also related to some changes in skin, but we consider that probably they do not yield

substantial changes in their values that can be found from a spectral change. Therefore, we assume that anisotropic scattering parameter g, refractive index n, and layer thickness t take constant values with keeping different values layer by layer, and we change values of the absorption and scattering coefficients, μ_a and μ_s in the nine layers. By this assumption, the number of parameter values to be changed is reduced from 45 (5 parameters by 9 layers) to 18 (2 by 9). In the constructed database, each spectrum is contained with its associative data-set of 45 parameter values. Once a simulated spectrum matched to the measured spectrum is found in the database, we can obtain 45 values for the five parameters in the nine layers. To construct a reasonable size and easy-to–use database with keeping this unique advantage of the nine-layered skin model, we propose a moderate grouping method [134] for the nine layers by using two magnification factors M_a and M_s for the absorption coefficient μ_a and scattering coefficient μ_s, respectively. Change of values in μ_a and μ_s is performed by M_a and M_s in terms of μ_a multiplied by M_a and μ_s multiplied by M_s, respectively. It is known that the absorption coefficient μ_a is characterized by melanin in epidermis and hemoglobin in dermis and subcutaneous layer. To change a value of μ_a in a convenient way, we set two groups of layers, L_1 – L_3 and L_4 – L_9 and change the value of the absorption coefficient μ_a by magnification factors, specifically denoted in $M_{a,1\text{-}3}$ and $M_{a,4\text{-}9}$, respectively. It is supposed that the scattering coefficient μ_s is closely related to tissue structure and is characterized by three regions of epidermis, the upper dermis, and the lower dermis followed by subcutaneous fat layer. For the scattering coefficient μ_s, we set three groups of layers, L_1 – L_3, L_4 – L_6, and L_7 – L_9 and change the value by magnification factors, specifically denoted in $M_{s,1\text{-}3}$, $M_{s,4\text{-}6}$, and $M_{s,7\text{-}9}$, respectively. Each of these takes a range for varying values as given in Table

4.2.

Table 4.2 Magnification values used for producing database. I_L is intervals where L indicates a grouping range of layers.

Layers	M_a	M_s
1~3	0.6 ~ 1.6 ($I_{1\text{-}3}$= 0.10)	0.6 ~ 1.4 ($I_{1\text{-}3}$= 0.10)
4~6	0.2 ~ 3.6 ($I_{4\text{-}9}$= 0.20)	0.3 ~ 9.3 ($I_{4\text{-}6}$= 0.30)
7~9		0.1 ~ 1.0 ($I_{7\text{-}9}$= 0.10)

It should be noted that, this grouping of μ_a (in 2 groups) and μ_s (in 3 groups) makes the magnification in each group uniform but keeps the condition of different values for μ_a and μ_s in all the nine layers. To determine the number of the discrete steps, first we evaluated the range of change for each magnification factor so that a difference range between the minimum and maximum reflectance spectra could cover all the target spectra used in this study. Then we set the smallest discrete step available (0.1 in this study) for each magnification factor. However, the ranges of $M_{a,4\text{-}9}$ and $M_{s,4\text{-}6}$ are larger than those of the other magnification factors, and it results in the larger number of steps, which increases the computation cost and the database size. So, we optimized and finally

employed the step to be 0.2 for $M_{a,4\text{-}9}$ and 0.3 for $M_{s,4\text{-}6}$. In this study, the number of discrete steps for changing is 11 for $M_{a,1\text{-}3}$, 18 for $M_{a,4\text{-}9}$, 9 for $M_{s,1\text{-}3}$, 31 for $M_{s,4\text{-}6}$, and 10 for $M_{s,7\text{-}9}$, and therefore, the database accumulates totally 552,420 spectral curves. It is also noted that a ratio of μ_a- or μ_s-values in layers within each group is maintained when this group-based changing of parameters are performed. So, the advantage of having nine layers as a skin model is guaranteed in this database. As mentioned earlier, the wavelength for all spectral reflectance curves is in a range of 400-700nm at an interval of 10 nm (31 wavelength points) to make the size of database reasonable. Figure 4.2 shows some examples of simulated spectra included in the constructed database. These examples were selected to represent in the figure a variety of simulated spectra contained in the proposed database, and have a difference range about 10-15% in reflectance over the wavelength of 400nm-700nm. As a special mention, the thickness t is not only different in individual but also has variance in different positions of body. So, it is difficult to incorporate such variance in the present constructed database. Estimation of μ_a and μ_s values are made under the condition of fixed thickness values, since this version of database treats only the change in μ_a and μ_s values but keeps fixed values for g, n, and t, which may be related to a standard virtual person. At least, with this present version we can observe relative change in μ_a and μ_s values in each of different subjects. In the near future, we intend to develop an advanced version of database, where change in thickness values will be incorporated.

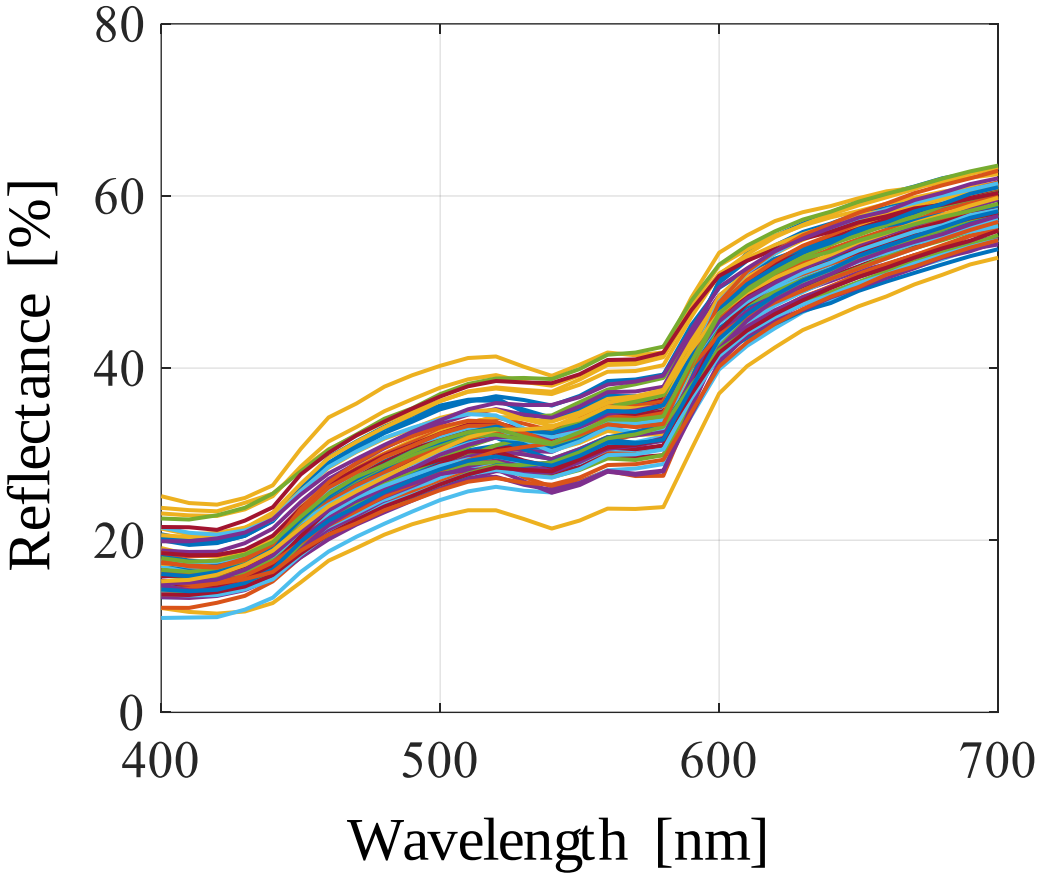

Fig. 4.2 Example of spectral reflectance in database.

4.4.3 Numerical Validation Experiment

To estimate the performance of the constructed database, we need target spectral samples as measured ones. In this study, we referred to published measured spectral

reflectance samples (459 curves) of Japanese women's cheek which are included in SOCS (standard object colour spectra) library [150] and commercially available. To test these samples as target spectra for validation experiments, we need knowledge on their input values corresponding to the five simulation parameters for the nine layers. The SOCS data do not contain this information. Instead of using directly 459 raw data in SOCS, we selected 459 substitutive simulated spectral data from the constructed database so that they are most similar to the 459 raw data in the SOCS one by one. Then, we chose a target spectrum as a test data one by one from those of 459 selected data, and performed the data mining from the database of 552,420 – 1 spectra by the criterion of the minimum RMSE. Here we employed the leave-one-out method in the partial cross validation, so we excluded the target spectrum itself in the mining process. The extracted spectrum seems to be very similar to the target spectrum, but not the real target spectrum. This process was repeated one by one for each the of 459 selected spectra. Each of the extracted spectra holds its five magnification factors in the database. So, we compared values of the five magnification factors between the extracted and the target spectra and evaluated its difference as an estimation error $\Delta M_{c,L}$ defined by

$$\Delta M_{c,L} = \frac{M^*_{c,L} - M_{c,L}}{I_L} \quad , \tag{4.2}$$

where $M^*_{c,L}$ and $M_{c,L}$ are magnification values of the target and extracted spectra, respectively, subscript c indicates 'a' for absorption and 's' for scattering, and L is a group of layers. I_L is a changing unit or interval of magnification which is the gap between two consecutive discrete steps in each of the five magnification factors. This is used to divide the difference between magnification values of the extracted and target spectra in Eq.

(4.2) so that the estimation error could be expressed in a normalized form and compared among all the five magnification groups that have different ranges of magnification values.

Figure 4.3 shows estimation error distributions of the 459 extracted magnification values for the absorption coefficient in two groups and scattering coefficient in three groups. The peak of the distribution was found to appear at the center (which indicates error of 0%) in Figs. 4.3(a)-4.3(d). This indicates that the absorption and scattering coefficients can be appropriately estimated for the target spectrum by using the constructed database, except for the scattering coefficients in the deeper layers, L_7- L_9 in Fig. 4.3(e). It seems difficult to estimate correctly μ_s-value in the deeper three layers because of experience of multiple scattering through relatively long path length of photons. In Figs. 4.3(a) and 4.3(c), the results show a case with no error, and indicate that values of $M_{a,1\text{-}3}$ and $M_{s,1\text{-}3}$ for all the 459 extracted spectra are correctly assigned to those for the 459 target spectra. This is slightly questionable. It probably comes from the nature that the absorption and scattering of light in the upper layers of the skin are strongly reflected on the shape of reflectance spectrum. We consider that the same kind of validation experiments should further be made with addition of noise in the near future. For example, if a certain amount of noise is randomly added to the target spectrum, we consider that our mining still extracts a similar spectrum from the database. So, the magnification factors are estimated from the extracted spectrum, but we may see the larger estimation error due to the added noise. It is also noticed that the estimation error $\Delta M_{c,L}$ in Eq.(4.2) is defined as a normalized value by the magnification interval I_L given in Table 4.2.

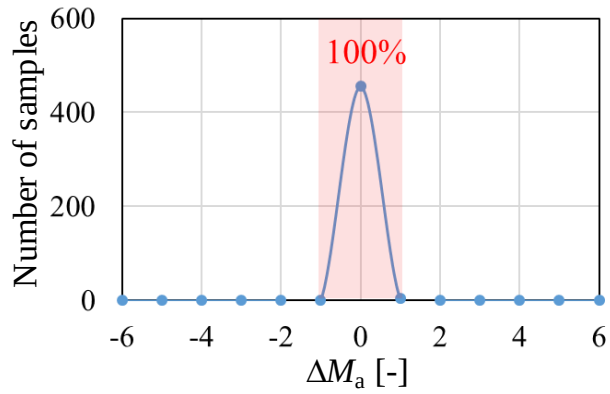

(a) Case of ΔM_a [-] in layers L_1-L_3

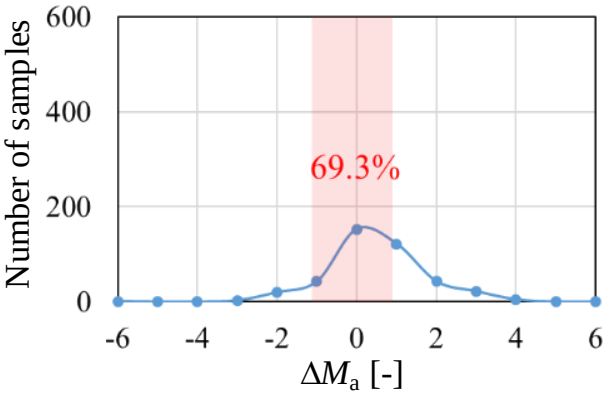

(b) Case of ΔM_a [-] in layers L_4-L_9

Fig. 4.3 Distribution diagrams of M_a and M_s.

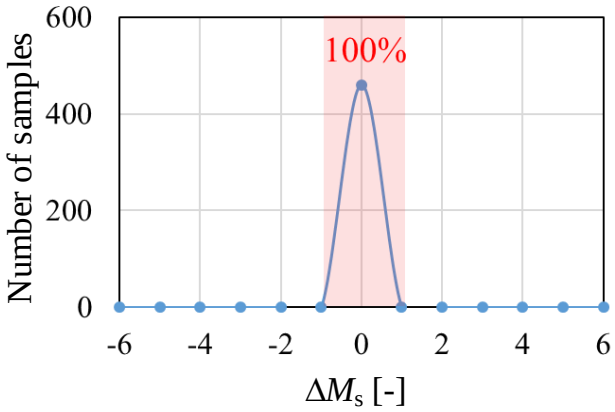

(c) Case of ΔM_s [-] in layers L_1-L_3

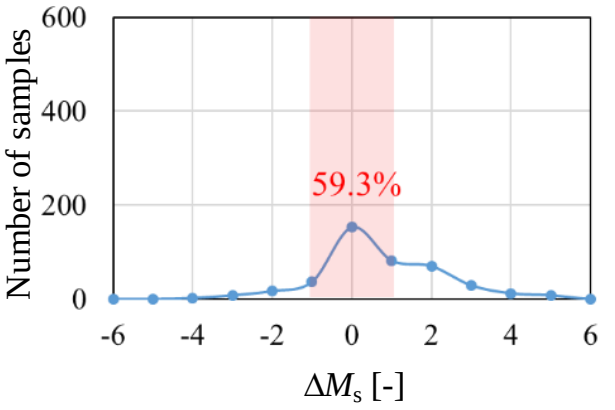

(d) Case of ΔM_s [-] in layers L_4-L_6

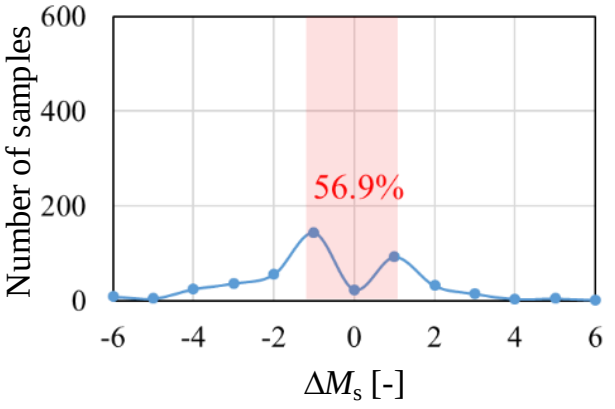

(e) Case of ΔM_s [-] in layers L_7-L_9

Fig. 4.3 Distribution diagrams of M_a and M_s.

4.4.4 Ambiguity Problem and Identification with PSF

Although the spectral database is promising for extraction of the simulated spectrum similar to the measured spectrum, we found the problem that some different sets of μ_a and μ_s values produce the similar reflectance spectra in the database. This can be an ambiguity problem for extracting correctly the desirable simulated spectrum from the database. Figure 4.4 demonstrates a typical example of the three similar spectra, which are simulated with values of μ_a and μ_s changed by different magnification factors given in Table 4.3.

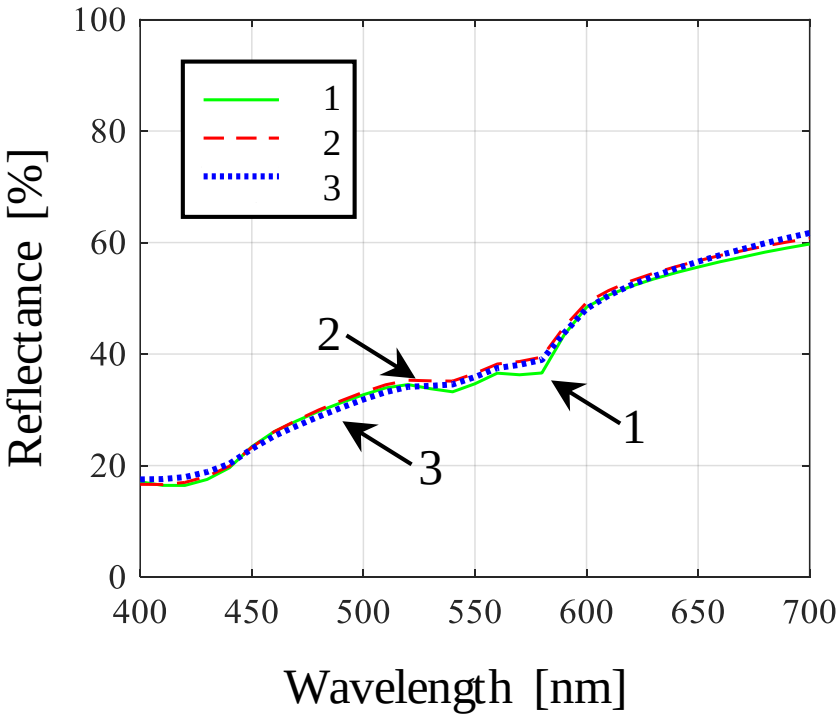

Fig. 4.4 Examples of similar spectra simulated with different values of M_a and M_s.

Table 4.3 Different magnification values of M_a and M_s for μ_a and μ_s, respectively.

	Magnification values				
	μ_a		μ_s		
Reflectance curve	$M_{a,1\text{-}3}$	$M_{a,4\text{-}9}$	$M_{s,1\text{-}3}$	$M_{s,4\text{-}6}$	$M_{s,7\text{-}9}$
1	1.1	0.4	0.8	0.3	0.6
2	1.3	1.6	0.8	4.8	0.1
3	1.4	2.2	1	9.3	0.2

To access this problem, we investigated changing behaviors of simulated spectra and also a simulated point spread function (PSF) of reflected intensity on the surface of the skin model, with the above-mentioned five magnification groups. In general, the PSF is known to reflect the scattering property of skin tissue. The PSF is simulated in this study at wavelength of 700 nm under the condition of circular spot illumination with Gaussian nature having a standard deviation of σ = 0.4 mm in the direction normal to the skin surface. We regarded this spot size as point-like illumination. If the PSF with a real point illumination is necessary, the deconvolution process can be used. Figures 4.5 and 4.6 show typical spectra and PSFs with different values of $M_{a,1\text{-}3}$ and $M_{a,4\text{-}9}$, respectively. In Fig. 4.5(a), the reflectance changes in the whole wavelength range which is probably

due to the effect of melanin. This type of spectral change is assigned to “Type A” here. In Fig. 4.6(a), the reflectance demonstrated its large change especially in the middle wavelength range of 500-600nm, and assigned to “Type B”. Almost no change is found in PSFs of Figs. 4.5 and 4.6. This means that change of absorption coefficient μ_a is not reflected on the PSF curves. Figures 4.7, 4.8, and 4.9 show typical spectra and PSFs obtained by changing values of $M_{s,1\text{-}3}$, $M_{s,4\text{-}6}$, and $M_{s,7\text{-}9}$, respectively. It is found that the reflectance changes in a specific range of wavelength with respect to the three groups of layers. The spectral changes by $M_{s,1\text{-}3}$ are found in the shorter wavelength range, those by $M_{s,4\text{-}6}$ in the middle, and those by $M_{s,7\text{-}9}$ in the longer, and are respectively assigned to “Type C”, “Type D”, and “Type E” here. It should be here noticed that the two changing types B and D of spectra seems to be very similar to each other in Figs. 4.6(a) and 4.8(a). We consider that this can probably be a cause of producing the similar spectra. In Fig. 4.6(a), the reflectance decreases in the middle wavelength range with increasing value of M_a, while in Fig. 4.8(a), it decreases in the same range with decreasing value of M_s. The magnification factor $M_{a,4\text{-}9}$ changes the value of absorption coefficients in the whole dermal layers and subcutaneous fat layers at the same time. But the primary effect by this change probably occurs in the upper dermal layers of $L_4 – L_6$. Therefore, an increase or decrease of μ_a and μ_s in the upper dermal layers makes an opposite effect on the reflectance in the middle wavelength range. This significant finding elucidates that it is difficult to discriminate between the change of μ_a and that of μ_s in the upper dermis from the spectral reflectance changes. We considered that the broadened distribution of estimation errors in Figs. 4.3(b) and 4.3(d) are also due to the same cause.

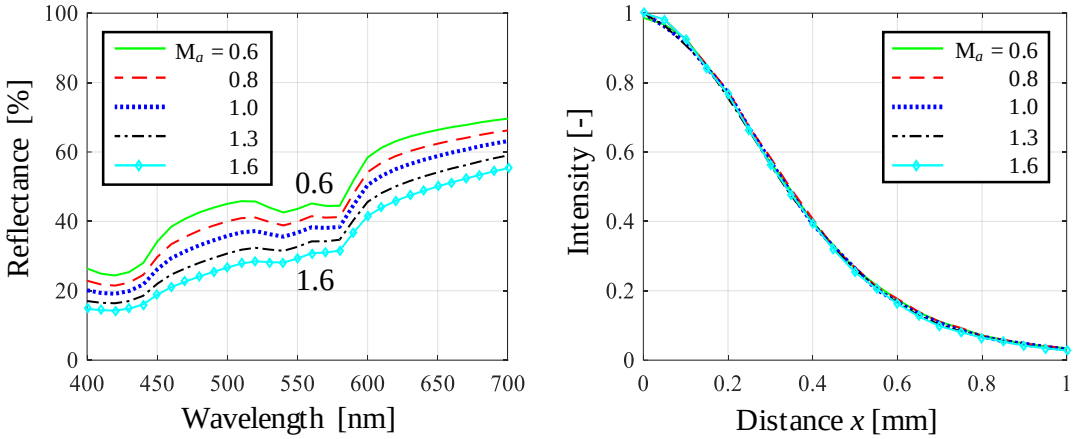

Fig. 4.5 Typical spectra and PSFs in 700nm simulated with different values of $M_{a,1\text{-}3}$.

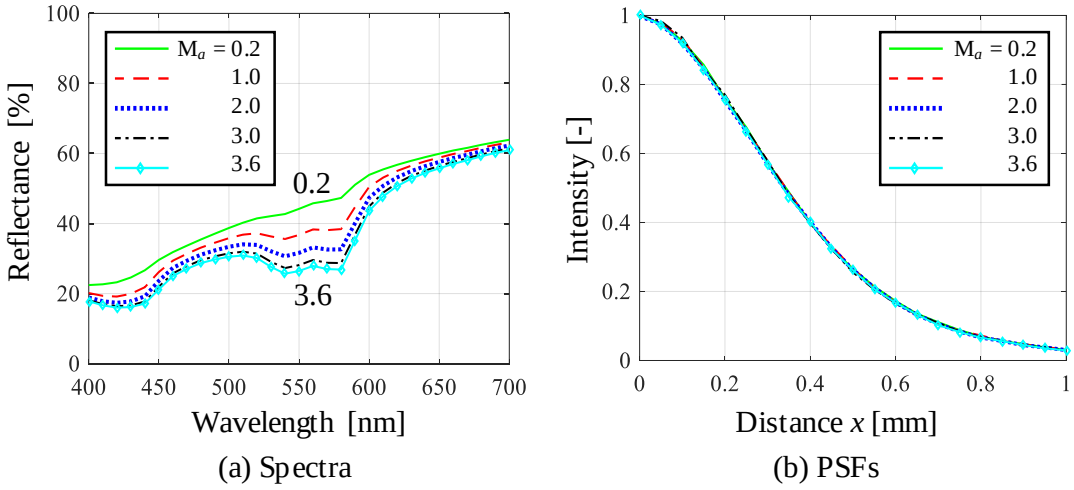

Fig. 4.6 Typical spectra and PSFs in 700nm simulated with different values of $M_{a,4\text{-}9}$.

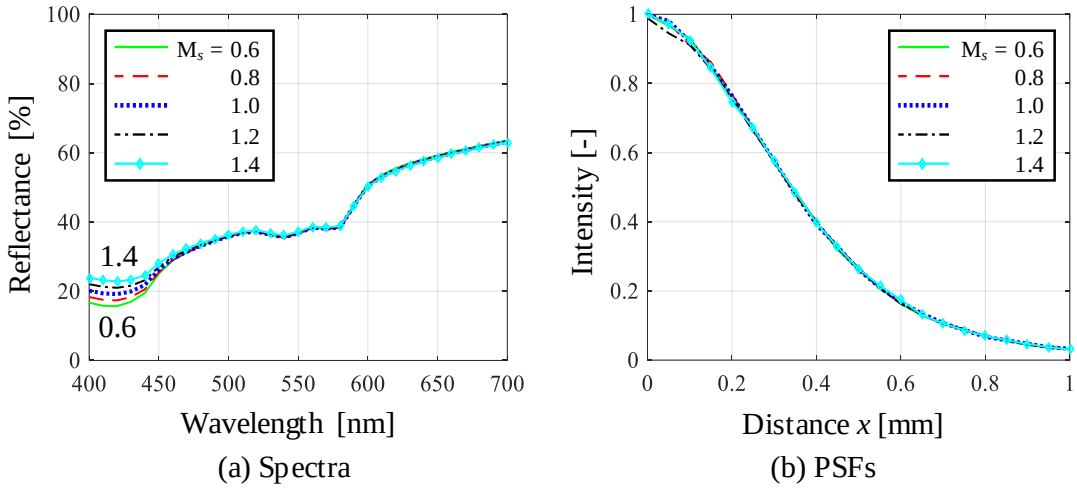

Fig. 4.7 Typical spectra and PSFs in 700nm simulated with different values of $M_{s,1\text{-}3}$.

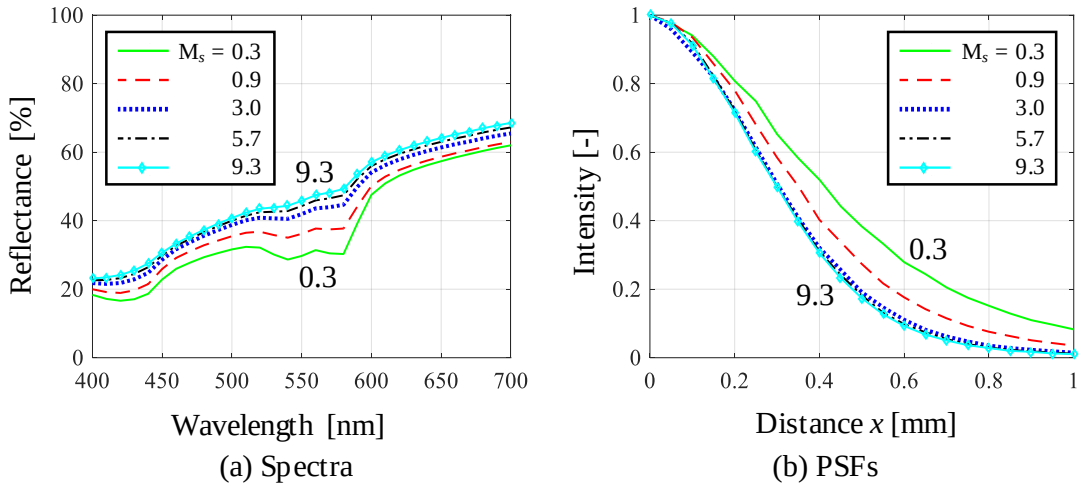

Fig. 4.8 Typical spectra and PSFs in 700nm simulated with different values of $M_{s,4\text{-}6}$.

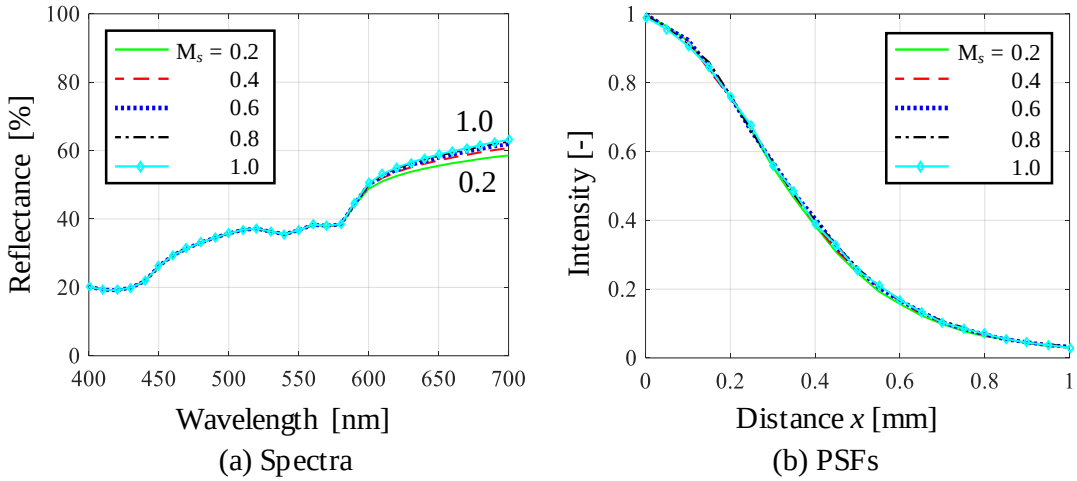

Fig. 4.9 Typical spectra and PSFs in 700nm simulated with different values of $M_{s,7\text{-}9}$.

Results of the simulated PSFs show no change with $M_{s,1\text{-}3}$ and $M_{s,7\text{-}9}$ in Figs. 4.7 and 4.9, respectively, but demonstrate remarkable change with $M_{s,4\text{-}6}$ in Fig. 4.8. Here, we found that PSF behavior shows different properties between Figs. 4.6 and 4.8. Change of μ_s by $M_{s,4\text{-}6}$ results in clearly different slopes in Fig. 4.8, but no change in the slope in Fig. 4.6. We interpret this difference by a step size, or mean free path of photon in the framework of the MCS. The step size s is given by

$$s = -\frac{\ln(\xi)}{\mu_a + \mu_s} \quad , \tag{4.3}$$

in the MCS of light propagation in the layered skin model [11], where ξ is a random number between 0 and 1. As seen from Table 4.1, μ_s is typically much larger than μ_a in the skin tissue. Thus, change of μ_a-value has negligibly small effect on the step size s, while change of μ_s-value has a substantial amount of influence on s. Increase of μ_s results in decrease of s, and this probably enhances multiple scattering near the illuminating point, which corresponds to the origin of distance x in the PSF graph. This can be considered as a source that the PSF curve becomes steep with increase of μ_s by $M_{s,4\text{-}6}$. In Fig. 4.8(b), the full width at half maximum, FWHM decreases from 0.95 to 0.69 with increase of $M_{s,4\text{-}6}$ from 0.3 to 9.3 in the wavelength of 700 nm.

Figure 12 shows the intensity distribution maps simulated in the MCS of photon fluence [11] by using the same condition as those in Fig. 4.6(b) and Fig. 4.8(b). In Fig. 4.10(I), the circular area of intensity distribution seems not to be affected by the change of values in $M_{a,4\text{-}9}$ or the absorption coefficient μ_a in dermis. In Fig. 4.10(II), it is found that the circular area with a certain level of intensity becomes small with increasing values of $M_{s,4\text{-}6}$ or the scattering coefficient μ_s, and indicates agreement with the PSF property in Fig. 4.8(b). From the present discussion, we consider that the database including PSF data as well as reflectance spectra are useful for identification of the target spectrum. Probably, the PSF curves at 700 nm is effective for improving the present ambiguity problem.

On actual measurements, it is necessary to obtain PSF data as well as the spectrum to use the present identification procedure. Usually, this can be made, for example, by hyper-spectral imaging with a point-like illumination. It should also be noticed that discrimination of the five types A to E of spectral changes can be made by comparing the spectral shape between before and after the change of skin condition and by finding the

wavelength band that shows the reflectance change. For the similar spectral changes in types B and D, PSF becomes effective to differentiate the similarity. Therefore, we should develop a certain intelligent procedure for identification of a measured spectrum and skin parameters in the framework of the constructed database in the near future. One possible example is considered briefly here. We first measure spectra from non-diseased and diseased areas of the same person, or occasionally before and after getting diseased. After that, we compare those spectra and assign the spectral change to Types A to E. If it matches with B and D, we need to compare PSFs from diseased and non-diseased sites. If a certain change is found in PSFs, it can be recognized as type D, and we may say that the skin condition changes in its scattering property and we adopt the extracted spectrum having a change of the magnification factor $M_{s,4\text{-}6}$ for the estimation of optical properties from the database. If no change is found in PSFs, it can be said as type B.

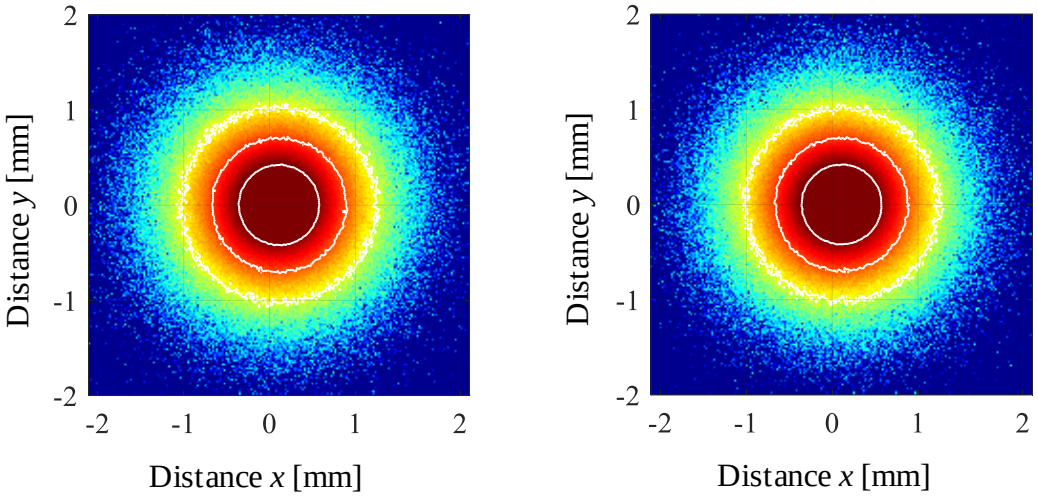

(a) $M_{a,4\text{-}9} = 0.2$ (b) $M_{a,4\text{-}9} = 1.0$

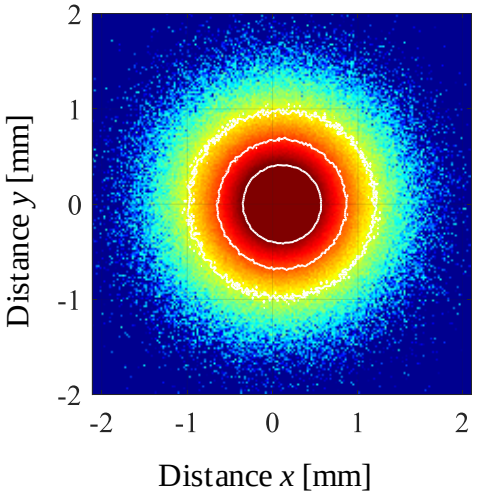

(c) $M_{a,4\text{-}9} = 3.6$

(I)

Fig. 4.10 Simulated intensity distribution on the surface of the skin model. (I) and (II) correspond to the two types B and D of spectral change by increasing values of $M_{a,4\text{-}9}$ and $M_{s,4\text{-}6}$, respectively.

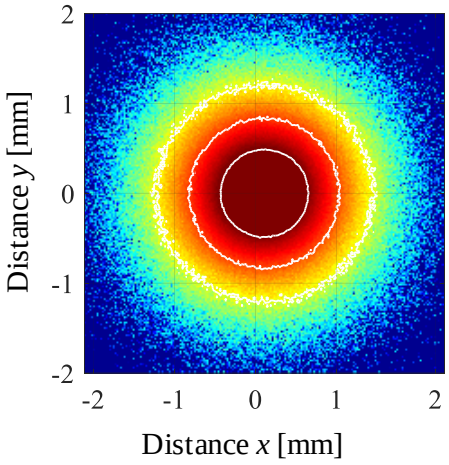

(a) $M_{s,4\text{-}6} = 0.3$

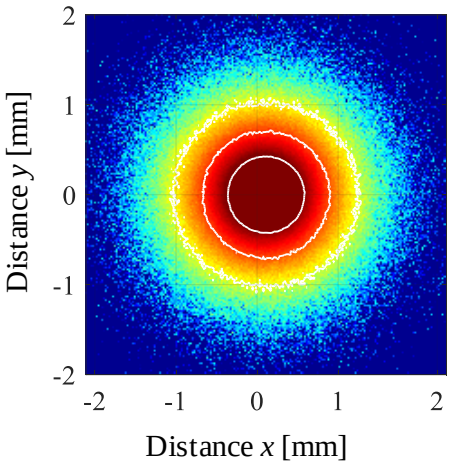

(b) $M_{s,4\text{-}6} = 0.9$

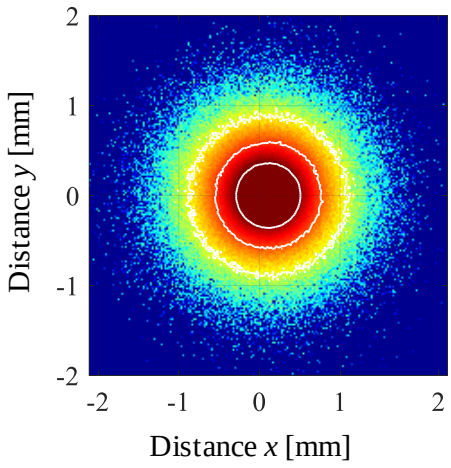

(c) $M_{s,4\text{-}6} = 9.3$

(II)

Fig. 4.10 Simulated intensity distribution on the surface of the skin model. (I) and (II) correspond to the two types B and D of spectral change by increasing values of $M_{a,4\text{-}9}$ and $M_{s,4\text{-}6}$, respectively.

To evaluate accuracy of the absorption and scattering coefficients, μ_a and μ_s obtained by the proposed method in the actual situations, it is desired to use any alternative method to estimate μ_a and μ_s in skin tissue and to compare the results. This is probably a possible approach to investigate the estimation accuracy. There are several evaluation methods, as we mentioned in Section 4.1, which can be used for this purpose. Also, the optical coherence tomography (OCT), and some advanced microscope techniques including confocal scanning laser microscopy [151] and polarization-resolved second-harmonic microscopy [152] are promising means to observe tissue structural changes which are closely related to the scattering coefficient. The comparison study with some of these possible techniques should be performed in the future to clarify the accuracy on the proposed estimating method.

4.5 Conclusion

We constructed a skin reflectance spectral database in the framework of the Monte Carlo simulation with the nine-layered skin tissue model. To realize the database in the reasonable size, we proposed the moderate grouping method for nine layers which enables us to change values of the absorption and scattering coefficient, μ_a and μ_s in the nine layers in the reduced numbers of combinations. To identify the desirable spectrum in the extraction from the database, we described also the use of PSF behaviors. Using the present identification procedure, we expect to extract the most desirable spectrum which is well close to the target spectrum, and to evaluate μ_a and μ_s values associated with the spectrum in the database in a real time manner. This approach provides us to obtain

information on μ_a and μ_s in the target skin tissue to be measured without multi-variate analysis and related mathematical modeling. However, the accuracy of skin parameters obtained through the database is not yet investigated in actual situations. This study described numerical approaches and, therefore, we intend to enhance the demonstrate the usefulness of this approach by *in vitro* and *in vivo* experimental studies in the near future.

Chapter 5

Spectral Classification and Mining in Simulated Reflectance Database for Detection of Absorption Change in Skin Tissue

5.1 Introduction

In the previous chapter [153], we proposed the use of a database consisting of various simulated spectra for estimating the absorption and scattering coefficients of a measured spectrum, in which a simulated spectrum that closely resembles with the measured spectrum is extracted out from the spectral database. The absorption and scattering coefficients associated with the extracted spectrum are regarded as estimated absorption and scattering coefficients of the measured spectrum. To construct the database, we also introduced the moderate grouping method [134] for changing values of absorption and scattering coefficients in the nine layers. By this method, we constructed the spectral reflectance database in the reasonable size while utilizing the merit of having nine layers in skin tissue model. We treated nine layers as two groups of the first to third and fourth to ninth layers for the absorption coefficient, and three groups of the first to third, fourth to sixth, and seventh to ninth layers for the scattering coefficient. Thus, we have five different groups, each of which demonstrates its specific spectral change type, due to the change of group-wise absorption or scattering coefficient. We demonstrated by simulation study a possibility that a type of difference between spectra before and after a

certain skin conditional change can be classified to one of the five groups and used for specifying a cause such as decrease or increase of absorption and/or scattering coefficients. We consider that this step can be helpful for mining efficiently a candidate spectrum from the database. There was, however, the problem of ambiguity or uncertainty in identification of a simulated spectrum being similar to the measured spectrum, since some different combinations of absorption and scattering coefficients produce similar reflectance spectra [135].

For example, decrease of absorption coefficient and increase of scattering coefficient in dermal layer cause similar spectral change. Thus, it is at present difficult to discriminate between them from spectral shape. However, if we pay attention to some application in which absorption coefficient changes are primarily of interest, we expect to detect the change of absorption by spectral shape recognition with less effect of scattering change. Then, we believe that this database method may be applied to analysis of chromophores such as melanin and hemoglobin, since they are known to be directly related to absorption coefficients of skin tissue layers. This application of the database is considered undoubtedly valuable, as many researchers have actually made much effort to estimation of melanin and hemoglobin concentrations using their respective techniques [72,56-59, 73-76], which provide useful information on various skin conditions including cancers, pigmentation, and tissue metabolism.

In this chapter, we propose a method of spectral classification and mining for analyzing change of chromophore concentration in the skin tissue using the spectral database. In order to confirm experimentally a feasibility of the spectral classification, which we demonstrated only by numerical simulation [153], we performed experiments using agarose-gel phantoms. We next performed pressure-cuff occlusion and hot water

immersion experiments for a human subject, to confirm ability of the proposed method for detecting change in hemoglobin concentration or absorption coefficients of dermal and subcutaneous layers. To discuss results obtained by the proposed method, we compared the tendency of estimated parameters with those by the MRA method. To counter the problem of ambiguity in extracting a similar simulated spectrum to the measured spectrum, we investigated a probable approach of using a customized database which consists of simulated spectra with variation in absorption (or scattering) coefficients while keeping fixed scattering (or absorption) coefficients. This approach is expected to be useful for detecting change in chromophore concentration with assuming that no considerable change takes place in scattering property. In case it is unknown whether skin condition changes in absorption or scattering, we consider that the spectral classification may become a useful step to judge of utilizing the customized database for spectral mining.

5.2 Database and Spectral Mining

5.2.1 Nine-Layered Skin Tissue Model and Monte Carlo Simulation

Human skin is known to have a complex structure as can be seen in Fig. 2.12(a) of chapter 2. Generally, a skin tissue model consists of three layers which are epidermis, dermis and subcutaneous layers. However, this model comes in short in mimicking various skin conditions aptly. One of such examples is that melanin in epidermis and hemoglobin in dermis have inhomogeneous distribution along the vertical direction in

skin tissue. We used a nine-layered model [122] which was developed on the basis of histological classification as shown in Fig. 2.12(b). Typical thickness value of each layer shown in Fig. 2.12 is obtained by modifying the data of Meglinski and Matcher [123], assuming the human forearm skin. These layers are modeled to be in parallel and have uniform scattering and absorption property within each of the nine layers. Absorption coefficients are characterized by concentration of chromophores such as melanin in epidermis and hemoglobin in dermis due to their absorption property. On the other hand, scattering coefficients are characterized by mainly the scattering property of fiber components such as collagen and elastin that exist in dermis and are responsible for elasticity of skin. Inclusion of blood vessels and capillary network are also contributed to the absorption and scattering. The overall effect of these blood vessels is treated in terms of absorption coefficients for hemoglobin contained in blood, and scattering coefficients for location and formation of vessels and networks. In this way, the nine-layered model is regarded to generate more realistic skin conditions than the conventional three-layered model.

We employed Monte Carlo simulation (MCS) for emulating light propagation in skin tissue statistically [10,136-140]. In MCS, we used the algorithm by Wang *et. al.* [30], which requires values of five input parameters to be specified at each wavelength for each layers. These parameters are scattering coefficient μ_s, absorption coefficient μ_a, anisotropy scattering parameter g, refractive index n, and thickness t. In addition, oxygen saturation Sat-O_2 is also needed to be given for specifying absorption coefficient μ_a in layers L_4 to L_9, as the μ_a of layers L_4 to L_9 (dermis and subcutaneous layers) mainly represents the absorption characteristics of hemoglobin. Anisotropy scattering parameter g is given by the average cosine of scattering phase function, and it ranges from -1 to +1

by representing backscattering to forward scattering. According to the algorithm by Wang *et. al.*, we utilized the characterization of *g* by Henyey-Greenstein function [110], as well-known approximated form of the phase function. It is generally known that typical values of *g* take 0.7-0.8 in skin tissue and greater than 0.9 in blood. Each of the selected *g* values are set by referring to the published data [153, 141-144]. The refractive index *n* has essentially wavelength dependency, yet is assumed to be constant in the visible wavelength range with reasonable simulation accuracy. In this study, we performed the simulation of diffuse reflectance in the wavelength range of 400-700nm at an interval of 10nm, and set the number of photon to be 10^6 for stable simulation. To prepare typical values for the five input parameters, we surveyed several articles [76,123,129,141-146] that contain feasible values at specific wavelength points and then modified them to have all the necessary values by interpolation and extrapolation. More detailed explanation for this skin model and MCS is given in the previous work [122].

5.2.2 Construction of Database by Moderate Grouping

To estimate skin parameters of a measured spectrum, we proposed a method of spectral database [153], in which a simulated spectrum that closely resembles with a certain measured spectrum is extracted by the criterion of root mean square error (RMSE). By the input parameters having been used for producing the extracted spectrum, we obtain estimated results as skin parameters of the measured spectrum. Here, we employ RMSE defined by,

$$\mathrm{RMSE} = \sqrt{\frac{1}{m}\sum_{i=1}^{m}\{R_s(\lambda_i) - R_t(\lambda_i)\}^2} \quad , \qquad (1)$$

where $R_s(\lambda_i)$ and $R_t(\lambda_i)$ are simulated and measured (target) spectra, λ_i denotes i^{th} discrete point of wavelength and m is the total number of wavelength points. Usually, we employ the condition of RMSE≤1~3%, according to the number of extracted spectra as candidates. To develop the database, we initiated a design of having a large number of spectral data by changing all the five parameters (μ_s, μ_a, g, n, and t) in each of nine layers. This approach may provide an enriched spectral database with a variety of simulated spectra but we noticed that it increased unnecessarily the size of database including unrealistic spectral data that correspond to unrealistic skin conditions. Then, we prudently observed the spectral reflectance library which includes typical spectral change behavior with varying of the five parameters in each of nine layers [149]. After that, we considered μ_a and μ_s probably as the primary factors for changing a spectral shape, although the other three parameters are related to some changes in spectra, but may not contribute in a significant amount to change the shape. So, we assumed that g, n, and t take constant values, while they are set differently in each of the nine layers and, then, we changed only values of μ_a and μ_s to generate various simulated spectra to construct the database. By this assumption, the number of parameters to be changed is reduced from 45 (5 parameters in 9 layers) to 18 (2 in 9).

To form the database in a reasonable size and simple way with still keeping the unique advantage of having nine layers, we further introduced the moderate grouping method [153]. To make those 18 parameters to be changed (μ_a and μ_s in 9 layers) easily, we introduced magnification factors M_a and M_s with respect to μ_a and μ_s, respectively in their group-wise changing. So the change of values for μ_a and μ_s are executed by varying M_a and M_s, in terms of $\mu_a \times M_a$ and $\mu_s \times M_s$, respectively. Since μ_a is known to be

characterized by melanin in epidermis and hemoglobin in dermis and subcutaneous layers, we set two groups of layers L_1-L_3 and L_4-L_9. Then, we changed the values of μ_a in the nine layers by magnification factors, termed as $M_{a,1\text{-}3}$ and $M_{a,4\text{-}9}$ for two groups. On the other hand, μ_s is supposed to be related with the morphological changes in tissue structure having refractive index differences, and are here made into three groups of layers, L_1-L_3, L_4-L_6 and L_7-L_9. We changed the values of μ_s in the nine layers by magnification factors termed as $M_{s,1\text{-}3}$, $M_{s,4\text{-}6}$ and $M_{s,7\text{-}9}$ for three groups. This group-based changing enables us to make the process for changing values of μ_a and μ_s in nine layers convenient and less time consuming. It should be noted that this group-based changing makes magnification in each group consistent, while keeping the context of μ_a and μ_s having different values in all the nine layers. The range of changing for these five groups is given in Table 5.1. For $M_{a,1\text{-}3}$ and $M_{s,1\text{-}3}$, we have enlarged their range from our previous version of database [153] to cover a wide range of spectral variation due to change of μ_a and μ_s in layers L_1 to L_3.

We optimized a value of discrete step for changing the magnification to be 0.2 for $M_{a,1\text{-}3}$ and $M_{a,4\text{-}9}$, 0.3 for $M_{s,1\text{-}3}$ and $M_{s,4\text{-}6}$, and 0.1 for $M_{s,7\text{-}9}$ from our experience made in the previous work [153]. Then, the number of discrete steps for changing is 18 for $M_{a,1\text{-}3}$ and $M_{a,4\text{-}9}$, 31 for $M_{s,1\text{-}3}$ and $M_{s,4\text{-}6}$, and 10 for $M_{s,7\text{-}9}$, and resultantly this database contains 3,113,640 spectral curves. It should be noted that variation in a layer thickness t was not considered in the construction of this database, although the thickness t may change in different individual and different parts of a body. So, the estimated μ_a and μ_s do not reflect the effects of changing t, as well as changing n and g. However, we consider that this approach is able to detect the relative change of μ_a and/or μ_s values due to some physiological change, for example that in normal to abnormal skin hemo-dynamics. As a

special mention, oxygen saturation Sat-O_2 is kept fixed at 80% in order to reduce the complexity in construction of database.

Table 5.1 Magnification values used for producing database. I_L is a discrete step where L indicates layers in a group.

Layers	M_a	M_s
1~3	0.2 ~ 3.6 ($I_{1\text{-}3}$= 0.20)	0.3 ~ 9.3 ($I_{1\text{-}3}$= 0.30)
4~6	0.2 ~ 3.6 ($I_{4\text{-}9}$= 0.20)	0.3 ~ 9.3 ($I_{4\text{-}6}$= 0.30)
7~9		0.1 ~ 1.0 ($I_{7\text{-}9}$= 0.10)

5.2.3 Spectral Classification and Mining

While using the database for detecting skin condition change, we confronted the ambiguity problem that different sets of μ_a and μ_s values produce similar spectra [135] to each other in the database. We recognize this as an annoying situation for extracting properly the desirable simulated spectrum from the database. To assess this situation, we investigated changing behavior of simulated spectra in the five different types [153] corresponding to the above-mentioned five groups and magnification factors, as shown in Fig. 5.1. Figures 5.1(a) and (b) show typical spectra with changing values of $M_{a,1\text{-}3}$ and

$M_{a,4\text{-}9}$. In Fig. 5.1(a), change of reflectance (around 40%) is found in the whole wavelength range due to the effect of melanin, and assigned as “Type-A”. In Fig. 5.1(b), it can be seen that the change of reflectance (of 20%) occurs mainly in a range of 500-600nm which is due to the effect of hemoglobin [147]. This type of change is assigned to “Type-B”. Figures 5.1(c), (d) and (e) show typical spectra with different values of $M_{s,1\text{-}3}$, $M_{s,4\text{-}6}$ and $M_{s,7\text{-}9}$, and are respectively assigned as “Type-C”, “Type-D” and “Type-E”. In Fig. 5.1(c), a significant change in reflectance (of 20 to 40%) can be seen mainly in a region of 400-600nm. Figure 5.1(d) depicts reflectance change (around 20%) particularly in the middle wavelength range of 500-600nm, and spectra in Fig. 5.1(e) shows slight change (by 5%) in the longer wavelength range. It should be noted that Type-B and Type-D show similar nature of changing reflectance in the range of 500-600nm with respect to increasing $M_{a,4\text{-}9}$ and decreasing $M_{s,4\text{-}6}$, respectively. We consider this behavior to be a possible source of producing the similar spectra in the constructed database.

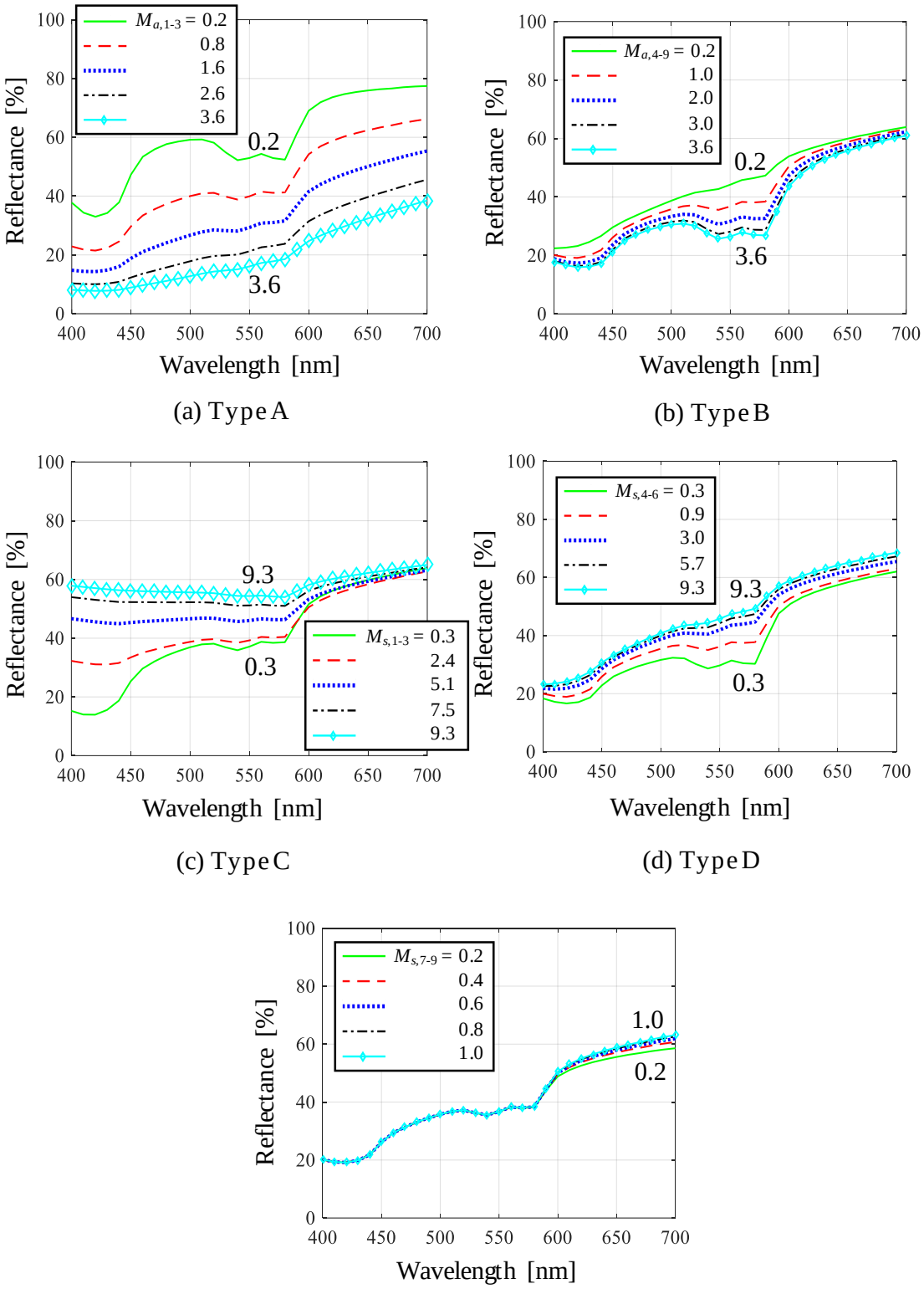

Fig. 5.1 Five types of change in shape of simulated spectra included in the constructed full-size database.

In chapter 4, we showed possibility of using a point spread function (PSF) of reflected intensity on the skin surface. However, accurate measurement of PSF is a difficult task generally due to some limitation in camera device, optical components and system. So, we did not proceed with the idea of using PSF to identify the similar spectra. Thus, the presence of ambiguity in the constructed database remains to be solved in our study. Currently, we are considering some possible approaches for specific applications. One of them is to compare very carefully spectral shapes of Type-B and Type-D. In case of Type-B by change of $M_{a,4\text{-}9}$, we observe very small change (less than 3%) in reflectance in the longer wavelength range (650-700nm), but for "Type-D" by change of $M_{s,4\text{-}6}$ there are some visible difference (more than 7%) in that range. This observation has its own drawback, as it depends on a conventional comparison of spectral shape between "Type-B" and "Type-D", which is time consuming and unstable and often requires experience. Another possible approach is using an application-based customized database. Here we focus our attention to a μ_a-type customized database that consists of spectra obtained by changing μ_a or M_a while μ_s or M_s is fixed in the nine layers. This can be applied to a situation where a change in chromophore concentration takes place. In this case, the actual influence by absorption change is expected to be seen without significant interference by scattering change. In Sections 4 and 5, the applicability of μ_a-customized database is presented and discussed by comparison with the original database in a full size. So, in this study we refer to the original database, which is constructed by simulated spectra with varying both μ_a and μ_s values, as a full size database in contrast to the customized database.

In case of general application without knowledge on change in absorption or scattering, we consider the following two-step approach. The five types of spectral change as shown in Fig. 5.1 is first referenced for all measured reflectance spectra, two of which

have some difference in the shape before and after a certain change of skin condition. Then, we compare spectral shape of the two. Due to the distinct changes in a specific wavelength range of types A, C and E, these types may easily be identified. But, in case of similar spectral changes in types B and D, it is required to mention a probable cause of changing skin conditions (absorption or scattering) to avoid erroneous judgement on type of spectral change. For this, we need to perform very careful observation of spectral change, especially in the longer wavelength range of 650-700nm. After this spectral classification in the five types, then we can employ a customized database, instead of using a full size database. This two-step approach of spectral classification and mining is expected to be advantageous for improving the reliability of spectral mining from the database for detection of absorption (or scattering in the future) change in skin tissue.

5.3 Phantom Experiments

5.3.1 Agarose-gel Phantom

To confirm the existence of five types of spectral change being used for spectral classification, we performed experiments on agarose-gel type skin phantom [74,154]. We fabricated a three-layered phantom model, where layers PL_1, PL_2 and PL_3 correspond to epidermis, dermis and subcutaneous fat tissue, respectively. Each of the three layers has specific thickness: 0.6mm for PL_1, 6.8mm for PL_2 and 4.5mm for PL_3. All of these specific thickness values have been determined by investigating many different models where different sets of thickness were used and finally the above-mentioned set was accepted so that we could have spectral reflectance curve rather similar to a measured

reflectance spectrum of human skin. In layer PL_1, coffee solution is used as an absorber or a melanosome substitute. For layers PL_2 and PL_3, horse blood (Nihon Biotest Kenkyujo, Saitama, Japan) with hematocrit of 44% was used as an absorber. We used 20%-Intralipos solution (Otsuka Pharmaceutical Co. Ltd, Tokyo, Japan) with different volume concentration (V. C.) to include the scattering phenomenon in all the three layers separately. As the base material, agar solution was prepared by mixing agar powder (Ina Shokuhin Kogyo, Nagano, Japan) in saline with a weight ratio of 0.8%. We did not use any deoxygenating agent (for example- $Na_2S_2O_4$) [74] in layers PL_2 and PL_3, so we assumed the oxygenation level of these layers to be 100%. Table 5.2 shows the volume concentration of coffee, blood and Intralipos of a certain phantom, which we referred as a phantom in the standard condition in this study.

Table 5.2 Amount of coffee, blood, Intralipos and agarose-gel solution used for a phantom at the standard condition.

Layer	Coffee [ml] (V. C.)	Blood (44% of HCT) [ml] (V. C.)	Intralipos 20% sol. [ml] (V. C.)	Agarose-gel solution [ml] (V. C.)	Thickness [mm]
Epidermis (PL_1)	1.8 (9%)	0.0	3.0 (15%)	15.2 (76%)	0.6
Dermis (PL_2)	0.0	0.4 (0.8%)	10.0 (20%)	39.6 (79%)	6.8
Subcutaneous (PL_3)	0.0	0.4 (1%)	4.0 (10%)	35.6 (89%)	4.5

To measure a reflectance spectrum, we used the experimental system shown in Fig. 5.2 [122]. Light from a halogen lamp (Hayashi, LA-150UX), which covers a visible wavelength range, was focused through a light guide and lens in such a manner that it produces a spot of 4 mm on a surface of a measured sample. Diameter and focal length of lens were 54 and 100 mm, respectively. The diffuse light reflected from the sample, which was placed at a sample port of an integrating sphere (Labsphere, RT-060-SF), was collected by a fiber probe having a diameter of 400 μm at the detector port. A light trap was attached to the integrating sphere to suppress specular reflectance component, so that only the diffused reflected light is detected. The detecting region at the sample port was circular in diameter of 22 mm. A multichannel spectrophotometer (Ocean optics, SD-2000) was employed to measure a reflectance spectrum of the light transmitted from the detector port in a visible wavelength range of 400-700nm with an interval of 10nm. Figure 5.3 shows a typical reflectance spectrum measured on a phantom in the standard condition. The result seems resemble a typical spectrum of human skin and demonstrates low spectral reflectance in the shorter wavelength range and high in the longer one, with having ‘W’-like characteristic coming from the oxygenated hemoglobin in the middle wavelength [147].

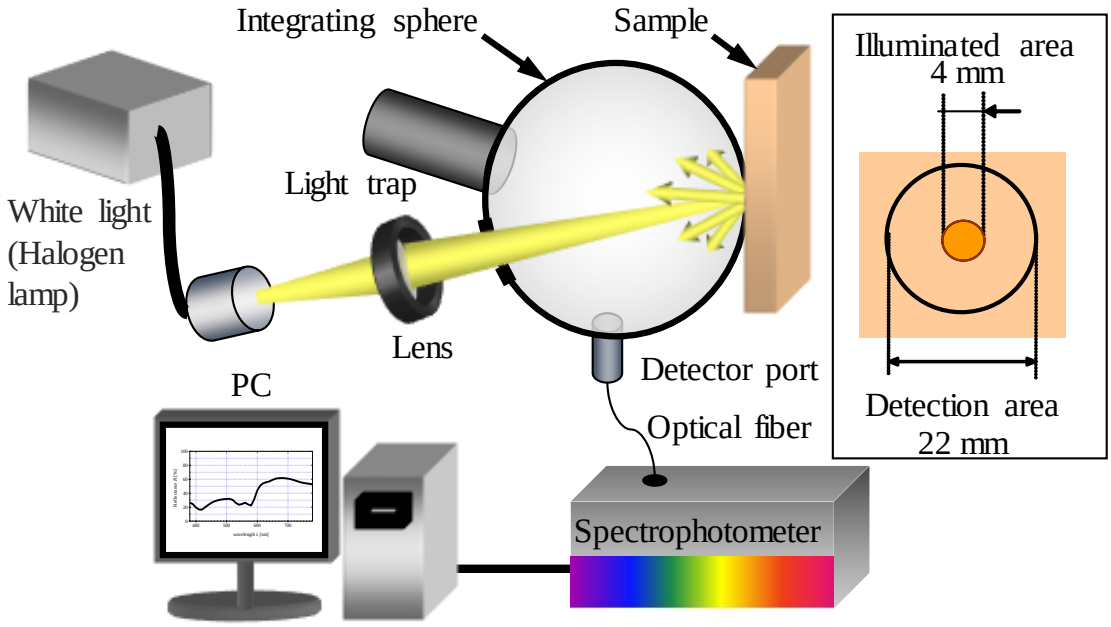

Fig. 5.2 Schematic diagram of spectral reflectance measuring system.

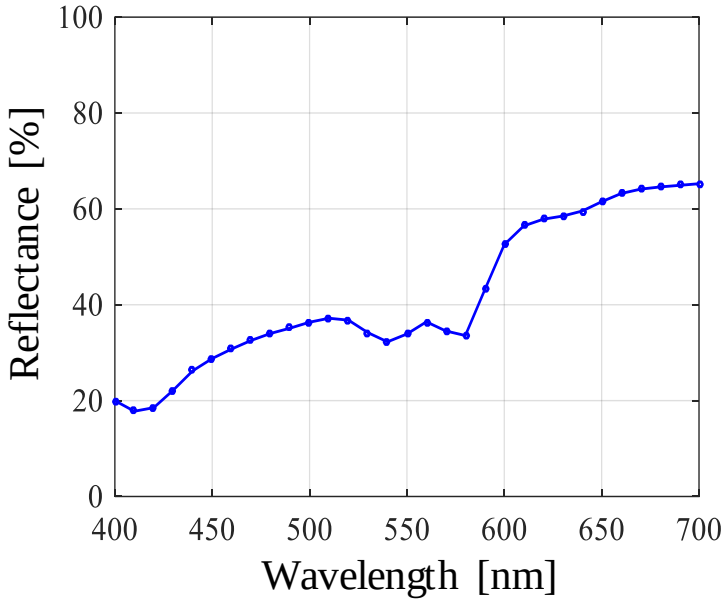

Fig. 5.3 Typical reflectance spectrum measured on a phantom at the standard condition.

5.3.2 Five Types of Spectral Change in Phantoms

As is shown in Fig. 5.1, there are five types of change in spectra simulated by using the five magnification factors in the constructed database. Here, we tried to find out five types of change in spectra measured on phantoms by varying the amount of absorber and scatterer. It should be noted that simulated spectra in the database are based on the nine-layered skin model. But, in the case of phantom experiment, we chose to fabricate a three-layered model due to its easy fabrication and repeatability, and with reasonable similarity to human skin in a reflectance spectrum. Figure 5.4 demonstrates five typical spectral changes of reflectance corresponding to specific changes in volume

concentration of coffee, blood and Intralipos in different layers of the phantom. Figure 5.4(a) represents a typical change of spectral reflectance due to the change of volume concentration of coffee in layer PL_1 and termed as "Type-A", following the corresponding notation of Fig. 5.1. With increasing the amount of coffee, the spectral reflectance is decreased (nearly 10%) in 430-530nm and 600-700nm regions, but almost no change in 530-600nm region was found. This is probably due to strong absorption of light by blood component in layer PL_2. Figure 5.4(b) shows a typical change of spectral reflectance produced by different volume concentration of blood in layers PL_2 and PL_3, and termed as "Type-B". Increasing of blood results in some decrease (around 10%) in reflectance in 400-500nm, and a substantial decrease (of 20%) in 500-600nm, and almost no change in 600-700nm. Figures 5.4(c), (d) and (e) show typical change in reflectance spectra with different amount of Intralipos individually in layers PL_1, PL_2 and PL_3, and termed as "Type-C", "Type-D" and "Type-E", respectively. In Fig. 5.4(c), increase of Intralipos in layer PL_1 resulted in increase of reflectance throughout the spectrum, especially with large increase (by 30 to 35%) in 400-580nm. In Fig. 5.4(d), increasing Intralipos generated increase in reflectance throughout the spectrum, particularly (by 15 to 20%) in a region of 500-700nm. For the result in Fig. 5.4(e), almost no significant change was found in spectral shape with increase of Intralipos. It is probably due to the effect of substantial absorption and scattering in layers PL_1 and PL_2. In this case, we consider that the travelling light does not reserve intensity large enough to penetrate deep into layer PL_3 and then come back to the surface.

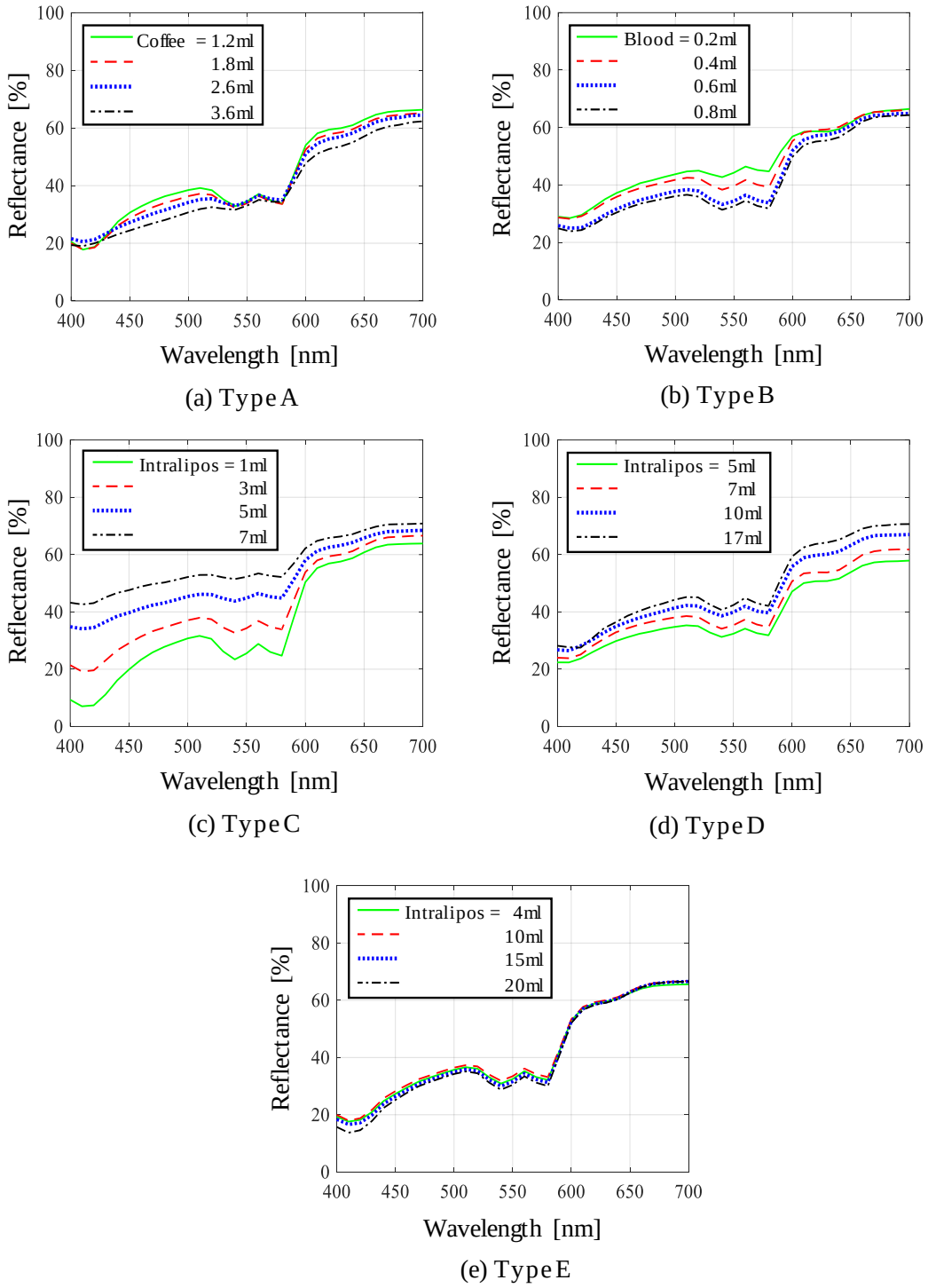

Fig. 5.4 Five types of change in shape of spectra measured from phantoms.

We compared these behaviors in the five types of spectral change in Fig. 5.4 with those found in simulation of Fig. 5.1. For “Type-B” to “Type-E”, we can see relatively similar change of pattern to each other between phantom and simulation. For “Type-A”, there is obvious difference between the simulation and phantom. This was probably due to mismatching in a changing range of absorption and scattering amounts between phantom and simulation. To investigate this, we further simulated some spectra as samples by changing μ_a in a small range with a single-layer magnification factor $M_{a,3}$ only for layer L_3 of the nine-layered model, instead of group-based change of μ_a in L_1-L_3 by magnification factor $M_{a,1\text{-}3}$. The resultant spectra are shown in Fig. 6 and demonstrate better similarity with that of “Type-A” for the phantom in Fig. 5.4(a), although some difference still remains in 500-600nm. This investigation may additionally support that careful observation of spectral change enables us to perform spectral classification into the five types, since the spectral changing type of Fig. 5.5 is probably discriminated from the other types of “Type-B” to “Type-E” in Fig. 5.1.

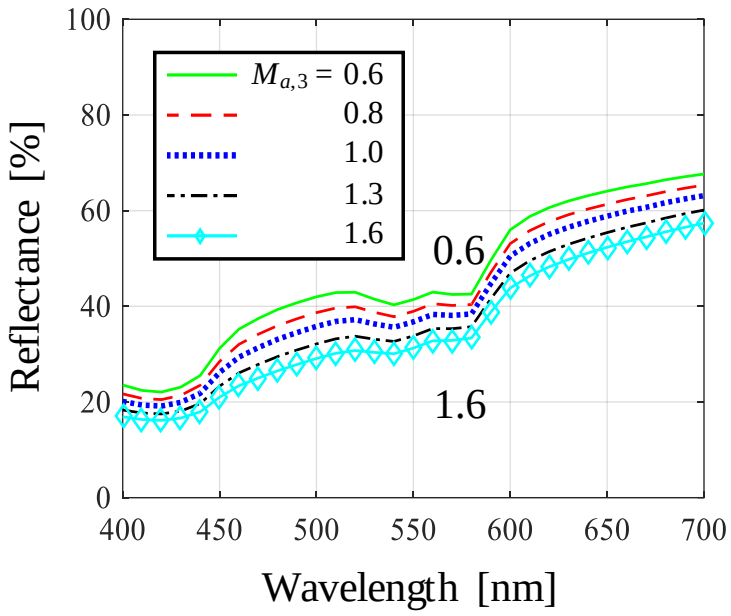

Fig. 5.5 Simulated spectra with changing $M_{a,3}$ for layer L_3 of nine-layered skin model.

5.3.3 Blind Tests for Phantom

To validate possibility of classifying the types of change in spectral reflectance, we performed a blind test for phantom samples in each of four types A, B, C and D, but except for type E. We refer to a phantom in the standard condition given in Table 5.2 as the standard phantom, whose reflectance spectrum is shown in Fig. 5.3. Here, we changed concentrations of coffee, blood and Intralipos in four different cases. In the first case, we changed only the concentration of coffee in layer PL_1, which is referred to as a blind sample 1. Next, we changed that of blood in layers PL_2 and PL_3 together, referred to as a blind sample 2. Finally, we changed that of Intraliops in layer PL_1 and layer PL_2 separately, and referred to as blind samples 3 and 4, respectively. So, all these samples resulted in 4 different spectral reflectance curves, which were compared against the spectral

reflectance curve of the standard phantom to evaluate the types (A to D) of spectral change. Figure 5.6(a) shows the comparison of spectra between the blind sample 1 and standard phantom. The reflectance shows increase (of 5%) in 430-530nm and 600-700nm regions, but no change in 530-600nm, and this resembles "Type-A" of Fig. 5.4(a). So, this means there must have been a decrease in volume concentration of coffee in layer PL_1. This can be confirmed by the fact that we only decreased the volume concentration of coffee in layer PL_1 from the standard value of 9% (1.8ml) to 3% (0.6ml). Figures 5.6(b) and 5.6(c) represent the comparison of spectrum from the standard phantom with that of blind samples 2 and 3, respectively. These two results demonstrate some similarity in a change of spectrum. Detailed observation may indicate that a notably significant change is found in 500-600nm (around 15 to 18%) for Fig. 5.6(b), and in 400-580nm (around 20 to 25%) for Fig. 5.6(c), which most likely resembles "Type-B" and "Type-C" in Fig. 5.6, respectively. This observation agrees with the fact that we only decreased the volume concentration of blood in layers PL_2 and PL_3 from the standard value of 0.8% (0.4ml) to 0.2% (0.1ml) to fabricate blind sample 2, and increased the volume concentration of Intralipos in layer PL_1 from the standard value of 15% (3ml) to 40% (8ml) to fabricate blind sample 3. Figure 5.6(d) shows large decrease in reflectance (by 15 to 18%) in the longer wavelength (600-700nm) and small decrease (of 5%) in 450-600nm. These characteristic traits are closely related to "Type-D", which corresponds to behavior due to decreasing amount of Intralipos in layer PL_2. This prediction can be confirmed by the fabricating condition in which the volume concentration of Intralipos in layer PL_2 was reduced from 20% (10ml) to 6% (3ml). For "Type-E" in a spectral shape of phantoms, we did not perform any blind test. As we mentioned earlier, "Type-E" refers to the situation of change in scattering property of layer PL_3, and this effect seems very difficult

to be observed due to the presence of absorption and scattering in layer PL_2. From the present blind tests, we confirmed the presence of five types of change in spectra and the possibility of the spectral classification into those types in the framework of phantom spectral behavior, although the spectral behavior of phantoms does not sufficiently coincide with that of real human skin.

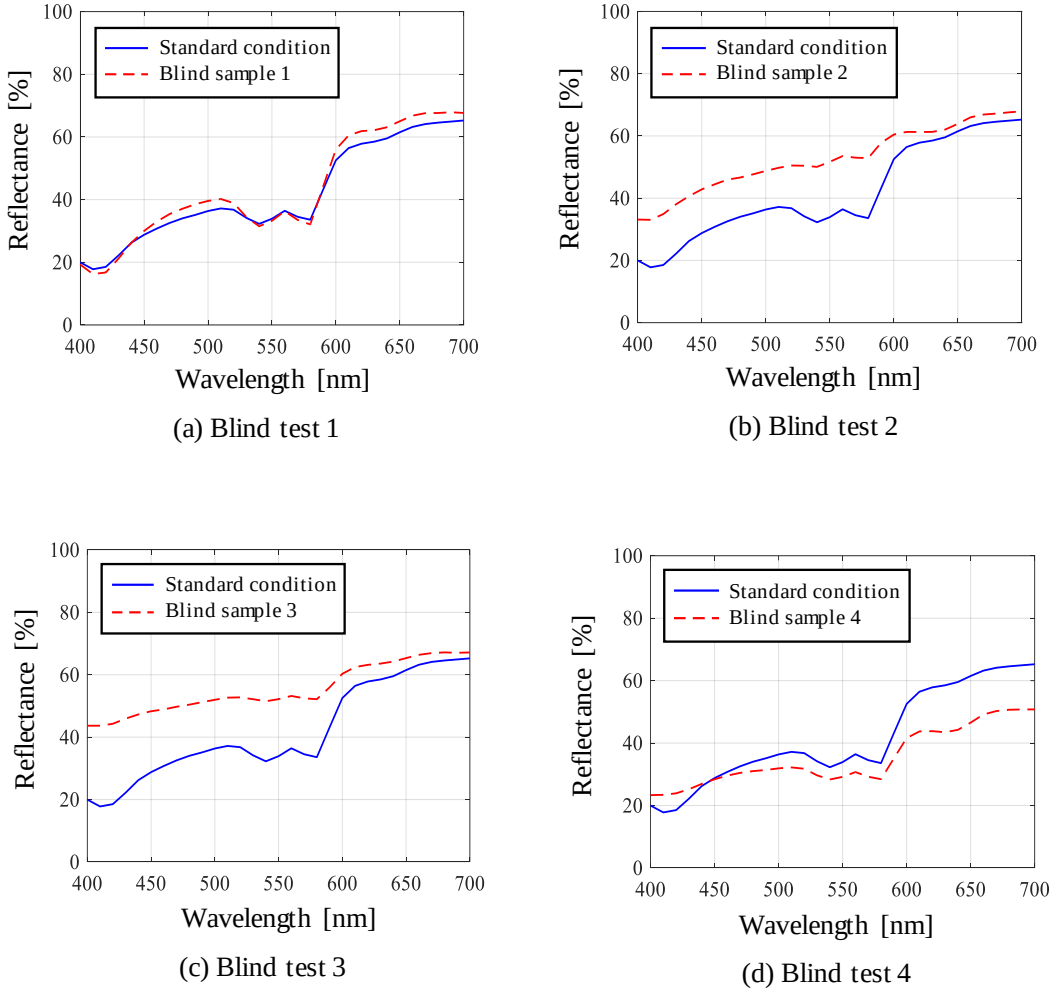

Fig. 5.6 Typical examples of spectral change obtained in the blind test.

5.4 Pressure-Cuff Occlusion Experiment

To investigate applicability of spectral mining for detection of absorption change, we performed pressure-cuff occlusion experiment, in which we expected to see change of absorption coefficient μ_a in dermal and subcutaneous layers in a time-sequential manner. A brachial cuff of a pressure type (aneroid) sphygmomanometer (Kenzmedico Co. Ltd., Saitama, Japan) was fixed around an upper arm of a Japanese adult male and pressure up to 180mmHg was applied. We administered time-series measurement of diffuse reflectance spectra from the surface of inner side of a forearm using the experimental setup shown in Fig. 5.2. The experimental protocol in Sects. 5.4 and 5.5 (described later) were approved by the Human Research Ethics Committee of Muroran Institute of Technology (Approval number H30-05-S05). The protocol for cuff occlusion experiment consists of pre-occlusion for 60 seconds, cuff occlusion for 100 seconds at the maximum pressure of 180mmHg and post-occlusion for 140 seconds in recovery to the normal state. Each spectrum was obtained by averaging 15 runs with one run made in 160ms. As the duration of the measurement was confined to 300 seconds, 125 reflectance spectra were measured at the rate of one spectrum in around 2.4 seconds.

Figure 5.7(a) shows typical reflectance spectra selected over the time course of 300 seconds, in which a clear change by 3 to 6% can be seen in the wavelength region larger than 500nm. To ensure increase or decrease of blood content with oxygenation level and no change of melanin content that we expected by cuff occlusion, we performed the MRA [74,75] for measured 125 spectra, by following the method by Nishidate *et. al.* [74]. According to modified Lambert-Beer law [60-62], an absorbance spectrum $A(\lambda)$ can be expressed as,

$$A(\lambda) = C_m l_e(\lambda)\varepsilon_m(\lambda) + C_{oh} l_d(\lambda)\varepsilon_{oh}(\lambda) + C_{dh} l_d(\lambda)\varepsilon_{dh}(\lambda) + S(\lambda) \ , \qquad (2)$$

where C and $\varepsilon(\lambda)$ are the molar concentration and molar extinction coefficient, and $l_e(\lambda)$ and $l_d(\lambda)$ are the mean path length in epidermis and dermis, and $S(\lambda)$ indicates attenuation by the other absorption and scattering of light. Subscripts m, oh and dh denote melanin, oxygenated hemoglobin and deoxygenated hemoglobin, respectively. By using $A(\lambda)$ as a response variable and $\varepsilon(\lambda)$ as predictor variables, MRA can be performed as

$$A(\lambda) = a_m \varepsilon_m(\lambda) + a_{oh} \varepsilon_{oh}(\lambda) + a_{dh} \varepsilon_{dh}(\lambda) + a_0 \ , \qquad (3)$$

where a_m, a_{oh}, a_{dh} and a_0 are regression coefficients, and express the degree of contribution of each molar extinction coefficient to $A(\lambda)$, being closely related to C_m, C_{oh} and C_{dh}, respectively. As a_m includes a factor of $l_e(\lambda)$, and a_{oh} and a_{dh} include a factor of $l_d(\lambda)$, the coefficients a_m, a_{oh} and a_{dh} have nonlinear relationship with C_m, C_{oh} and C_{dh}, respectively. To compensate this nonlinearity, Nishidate *et. al.* presented the use of conversion vectors that relate the regression coefficients a_m and a_{th} ($=a_{oh} + a_{dh}$) to C_m and C_{th} ($=C_{oh} + C_{dh}$). The estimated level of oxygen saturation Sat-O_2 (%) is obtained by

$$\mathrm{Sat} - \mathrm{O}_2 = \frac{a_{oh}}{a_{th}} \times 100 \ . \qquad (4)$$

As c_{th} represents concentration of total hemoglobin, it can be regarded as C_b or volume concentration of blood. Also, C_m can be regarded as C_{mel} or volume concentration of melanosome. Figure 5.7(b) depicts that C_b gradually increased by 27% and Sat-O_2 apparently decreased by 37% under the occlusion, while almost no change in C_m

(fluctuation of 3 to 5%) in all the three stages of pre-occlusion, occlusion and post-occlusion recovery. As soon as the occlusion was released, both C_b and Sat-O_2 increased sharply by 12% and 55%, respectively, in the moment and, then, slowly returned to the initial values by respective decrease of 38% and 19%. This sharp increase in C_b and Sat-O_2 is possibly due to the well-known effect of hyperemia, oxygenation and blood circulation recovery [167].

Next, we referred to the types of spectral change in Fig. 5.1 to identify a type of the spectral change in Fig. 5.7(a). From visual observation of spectral shapes, a probable type is considered to be types B or D or E. Since "Type-E" represents changing of scattering in deeper layers of skin tissue, it is at present difficult to relate reliably such a change to spectral shape as noticed in the previous numerical investigation [153]. Thus, we focus our discussion to "Type-B" or "Type-D". At present, we have no appropriate way to discriminate between these two types. Then, we performed spectral mining with the constructed full-size database and extracted 125 simulated spectra for all of 125 measured spectra using criterion of the minimum RMSE. Magnification factors associated with 125 extracted spectra are shown in Fig. 5.7(c), in which $M_{a,4\text{-}9}$ shows first no change in pre-occlusion stage. After the occlusion starts, this factor increases by 39% and reaches its maximum value and, then, saturates till the occlusion is withdrawn. After the occlusion is over, $M_{a,4\text{-}9}$ decreases by 38.8% and returns to the initial value. No change was found in the other three factors $M_{a,1\text{-}3}$, $M_{s,1\text{-}3}$ and $M_{s,4\text{-}6}$. No temporal response in these factors may assert that the spectral changes in Fig. 5.7(a) was mainly due to variation of μ_a or hemoglobin concentration in the dermal and subcutaneous layers and corresponding to "Type-B".

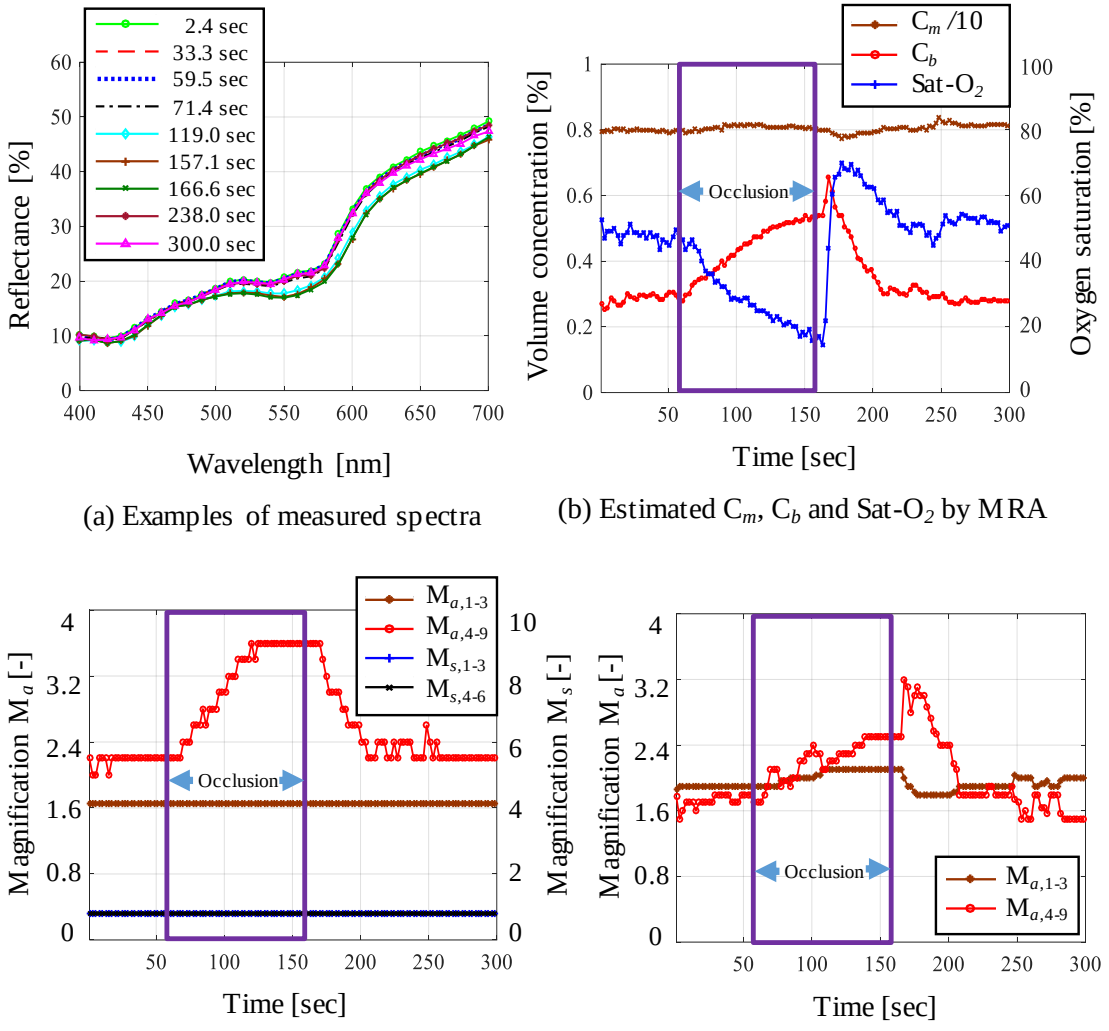

(a) Examples of measured spectra

(b) Estimated C_m, C_b and Sat-O_2 by MRA

(c) Magnifications by full-size database

(d) Magnifications by customized database

Fig. 5.7 Results obtained by using MRA and spectral mining in the pressure-cuff experiment.

According to this experimental condition of cuff-occlusion also, we can assume that the change of reflectance spectra in Fig. 5.7(a) is probably caused by variation of hemoglobin concentration due to suppression of blood circulation. This assumption leads to a prediction that the spectral change in Fig. 5.7(a) probably falls under the category of "Type-B" in Fig. 5.1(b). On the basis of this prediction, we conceived use of an alternative database which aimed at searching for change of μ_a only. We constructed this customized type of database by simulating spectra with different values of μ_a (with fixed Sat-O_2 of 80%) by changing $M_{a,1\text{-}3}$ and $M_{a,4\text{-}9}$ in the range of 0.2-3.6 with 35 discrete steps by interval of 0.1, under constraint of μ_s value fixed at the standard condition. This resulted in 1225 simulated spectra with change in μ_a only, and was expected to have better estimation specifically for change of absorption property corresponding to change of chromophore concentration. Figure 5.7(d) shows time course of magnification factors extracted by using the customized database, which represents better similarity of behavior between $M_{a,4\text{-}9}$ and C_b in Fig. 5.7(b). It is also interesting that $M_{a,4\text{-}9}$ in Fig. 5.7(d) successfully depicts a peak just after the release of occlusion. To express the change of $M_{a,4\text{-}9}$ in a quantitative manner, it first increased by 28% from its initial values under the occlusion, then further increased by 19% just after the release of occlusion, and finally returned to the pre-occlusion values with a decrease of 47%. Small fluctuation (3 to 6%) in $M_{a,1\text{-}3}$ in Fig. 5.7(d) is probably due to the improved resolution which became more sensitive to fluctuation in the measured spectra. We consider that this nature originates from micro-movement and positioning errors of the measuring area on a forearm.

By comparing the results in Figs. 5.7(b) and (c) or (d), we can confirm the resemblance in the changes of blood concentration C_b and magnification factor $M_{a,4\text{-}9}$ (with respective correlation coefficients of 0.962 and 0.905 for $M_{a,4\text{-}9}$ of the original and

customized database). Thus, the spectral mining from the database works well for detection of change in absorption property. However, the database method is currently not able to show the change of Sat-O_2, since all spectra included in the database were simulated with the fixed Sat-O_2 level of 80%. In the near future, we intend to add data of changing Sat-O_2 to the construction of database.

5.5 Hot Water Immersion Experiment

To assess further ability of the spectral mining for detecting change of absorption condition, we performed an experiment on hot water immersion for a human forearm, where we expected to observe change mainly in absorption coefficient of dermal and subcutaneous layers. This type of experiment is reported by some researchers to estimate the change of hemoglobin concentration [57,58,128]. Again we employed the experimental setup shown in Fig. 5.2. We first measured the reflectance spectrum on the inner side of forearm of a Japanese adult male in a normal health state at t= 0 min. Then, we immersed his forearm inside a water tank having the average temperature about 45°C for seven minutes. In two minutes, we performed reflectance measurement twice at t= 9 and 11 min. with an interval of two minutes. After that, we repeated measurement of reflectance spectra eleven times at t= 16 to 66 min. with an interval of five minutes. Finally, we obtained a total of 14 reflectance spectra in the time course of 66 minutes, which are shown in Fig. 5.8(a). It is observed from Fig. 5.8(a) that reflectance is clearly reduced around 10% in 500-600nm wavelength region under the influence of hot water immersion. This property suggests increase of hemoglobin concentration or absorption coefficient in dermal and subcutaneous layers. The reduction of reflectance is recovered

as time passes on.

To understand this spectral transition, first we analyzed L^* and a^* values of these 14 measured spectra as visual evidence of change in skin conditions through the experimental process. L^* has a changing range from black to white representing decrease or increase in brightness, and a^* has a changing range from green to red. As we can see from Fig. 5.8(b), after immersion L^* value is decreased by 42% with referring to reduced brightness and a^* value is increased by 40% with referring to redness of skin due to increased blood concentration. Then, both L^* and a^* values gradually increased by 34% and decreased by 35%, respectively to their initial levels. Figure 5.8(c) shows calculated color difference ΔE and RMSE (%) of measured spectra with respect to the first spectrum at t= 0. These results indicate a change of skin color and spectral shape after the immersion in terms of explicit increase of 97% and 48%, respectively, in the early time and gradual decrease of 95% and 40%, respectively, in the latter. Figures 5.8(d), (e) and (f) which represent the photographs of the measuring forearm before and after the immersion, further confirms the visual evidence. In Fig. 5.8(d), t= 0min represents before immersion where both the measuring and non-measuring forearms shows similar color. In Fig. 5.8(e), t= 11min represents four minutes after the immersion where increased redness of the measuring forearm can be seen. In Fig. 5.8(f), t= 66min represents the photograph of measuring forearm at the time of last measurement where no trace of the increased redness can be found.

Figure 5.8(g) shows results of the MRA analysis (mentioned in Section 4) for 14 measured reflectance spectra. Both Sat-O_2 and C_b increased sharply by 26% and 48%, respectively, in the first eleven minutes and then decreased gradually by 38% and 44%, respectively, but C_{mel} remains almost unaltered. This result indicates expectable behavior

in the concentrations of hemoglobin and melanin as can be seen in the preceding articles [57,58,128]. It should be noted, however, that the MRA does not generally provide us the effects of scattering properties distinctively, and thus, it tends to exhibit primarily the absorption characteristics of melanin and hemoglobin.

We next extracted magnification factors for all the measured spectra using spectral mining from the full-size database, as can be seen in Fig. 5.8(h). The result shows that $M_{a,4\text{-}9}$ is increased rapidly by 61% just after the hot water immersion in the first eleven minutes and then returned nearly to its original value with a decrease of 45% over passing time (having a correlation coefficient of 0.804 with C_b). However, for the spectra measured at t= 31, 36 and 41 min., the extracted $M_{a,4\text{-}9}$ shows unexpected local increase (about 10 to 15%) in Fig. 5.8(h). This is probably due to the ambiguity defect [153] in spectral mining, which exists between the changing types B and D in spectral shape as shown in Fig. 1. This consideration may be supported to some extent by noting that scattering magnification $M_{s,4\text{-}6}$ shows some decrease (by 13%) and then increase (by 22%) during the experiment in Fig. 5.8(h). This is unexpected behavior since the experiment was performed under the assumption of major change in absorption coefficient but almost no change in scattering coefficient. So, we consider that spectral mining process erroneously accounted the change of spectral shape as the effect of scattering. $M_{a,1\text{-}3}$ and $M_{s,1\text{-}3}$ exhibit no change in their values, and $M_{s,7\text{-}9}$ value is not shown here since the proper representation of scattering in the deeper layers is difficult in the present approach.

To eliminate the effect of scattering in spectral mining, we again employed the customized database with μ_a-change only in the same way as the cuff occlusion experiment in Section 5.4. Figure 5.8(i) depicts the absorbing magnification factors M_a extracted from the μ_a-customized database for all 14 reflectance spectra measured in the

experiment. The μ_a-customized database rectifies the erroneous estimation of magnification factor $M_{a,4\text{-}9}$ obtained from the full-size database and provides reasonably estimated $M_{a,4\text{-}9}$ values (having a correlation coefficient of 0.956 with C_b), which are increased by 58% after the immersion and then gradually decreased by 53% with passing time, while estimated $M_{a,1\text{-}3}$ values have no change. This improvement in the estimated $M_{a,4\text{-}9}$ was probably made by a constraint that μ_a-customized database does not include any effect of changing scattering property in the simulated spectra. So, this μ_a-type customized database becomes more effective and useful in estimating the change of absorption coefficient or chromophore concentration than the full-size database.

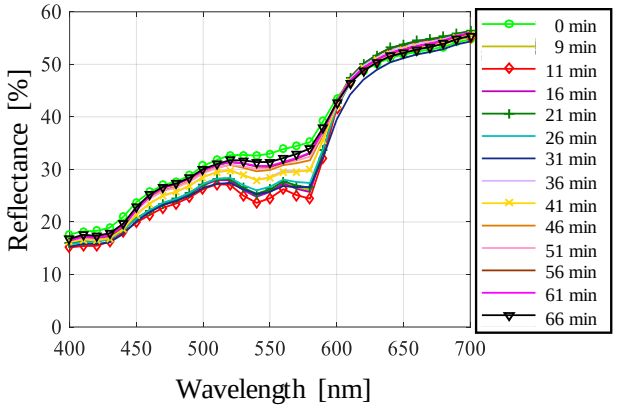

(a) Measured spectra

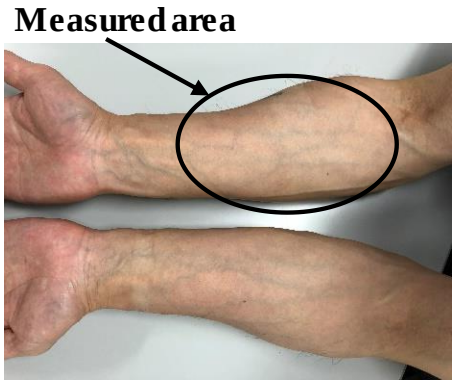

(d) Measuring forearm At t= 0min

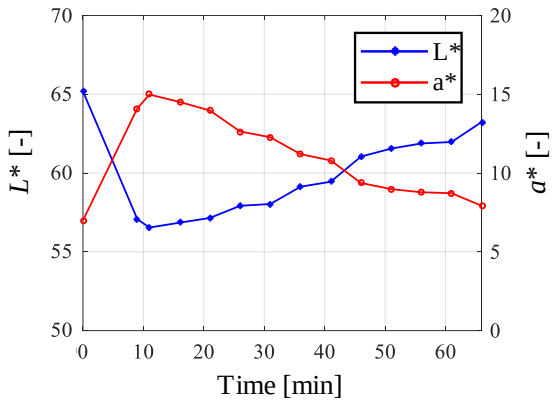

(b) Calculated L^* and a^* values

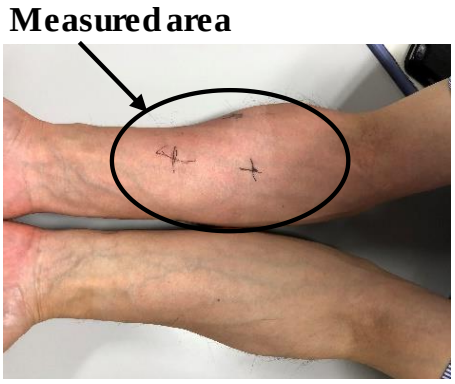

(e) Measuring forearm At t= 11min

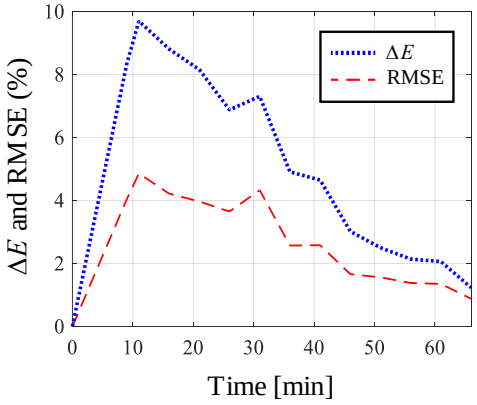

(c) ΔE and RMSE to the first spectrum

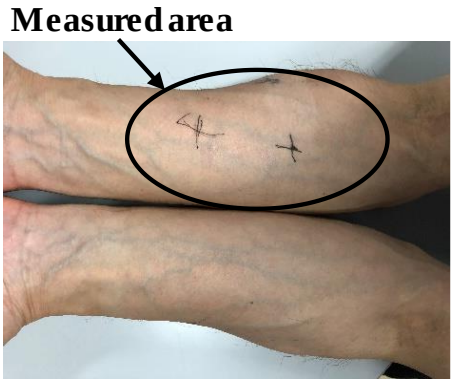

(f) Measuring forearm At t= 66min

Fig. 5.8 Results obtained by using MRA and spectral mining in the hot water immersion experiment.

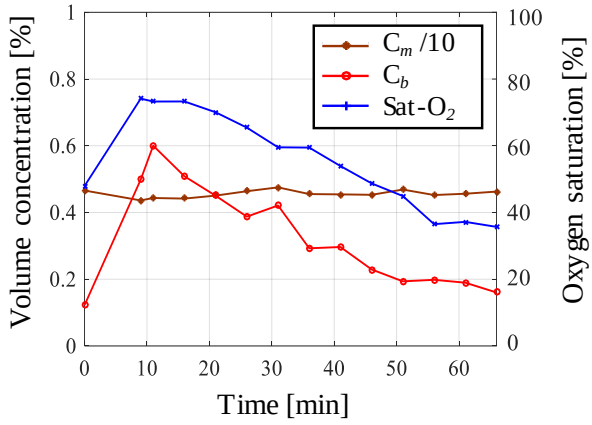

(g) Estimated C_m, C_b and Sat-O_2 by MRA

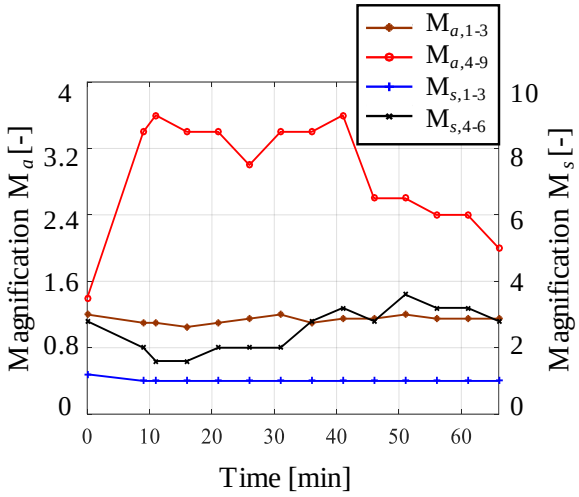

(h) Magnifications by full-size database

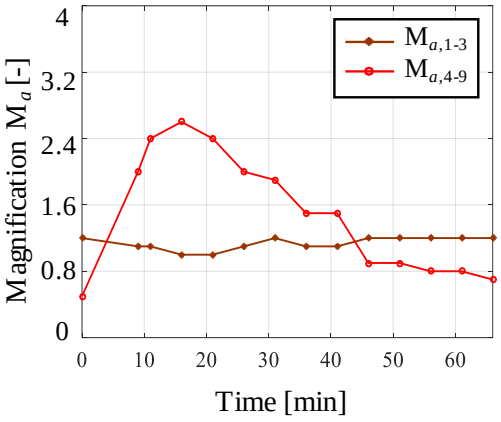

(i) Magnifications by customized database

Fig. 5.8 Results obtained by using MRA and spectral mining in the hot water immersion experiment.

In this chapter, we presented the possibility of estimating change of only absorbing condition due to blood concentration. However, in the near future we intend to do the same for change of melanin concentration and also scattering condition as well. Our spectral mining from the database is capable of estimating unknown parameters of measured spectra with moderate accuracy using both the full-size and customized database, for the case where change of skin condition is distinguished between absorption

and scattering. However, for measured spectra without distinction, estimated parameters may include some erroneous data due to the ambiguity present in the full-size database. So, the ambiguity problem is yet to be solved by detailed investigation of spectral change, which will be performed intensively in the near future.

5.6 Conclusion

We have described the method of spectral classification and spectral mining using the database and validated its possibility to detect change of absorption in skin tissue through the experiments with agarose-gel type skin phantom and on human forearm. We also proposed the effectiveness of μ_a-type customized database for detecting the change of absorption property for measured spectra with less influence by scattering effect. The extracted parameters from the database showed expectable tendency in accordance with experimental conditions. The results also agree with temporal response of skin parameters obtained from the MRA. For target-known application such as changing of pigment concentration, the present method can reasonably detect the change of parameters. However, error may occur for general application due to the ambiguity problem. Therefore, we continue to solve this subject with proper justification and reliability. We should also investigate usefulness of the method for estimating changes of melanin concentration and scattering property in the near future. The database approach has flexibility in its own extension of contained spectral data and simplicity in determination of probable skin change. In this respect, we consider that the present method is advantageous for future development of on-line skin inspection. We expect that for such

on-line skin inspection, from uploading measured spectrum to downloading skin parameter information, the whole process can be executed under a minute considering the current size for both the original and customized databases.

Chapter 6

Concluding Remarks

The present dissertation has been dedicated towards the evaluation of optical parameters of measured spectra using spectral mining in spectral reflectance database. Chapter 2 was devoted to the description of fundamental theories and principles treated through this dissertation. The constitution of biological tissue has been presented in Section 2.2. The algorithm of the Monte Carlo simulation for the light transport in tissue has been mentioned in Section 2.5. In Section 2.7, details of the layered skin model have been discussed. Spectral database is introduced in section 2.8. The composition of the skin tissue phantom used for experiments in Chapter 5 has been referred in Section 2.9. Chapter 3 described the importance of appropriate aperture size for detection through simulative and experimental works. Chapters 4 and 5 consist of investigation of the proposed database method. In chapter 4, the construction and numerical validation of the database method has been discussed. Chapter 5 conveyed the experimental validation of the database method to exhibit its usefulness.

Chapter 3 dealt with the effect of detection area for measurement of spectral reflectance. In this chapter, we describe how a reduced or inappropriate detection area can influence spectral reflectance. This has been investigated by Monte Carlo simulation and experiments on human skin tissue using an integrating sphere. Section 3.3 highlighted the numerical investigation, in which different illumination sources (point-like and circular illuminations) are used to clarify the effect of the detection aperture in different size through simulated reflectance spectra and photon fluence map in skin tissue model.

Also, in the same section, the longer wavelength of light penetrates deeper in a tissue model producing broadening of diffuse light is reported. Section 3.4 confirmed the numerical findings through the experiment on human forearm skin, in which a reduced detecting aperture size resulted in significant decrease of spectral reflectance in the wavelength range larger than 600nm. All these results indicated that an appropriate detection aperture probably calculated by sum of an illumination spot size and a detection margin of 4 to 6mm which generates from the broadening of diffused light.

Chapter 4 is allotted to the estimation of optical property, mainly absorption and scattering coefficients of a certain measured spectrum. Here, in order to do so, use of database constructed with simulated spectral reflectance has been proposed, in which the most reasonable simulated spectrum is extracted out with a criterion of root mean square error. In Section 4.3.2, construction of database is explained in details, where moderate grouping for varying absorption coefficients (in two groups) and scattering coefficients (in three groups) with fixed thickness, refractive index and anisotropy scattering parameter is introduced. This resulted in a convenient and simple way to build a database with keeping the advantage of nine-layered skin tissue model. Section 4.3.3 presented the performance of the constructed database by numerical validation experiments which indicated efficiency of the database to appropriately estimate absorption and scattering coefficients, except for the scattering coefficients in deeper layers due to multiple scattering experienced by photons in longer path lengths. Section 4.3.4 mentioned the use of point spread function of reflected intensity on the skin surface, to counter the ambiguity in the database which occurs as some different conditions of absorption and scattering coefficients in dermal layer produced similar simulated spectra. Point spread function showed varying slope for changing scattering coefficients in dermal layer but not for

changing absorption coefficients in dermal layer which conveyed its effectiveness in identification of ambiguity present in the database.

Chapter 5 extended the study conducted in Chapter 4. As in Chapter 4 moderate grouping of absorption and scattering coefficients resulted in five types of spectral change in the database, in Section 5.2.2 of Chapter 6 the applicability of types of spectral change in spectral mining to extract the most nearer simulated spectrum from spectral reflectance database has been discussed. Also, these types of spectral change are validated from five types of spectral change in measured spectra from agarose-gel phantom, described in section 5.3. In Sections 5.4 and 5.5 pressure-cuff occlusion and hot water immersion experiments are carried out, which confirms the effectiveness of the database method to evaluate change of absorption property in measured spectra, as under the experimental condition absorption property in dermal and subcutaneous layers are expected to alter. The results of the database method also compared with multiple regression analysis method, which conveyed good resemblance. To counter the ambiguity problem in database (full size or both absorption and scattering coefficients are varying), use of application based customized database (for this study only varying absorption property) is introduced, as measurement of point spread function is unreliable and has many limitations.

As shown in the present dissertation, the spectral mining from spectral reflectance database method has the ability to evaluate optical property of skin tissue in real time, which enable it to analyze skin condition changes. Thus, it has the potential to become a diagnostic tool for clinician. The proposed database approach has flexibility in its own expansion of contained spectral data and simplicity in determination of probable changes in skin condition. The author expects that the results obtained in this dissertation will

provide new possibilities for development of non-invasive, affordable and dependable biomedical instrumentations in practical situations.

Appendix

A.1 Molar Extinction Coefficients of Hemoglobin

Tabulated Molar Extinction Coefficient for Hemoglobin in Water

These values for the molar extinction coefficient ε [cm-1/(moles/liter)] were compiled by

S. A. Prahl, Oregon Medical Laser Center, Portland.

λ (nm)	ε_{Hb02} (cm^{-1}/M)	ε_{Hb} (cm^{-1}/M)
400	266232	223296
410	466840	303956
420	480360	407560
430	246072	528600
440	102580	413280
450	62816	103292
460	44480	23388.8
470	33209.2	16156.4
480	26629.2	14550
490	23684.4	16684
500	20932.8	20862
510	20035.2	25773.6
520	24202.4	31589.6
530	39956.8	39036.4
540	53236	46592
550	43016	53412
560	32613.2	53788
570	44496	45072
580	50104	37020
590	14400.8	28324.4
600	3200	14677.2
610	1506	9443.6
620	942	6509.6
630	610	5148.8
640	442	4345.2
650	368	3750.12
660	319.6	3226.56
670	294	2795.12
680	277.6	2407.92
690	276	2051.96
700	290	1794.28
710	314	1540.48
720	348	1325.88
730	390	1102.2
740	446	1115.88
750	518	1405.24
760	586	1548.52
770	650	1311.88
780	710	1075.44
790	756	890.8
796.8	794.72	794.72
800	816	761.72
810	864	717.08
820	916	693.76
830	974	693.04
840	1022	692.36
850	1058	691.32
860	1092	694.32
870	1128	705.84
880	1154	726.44
890	1178	743.6
900	1198	761.84

A.2 Scattering Coefficients of Hemoglobin

Scattering Coefficients of Hemoglobin

These values for the scattering coefficients of hemoglobin (Hct=45%) μs [cm-1] by

A. Roggan, M. Friebel, K. Dorschel, A. Hahn, and G. Muller,

“Optical Properties of Circulating Human Blood in the Wavelength Range 400-2500 nm.”

λ (nm)	μ_s (cm^{-1})
380	404.9005941
390	384.9863807
400	365.0721673
410	352.251562
420	423.7620887
430	547.9355277
440	653.7461703
450	793.7331961
460	816.556118
470	789.513794
480	885.9076687
490	924.6111993
500	939.3893184
510	864.5980921
520	815.4556114
530	731.2141063
540	714.6073616
550	682.1136629
560	679.6045077
570	650.1872705
580	631.7798589
590	665.138298
600	639.534366
610	637.2597872
620	620.9552357
630	626.5880452
640	632.2208547
650	630.0781385
660	627.030429
670	616.057287
680	614.6948399
690	611.0647542
700	612.0373642
710	612.8444024
720	609.867284
730	603.567032
740	594.5956224
750	595.2939979
760	595.9923735
770	586.3907999
780	576.5524685
790	570.3579049
800	582.0101885
810	572.7927015
820	568.503105
830	560.5667665
840	557.9289214
850	562.3604932
860	536.1938156
870	529.4371012
880	519.1470664
890	510.7039
900	498.664357

A.3 Absorption Coefficients of Melanosome

Absorption Coefficients of Melanosome in Epidermis

These values for the absorption coefficients of melanosome μ_a [cm-1] by

S. L. Jacques,

"Skin optics," Oregon Medical Laser Center Monthly news and articles on Biomedical Optics and Medical Lasers, http://omlc.ogi.edu/news/jan98/skinoptics.html, 1998.

λ (nm)	μ_a (cm^{-1})
400	1427.85519
410	1315.14516
420	1213.73478
430	1122.26128
440	1039.55273
450	964.59779
460	896.52077
470	834.56097
480	778.05557
490	726.42535
500	679.16269
510	635.82156
520	596.00898
530	559.37788
540	525.62101
550	494.46571
560	465.66951
570	439.01632
580	414.31315
590	391.38731
600	370.08397
610	350.26407
620	331.80247
630	314.58637
640	298.51394
650	283.49308
660	269.44035
670	256.28008
680	243.9435
690	232.36808
700	221.4968
710	211.27769
720	201.66323
730	192.60999
740	184.07818
750	176.03131
760	168.4359
770	161.26118
780	154.47881
790	148.06272
796.8	143.89665
800	141.98886
810	136.23504
820	130.78075
830	125.60701
840	120.69629
850	116.0323
860	111.59997
870	107.3853
880	103.37527
890	99.55778
900	95.92159

A.4 Scattering Coefficients of Epidermis and Dermis

Scattering Coefficients of Epidermis and Dermis

These values for the scattering coefficients of epidermis and dermis μs [cm-1] by

S. L. Jacques,

“Skin optics,” Oregon Medical Laser Center Monthly news and articles on Biomedical Optics and Medical Lasers, http://omlc.ogi.edu/news/jan98/skinoptics.html, 1998.

λ (nm)	M_s (cm^{-1})
400	390.625
410	363.3411
420	338.9208
430	316.99937
440	297.26636
450	279.45635
460	263.34173
470	248.72634
480	235.44091
490	223.33855
500	212.29166
510	202.18893
520	192.93294
530	184.43836
540	176.63008
550	169.4419
560	162.81535
570	156.69865
580	151.0458
590	145.81599
600	140.97272
610	136.48346
620	132.31923
630	128.45388
640	124.86409
650	121.52883
660	118.42932
670	115.54852
680	112.87106
690	110.38327
700	108.0726
710	104.19232
720	100.53299
730	97.07836
740	93.81345
750	90.72475
760	87.79972
770	85.02712
780	82.39644
790	79.89814
796.8	78.2704
800	77.52345
810	75.26424
820	73.11316
830	71.06328
840	69.10831
850	67.24232
860	65.46
870	63.75627
880	62.1265
890	60.56638
900	59.07186

A.5 Anisotropy Scattering parameter of Epidermis and Dermis

Anisotropy scattering parameter of epidermis and dermis

These values for the Anisotropy scattering parameter of epidermis and dermis

g [-] by M. J. C. van Gemert *et. al*., “Skin optics,” IEEE TRANSACTIONS ON BIOMEDICAL ENGINEERING,Vol. 36, No. 12 (1989)pp1146-1154.

λ (nm)	*g* (-)
400	0.736
410	0.7389
420	0.7418
430	0.7447
440	0.7476
450	0.7505
460	0.7534
470	0.7563
480	0.7592
490	0.7621
500	0.765
510	0.7679
520	0.7708
530	0.7737
540	0.7766
550	0.7795
560	0.7824
570	0.7853
580	0.7882
590	0.7911
600	0.794
610	0.7969
620	0.7998
630	0.8027
640	0.8056
650	0.8085
660	0.8114
670	0.8143
680	0.8172
690	0.8201
700	0.823
710	0.8259
720	0.8288
730	0.8317
740	0.8346
750	0.8375
760	0.8404
770	0.8433
780	0.8462
790	0.8491
796.8	0.85107
800	0.852
810	0.8549
820	0.8578
830	0.8607
840	0.8636
850	0.8665
860	0.8694
870	0.8723
880	0.8752
890	0.8781
900	0.881

A.6 Molar Extinction Coefficients of melanin

These values for the molar extinction coefficient ε [cm-1/(moles/liter)] of melanin were compiled by

[1] S. L. Jacques, "Optical absorption of melanin," http://omlc.ogi.edu/spectra/melanin/index.html

[2] T Sarna, RC Sealy, Photoinduced oxygen consumption in melanin systems. Action spectra and quantum Yields for eumelanin and synthetic melanin. Photochem. Photobiol. 39:69-74, 1984.

[2] RP Crippa, V Cristofoletti, N Romeo, A band model for melanin deduced from optical absorption and photoconductivity experiments. Biochim. Biophys. Acta 538:164-170, 1978.

λ (nm)	ε_{Mel} (cm^{-1}/M)
400	2529.86223
410	2394.40817
420	2266.20659
430	2144.8692
440	2030.02846
450	1921.33653
460	1818.46419
470	1721.09985
480	1628.9486
490	1541.73132
500	1459.18383
510	1381.0561
520	1307.1115
530	1237.12604
540	1170.88775
550	1108.19599
560	1048.86088
570	992.7027
580	939.55134
590	889.24581
600	841.63375
610	796.57094
620	753.92088
630	713.55439
640	675.34921
650	639.18962
660	604.96608
670	572.57494
680	541.91809
690	512.90268
700	485.4408
710	459.4493
720	434.84943
730	411.56669
740	389.53056
750	368.67428
760	348.9347
770	330.25201
780	312.56964
790	295.83401

λ (nm)	ε_{Mel} (cm^{-1}/M)
800	279.99444
810	265.00296
820	250.81415
830	237.38504
840	224.67496
850	212.6454
860	201.25992
870	190.48405
880	180.28514
890	170.6323
900	161.49629

Acknowledgement

I would like to express my sincere gratitude towards Professor Y. Aizu for his valuable instruction and useful suggestions with profound supervision on all of the present work, and also I am indebted for his continuous guidance, much needed perspective, and encouragement throughout the present work, without which this dissertation would not have been possible. I wish to extend my appreciation to Associate Professor T. Yuasa and Associate Professor H. Funamizu for kind encouragement and useful discussions on the simulative study and imaging systems. Heartfelt acknowledgement extended to Associate Professor I. Nishidate of Tokyo University of Agriculture and Technology and Associate Professor T. Maeda of Kushiro National Collage of Technology for fruitful discussions and advices on skin optics, skin phantom and imaging. Also, I am grateful to all other members of the Instrumentation Systems Laboratory, Division of Production and Systems Engineering, Muroran Institute of Technology, for various supports with which the present dissertation has been successfully accomplished.

Kaustav Das

Bibliography

[1] S. Chandrasekhar, *Radiative Transfer*, Dover, New York (1960).

[2] A. Ishimaru, "Diffusion of a Pulse in Densely Distributed Scatterers," *J. Opt. Soc. Am.* **68**, 1045-1050 (1978).

[3] K. Furutsu, "On the Diffusion Equation Derived from the Space-Time Transport Equation," *J. Opt. Soc. Am.* **70**, 360-366 (1980).

[4] A. H. Gandjbakhche, G. H. Weiss, R. F. Bonner, and R. Nossal, *Phys. Rev.* **E48**, 810-818 (1993).

[5] *Special Issue on Lasers in Biology and Medicine*, IEEE J. Quantum Electr. vol. 20, (1342-1532); vol. 23, (1701-1855); vol. 26, 1990.

[6] *Special Issue on Optical Properties of Mammalian Tissues*, *Appl. Opt.* **28**, 2207-2357 (1989).

[7] M. J. C. van Gemert, S. L. Jacques, H. J. C. M. Sterenborg, W. M. Ster, "Skin optics," *IEEE Trans. Biomed. Eng.* **36**, 1146-1154 (1989).

[8] M. J. C van Gemert and W. M. Ster, "Relations between the Kubelka-Munk and the transport equation models for anisotropic scattering," *Lasers in Life Science* **1**, 287-298 (1987).

[9] A. J. Welch, G. Yoon, M. J. C. van Gemert, "Practical models for light distribution in laser-irradiated tissue," *Laser in Surgery and Medicine* **6** 488-493 (1987).

[10] S. A. Prahl, M. Keijzer, S. L. Jacques, and A. J. Welch, "A Monte Carlo model of light propagation in tissue," *SPIE Institute Series* **IS5**, 102-111 (1989).

[11] L.-H. Wang, S. L. Jacques and L.-Q. Zheng, "MCML-Monte Carlo modeling of

photon transport in multi-layered tissues," *Comput. Methods Programs Biomed.* **47**, 131-146 (1995).

[12] R. Arridge, M. Cope, and D. T. Delpy, *Phys. Med. Biol.* **37**, 1531-1560 (1992).

[13] B. Chance, J. S. Leigh, H. Miyake, D. S. Smith, S. Nioka, R. Greemfeld, M. Finander, K. Kaufman, W. Levy, M. Young, P. Cohen, H. Yoshioka, and R. Boretsky, "Comparison of time-resolved and -unresolved measurements of deoxyhemoglobin in brain," *Proc. Natl. Acad. Sci.* (USA) **85**, 4871-4975 (1988).

[14] D. T. Delpy, M. Cope, P. van der Zee, S. R. Arridge, S. Wray, and J. Wyatt, "Estimation of optical pathlength through tissue from direct time of flight measurement," *Phys. Med. Biol.* **33**, 1433-1442 (1988).

[15] B. Wilson, Y. Park, Y. Hefetz, M. Patterson, S. Madsen, and S. Jacques, "The potential of time-resolved reflectance measurements for noninvasive determination of tissue optical properties," in *Thermal and Optical Interactions with Biological and Related Composite Materials*, M. J. Barry and G. M. Harpole, eds., *Proc. Soc. Photo-Opt, Instrum. Eng.* **1064**, 97-106 (1989).

[16] Y. Nomura, O. Hazeki, and M. Tamura, "Exponential attenuation of light along nonlinear path through the biological model," *Adv. Exp. Med. Biol.* **248**, 77-80 (1989).

[17] M. S. Patterson, B. Chance, and B. C. Wilson, "Time resolved reflectance and transmittance for the non-invasive measurement of tissue optical properties," *Appl. Opt.* **28**, 2331-2336 (1989).

[18] Y. Hasegawa, Y. Yamada, M. Tamura, and Y. Nomura, "Monte Carlo simulation of light transmission through living tissues," *Appl. Opt.* **30**, 4515-4520 (1991).

[19] S. L. Jacques, "Time resolved propagation of ultrashort laser pulses within turbid

tissues," *Appl. Opt.* **28**, 2223-2229 (1989).

[20] Y. Ito, I, Oda, M. Takada, T. Kubodera, K. Nagai, H. Nakagawa, and M. Tamura, "An experiment of light beam computed tomography," in *Proceedings of the Second International Near Infrared Soectroscopy Conference*, M. Iwamoto and S. Kawama, eds. (Korin, Tokyo, 1989), pp.305-312.

[21] R. Araki and I. Nashimoto, "Near-infrared imaging *in vivo*: imaging of Hb oxygenation in living tissues, in *Time-Resolved Spectroscopry and Imaging of Tissues*, B. Chance and A. Katzer, eds., Proc. Soc. Photo-Opt. Instrum. Eng. **1431**, 321-332 (1991).

[22] S. R. Arridge, P. van der Zee, M. Cope, and D. T. Delpy, "Reconstruction methods for infra-red absorption imaging," in *Time-Resolved Spectroscopry and Imaging of Tissues*, B. Chance and A. Katzer, eds., *Proc. Soc. Photo-Opt. Instrum. Eng.* **1431**, 204-215 (1991).

[23] J. R. Singer, F. A. Grünbaum, P. Kohn, and J. P. Zubelli, "Image reconstruction of the interior of bodies that diffuse radiation," *Science* **248**, 990-993 (1990).

[24] Y. Yamada and Y. Hasegawa, "Simulation of time-resolved optical-CT imaging," in *Time-Resolved Spectroscopry and Imaging of Tissues*, B. Chance and A. Katzer, eds., *Proc. Soc. Photo-Opt. Instrum. Eng.* **1431**, 73-82 (1991).

[25] Y. Yamada, Y. Hasegawa, and Y. Yamashita, "Simulation of fan-beam-type optical computed-tomography imaging of strongly scattering and weakly absorbing media," *Appl. Opt.* **32**, 4808-4814 (1993).

[26] S. J. Madsen, E. R. Anderson, R. C. Haskell, and B. J. Tromberg, "Portable high-bandwidth frequency-domain photon migration instrument for tissue spectroscopy," *Opt. Lett.* **19**, 1934-1936 (1994).

[27] B. J. Tromberg, L. O. Svaasand, T. Tsay, and R. C. Haskell, "Properties of photon density waves in multiple-scattering media," *Appl. Opt.* **32**, 607-616 (1993).

[28] J. B. Fishkin, P. T. C. So, A. E. Cerussi, S. Fantini, M. A. Franceschini, and E. Gratton, "Frequency-domain method for measuring spectral properties in multiple-scattering media: methemoglobin absorption spectrum in a tissuelike phantom," *Appl. Opt.* **34**, 1143-1155 (1995).

[29] S. Fantini, M. A. Franceschini, J. B. Fishkin, B. Barbieri, and E. Gratton, "Quantitative determination of the absorption spectra of chromophores in strongly scattering media: a light-emitting-diode-based technique," *Appl. Opt.* **33**, 5204-5213 (1994).

[30] M. S. Patterson, J. D. Moulton, B. C. Wilson, K. W. Berndt, and J. R. Lakowicz, "Frequency-domain reflectance for the determination of the scattering and absorption properties of tissue," *Appl. Opt.* **30**, 4474-4476 (1991).

[31] J. B. Fishkin, S. Fantini, M. J. vandeVen, and E. Gratton, "Gigaherz photon density waves in a turbid medium: theory and experiments," *Phys. Rev.* **E53**, 2307-2319 (1996).

[32] J. B. Fishkin, O. Coquoz, E. R. Anderson, M. Brenner. And B. J. Tromberg, "Frequency-domain photon migration measurements of normal and malignant tissue optical properties in a human subject," *Appl. Opt.* **36**, 10-20 (1997).

[33] R. A. J. Groenhuis, H. A. Frewerda, and J. J. T. Bosch, "Scattering and absorption of turbid materials determined from reflection measurements. 1: Theory," *Appl. Opt.* **22**, 2456-2462 (1983).

[34] R. A. J. Groenhuis, J. J. T. Bosch, and H. A. Frewerda, "Scattering and absorption of turbid materials determined from reflection measurements. 2: Measuring

method and calibration," *Appl. Opt.* **22**, 2463-2467 (1983).

[35] J. M. Schmitt, G. X. Zhou, E. C. Walker, and R. T. Wall, "Multilayer model of photon diffusion in skin," *J. Opt. Soc. Am.* **A7**, 2141-2153 (1990).

[36] B. C. Wilson, T. J. Farrell, and M. S. Patterson, "An optical fiber-based diffuse reflectance spectrometer for non-invasive investigation of photodynamic sensitizers *in vivo*," *Proc. SPIE* **IS6**, 319-231 (1990).

[37] T. J. Farrell, M. S. Patterson, and B. C. Wilson, "A diffusion theory model of spatially resolved, steady-state diffuse reflectance for the noninvasive determination of tissue optical properties *in vivo*," *Med. Phys.* **19**, 879-888 (1992).

[38] R. A. Bolt and J. J. ten Bosch, "Measuring position-dependent volume reflection," *Appl. Opt.* **32**, 4641-4645 (1993).

[39] R. A. Bolt and J. J. ten Bosch, "On the determination of optical parameters for turbid materials," Wave Random Media **4**, 233-242 (1994).

[40] S. L. Jacques, A. Gutsche, J. Schwartz, L. Wang, and F. K. Tittel, "Video reflectometry to extract optical properties of tissue *in vivo*," in *Medical Optical Tomography: Functional Imaging and Monitoring*, G. Muller, B. Chance, R. R. Alfano, S. A. Arridge, J. Beuthan, E. Gratton, M. Kaschke, B. R. Masters, S. Svanberg, and P. van der Zee, vol. ISII of SPIE Institute Series (Society of Photo-Optical Instrumentation Engineers, Bellingham, Wash., 1993), pp. 211-226.

[41] R. Splinter, G. A. Nanney, L. Littmann, c. H. Chuang, R. H. Svenson, J. R. Tuntelder, and G. P. Tatsis, "Monitoring tissue optical characteristics *in situ* using a CCD camera," *Laser Life Sci.* **6**, 15-25 (1994).

[42] M. Dogariu and T. Asakura, "Reflectance properties of finite-size turbid media," *Waves Random Media* **4**, 429-439 (1994).

[43] A. Kienle, L. Lilge, M. S. Patterson, R. Hibst, R. Steiner, and B. C. Wilson, "Spatially resolved absolute diffuse reflectance measurements for noninvasive determination of the optical scattering and absorption coefficients of biological tissue," *Appl. Opt.* **35**, 2304-2314 (1996).

[44] L. Wang and S. L. Jacques, "Use of a laser beam with an oblique angle of incidence to measure the reduce scattering coefficient of a turbid medium," *Appl. Opt.* **34**, 2362-2366 (1995).

[45] S. P. Lin, L. Wang, S. L. Jacques, and F. K. Tittel, "Measurement of tissue optical properties by the use of oblique-incidence optical fiber reflectometry," *Appl. Opt.* **36**, 136-143 (1997).

[46] E. A. Edwards and S. Q. Duntley, "The pigments and color of living human skin," *Am. J. Anat.* **65**, 1-33 (1939).

[47] H. E. Kuppenheim *et al.*, "Spectral reflectance of white and Negro skin between 440-1000 nm," *J. Appl. Physiol.* **4**, 800-806 (1952).

[48] R. R. Anderson and J. A. Parrish, "The optics of human skin," *J. Invest. Dermatol.* **77** 13-19 (1981).

[49] J. W. Feather, M. Hajizadeh-Saffar, G. Leslie, and J. B. Dawson, "A portable scanning reflectance spectrophotometer using visible wavelengths for the rapid measurement of skin pigments," *Phys. Med. Biol.* **34**, 807-820 (1989).

[50] B. L. Diffey, R. J. Oliver, and P. M. Farr, "A portable instrument for quantifying erythema induced by ultraviolet radiation," *Br. J. Dermatol.* **111**, 663-672 (1984).

[51] J. B. Dawson, D. J. Barker, E. Grassam, J. A. Cotterill, G. W. Fisher, and J. W. Feather, "A theoretical and experimental study of light absorption and scattering by *in vivo* skin," *Phys. Med. Biol.* **25**, 695-709 (1980).

[52] D. K. Harrison, S. D. Evans, N. C. Abbot, J. S. Beck, and P. T. McCollum, "Spectrophotometric measurements of haemoglobin saturation and concentration in skin during the tuberculin reaction in normal human subjects," *Clin. Phys. Physiol. Meas.* **13**, 349-363 (1992).

[53] R. Marchesini, M. Brambilla, C. Clemente, M. Maniezzo, A. E. Sichirollo, A. Testori, D. R. Venturoli, and N. Cascinelli, "*In vivo* spectrophotometric evaluation of neoplastic and non-neoplastic skin pigmented lesions-I. Reflectance measurements," *Photochem. Photobiol.* **53**, 77-84 (1991).

[54] R. Marchesini, N. Cascinelli, M. Brambilla, C. Clemente, L. Mascheroni, E. Pignoli, A. Testori, and D. R. Venturoli, "*In vivo* spectrophotometric evaluation of neoplastic and non-neoplastic skin pigmented lesions-II. Discriminant analysis between nevus and melanoma," *Photochem. Photobiol.* **55**, 515-522 (1992).

[55] V. P. Wallace, D. C. Crawford, P. S. Mortimer, R. J. Ott, and C. B. Bamber, "Spectrophotometric assessment of pigmented skin lesion: methods and feature selection for evaluation of diagnostic performance," *Phys. Med. Biol.* **45**, 735-751 (2000).

[56] N. Tsumura, H. Haneishi and Y. Miyake. "Independent-component analysis of skin color image," *J. Opt. Soc. Am.* **A16**, 2169-2176 (1999).

[57] M. Shimada, Y. Masuda, Y. Yamada, M. Itoh. M. Takahashi and T. Yatagai, "Explanation of human skin color by multiple linear regression analysis based on the modified Lambert-Beer law," *Opt. Rev.* **7**, 348-352 (2000).

[58] M. Shimada, Y. Yamada, M. Itoh and T. Yatagai. "Melanin and blood concentration in human skin studied by multiple regression analysis: experiments," *Phys. Med. Biol.* **46**, 2385-2395 (2001).

[59] M. Shimada, Y. Yamada, M. Itoh and T. Yatagai. “Melanin and blood concentration in human skin studied by multiple regression analysis: assessment by Monte Carlo simulation,” *Phys. Med. Biol.* **46**, 2397-2406 (2001).

[60] Y. Nomura, O. Hazeki, M. Tamura, “Relationship between time-resolved and non-time-resolved Beer–Lambert law in turbid media” *Phys. Med. Biol*. **42**, 1009–22 (1997).

[61] Y. Nomura, O. Hazeki, M. Tamura, “Exponential attenuation of light along nonlinear path through the biological model” *Adv. Exp. Med*. Biol. **248**, 77–80 (1989).

[62] M. Hiraoka, M. Firbank, M. Essenpreis, M. Cope, S. R. Arridge, P. van der Zee, D. T. Delpy, “A Monte Carlo investigation of optical path length in inhomogeneous tissue and its application to near-infrared spectroscopy” *Phys. Med. Biol*. **38**, 1859–76 (1993).

[63] S. J. Matcher, M. Cope, D. T. Deply, “Use of the water absorption spectrum to quantify tissue chromophore concentration changes in near-infrared spectroscopy” *Phys. Med. Biol*. **38**, 177-196 (1993).

[64] E. Salomatina, B. Jiang, J. Novak, A. N. Yaroslavsky, “Optical properties of normal and cancerous human skin in the visible and near-infrared spectral range” *J. Biomed. Opt.* **11**(6), 064026 (2006).

[65] G. N. Stamatas, N. Kollias, “In vivo documentation of cutaneous inflammation using spectral imaging” *J. Biomed. Opt.* **12**(5), 051603 (2007).

[66] G. Zonios, A. Dimou, I. Bassukas, D. Galaris, A. Tsolakidis, E. Kaxiras, “Melanin absorption spectroscopy: new method for noninvasive skin investigation and melanoma detection” *J. Biomed. Opt*. **13**(1), 014017 (2008).

[67] M. Hirose, S. Toyota, N. Ojima, K. Ogawa-Ochiai, N. Tsumura, “Principal component analysis for surface reflection components and structure in facial images and synthesis of facial images for various ages” *Opt. Rev.* **24**, 517-528 (2017).

[68] R. Zhang, W. Verkruysse, B. Choi, J. A. Viator, B. Jung, L.O. Svaasand, G. Aguilar, J. S. Nelson, “Determination of human skin optical properties from spectrophotometric measurements based on optimization by genetic algorithms” *J. Biomed. Opt.* **10**(2), 024030 (2005).

[69] W. Verkruysse, R. Zhang, B. Choi, G. Lucassen, L. O. Svaasand, J. S. Nelson, “A library based fitting method for visual reflectance spectroscopy of human skin” *Phys. Med. Biol.* **50**, 57-70 (2005).

[70] C. Magnain, M. Elias, J. Frigerio, “Skin color modelling using the radiative transfer equation solved by the auxiliary function method” *J. Opt. Soc. Am. A* **24**(8), 2196-2205 (2007).

[71] C. Magnain, M. Elias, J. Frigerio, “Skin color modelling using the radiative transfer equation solved by the auxiliary function method: inverse problem” *J. Opt. Soc. Am. A* **25**(7), 1737-1743 (2008).

[72] F. H. Imai, N. Tsumura, H. Haneishi, Y. Miyake, “principal component analysis of skin color and its application to colorimetric color reproduction on CRT display and hard copy” *J. Imaging Sci. Technol*. **40**,422-30 (1996).

[73] I. Konishi, Y. Ito, N. Sakauchi, M. Kobayashi, Y. Tsunazawa, “A new optical image for hemoglobin distribution in human skin” *Opt. Rev.* **10**(6), 592-595 (2003).

[74] I. Nishidate, Y. Aizu, H. Mishina, “Estimation of melanin and hemoglobin in skin tissue using multiple regression analysis aided by Monte Carlo simulation” *J.*

Biomed. Opt. **9**, 700-710 (2004).

[75] I. Nishidate, A. Wiswadarma, Y. Hase, N. Tanaka, T. Maeda, K. Niizeki, Y. Aizu, "Non-invasive spectral imaging of skin chromophores based on multiple regression analysis aided by Monte Carlo simulation" *Opt. Lett.*, **36**, 3239-3241 (2011).

[76] J. Spigulis, I. Oshina, A. Berzina, A. Bykov, "Smartphone snapshot mapping of skin chromophores under triple-wavelength laser illumination" *J. Biomed. Opt*. **22**(9), 091508 (2017).

[77] B. Alberts, D. Bray, A. Johnson, J. Lewis, M. Raff, K. Roberts, and P. Walter, Essential Cell Biology, Garland Publishing, 1998.

[78] W. F. Lever and G. Schaumburg-Lever, Histopathology of the skin. J.B.Lippincott Company, seventh edition edition, 1990.

[79] D. Batisse, R. Bazin, T. Baldeweck, B. Querleux, and J. L. Leveque, "Influence of age on the wrinkling capacities of skin," Skin Research and Technology, 8, 148–154 (2002).

[80] S. Akazaki, H. Nakagawa, H. Kazama, O. Osanai, M. Kawai, Y. Takema, and G. Imokawa, "Agerelated changes in skin wrinkles assessed by a novel three-dimensional morphometric analysis," British J. Dermat., 147, 689–695 (2002).

[81] K. Tsukahara, Y. Takema, T. Fujimura, S. Moriwaki, and M. Hattori, "Quantitative twodimensional analysis of facial wrinkles of japanese women at various ages," International Journal of Cosmetic Science, 24, 71–80 (2002).

[82] J. H. Chung, "Photoaging in asians," photodermatol Photoimmunol. Phtomed., 19, 109–121 (2003).

[83] J. S. Koh, H. Kang, S. W. Choi, and H. O. Kim, “Cigarette smoking associated with premature facial wrinkling: image analysis of facial skin replicas,” International Journal of Dermatology, 41, 21–27 (2002).

[84] R. R. Anderson and J. A. Parrish, The science of photomedicine Chapter 6: Optical properties of human skin. Plenum Press, 1982.

[85] A. R. Young, “Chromophores in human skin,” Physics in Medicine and Biology, 42, 789–802 (1997).

[86] S. L. Jacques, “Optical absorption of melanin,” Oregon Medical Laser Center Monthly news and articles on Biomedical Optics and Medical Lasers, http://omlc.ogi.edu/spectra/melanin/index.html, 1998.

[87] E. Angelopoulou, “The reflectance spectrum of human skin,” Tech. Note, University of Pennsylvania, 1999.

[88] S. L. Jacques, “Origins of tissue optical properties in the UVA, visible, and NIR regions,” Trends in Optics and Photonics: Advances in Optical Imaging and Photon Migration, 2, 364–371 (1996).

[89] S. L. Jacques, “Skin optics,” Oregon Medical Laser Center Monthly news and articles on Biomedical Optics and Medical Lasers, http://omlc.ogi.edu/news/jan98/skinoptics.html, 1998.

[90] S. L. Jacques, “Video imaging with polarized light finds skin cancer margins not visible to dermatologists,” Oregon Medical Laser Center Monthly news and articles on Biomedical Optics and Medical Lasers, http://omlc.ogi.edu/news/feb98/polarization/index.html, 1998.

[91] S. L. Jacques, “Scattering of polarized light by biological tissues,” Oregon Medical Laser Center Monthly news and articles on Biomedical Optics and

Medical Lasers, http://omlc.ogi.edu/news/oct99/saratov/index.htm, 1999.

[92] S. L. Jacques, C. A. Alter, and S. A. Prahl, “Angular dependence of HeNe laser light scattering by human dermis,” Lasers in the Life Science, 1, 309–333 (1987).

[93] S. L. Jacques and S. A. Prahl, “Modeling optical and thermal distributions in tissue during laser irradiation,” Lasers in Surgery and Medicine, 6, 494–503 (1987).

[94] S. L. Jacques, J. C. R. Roman, and K. Lee, “Imaging skin pathology with polarized light,” J. Biomed. Opt., 7, 329–340 (2002).

[95] M. Lees, Skin Care: Beyond the Basis, Milady, 2001.

[96] S. D. Cotton and E. Claridge, “Do all human skin colours lie on a defined surface within lms space?” Tech. Note CSR-96-1, School of Computer Science, The Univeristy of Birmingham, 1996.

[97] L. O. Olsen, H. Takiwaki, and J. Serup, “Skin thickness and echographic density of 22 anatomical sites,” Skin Research and Technology, 1, 74–82 (1995).

[98] M. Gniadecha and G. B. E. Jemec, “Quantitative evaluation of chronological ageing and photoageing in vivo: studies on skin echogenicity and thickness,” British J. Dermatol., 139, 815–821 (1998).

[99] M. Larsson, H. Nilsson, and T. Stromberg, “In vivo determination of local skin optical properties and photon path length by use of spatially resolved diffuse reflectance with applications in laser doppler flowmetry,” Appl. Opt., 42, 124–134 (2003).

[100] M. Denda and M. Takahashi, “Measurement of facial skin thickness by

ultrasound method," Journal of Society Cosmetic Chemists Japan, 23, 316–319 (1990).

[101] M. Ooe and H. Shiroshita, "The relationship between transparent skin and optical properties of stratum corneum," Fragrance Journal, 4, 38–44 (2002).

[102] P. T. Pugliese, Physiology of the Skin, chapter 1, page 1, Allured Publishing Corporation, 2001.

[103] A. F. Hood, T. H. Kwan, M. C. Mihm Jr., T. D. Horn, and B. R. Smoller, Primer of dermatopathology, Lippincott Williams & Wilkins, third edition, 2002.

[104] H. M. Sheu, S. C. Chao, T. W. Wong, Y. Y. Lee, and J. C. Tsai, "Human skin surface lipid film: an ultrastructural study and interaction with corneocytes and intercellular lipid lamellae of the stratum corneum," British J. Dermatol., 140, 385–391 (1999).

[105] R. W. G. Hunt "*Measuring Colour*," (Fountain Press, Kingston-upon-Thames, England, 1998) 3rd ed.

[106] G. Wyszecki and W.S. Stiles "*Color Science Concepts and Methods, Quantitative Data and Formulae*," (John Wiley & Sons, New York, 1982).

[107] R. A. Johnson and G. K. Bhattacharyya: Statistics Principles and Methods (Wiley, New York, 1996) 3rd ed.

[108] A. Ishimaru, "Wave Propagation and Scattering in Random Media" (Academic Press, New York, 1978) Vol. 1, Part II.

[109] E. Hecht "Optics," 2nd edn. (Addison & Wesley Publishing Company, Inc. 1987).

[110] L. G. Henyey and J. L. Greenstein, "Diffuse radiation in the galaxy," Astrophys. J. 93, 70-83 (1941).

[111] A. Roggan, M. Friebel, K. Dörschel, A. Hahn and G. Muller, “Optical properties of circulating human blood in the wavelength range 400-2500 nm,” J. Biomed. Opt. 4, 36-46 (1999).

[112] S. J. Dam, T. Dalgaard, P. E. Fabricius, and S. Andersson-Engels, “Multiple polynominal method for determination of biomedical optical properties from integrating sphere measurements,” Appl. Opt. 7, 1202-1209 (2000).

[113] M. J. van Gemert, J. W. Pickering, and A. J. Welch, “Modeling laser treatment of port-wine stains,” in Management and Treatment of Benign Cutaneous Vascular Lesions, O. T. Tan, ed. (Lea & Febiger, Philadelphia, 1992), pp. 24-47.

[114] J. M. Steinke and A. P. Shepherd, “Comparison of Mie theory and the light scattering of red blood cells,” Appl. Opt. 27, 4027-4033 (1988).

[115] T. Sarna and R. C. Sealy, “Photoinduced oxygen consumption in melanin systems. Action spectra and quantum yields for eumelanin and synthetic melanin,” Photochem. Photobiol. 39, 69-74 (1984).

[116] R. P. Crippa, V. Cristofoletti and N. Romeo, “A band model for melanin deduced from optical absorption and photoconductivity experiments,” Biochim. Biophys. Acta 538, 164-170 (1978).

[117] S. L. Jacques and D. J. McAuliffe, “The melanosome: threshold temperature for explosive vaporization and internal absorption coefficient during pulsed laser irradiation,” Photochem. Photobiol. 53, 769-775 (1991).

[118] S. L. Jacques, R. D. Glickman and J. A. Schwartz, “Internal absorption coefficient and threshold for pulsed laser disruption of melanosomes isolated from retinal pigment epithelium,” Proc. SPIE 2681, 468-477 (1996).

[119] S. Takatani and M. D. Graham, “Theoretical analysis of diffuse reflectance from

a two-layer tissue model," IEEE Trans. Biomed. Eng. BMF-26, 656-664 (1979).

[120] J. Parrish, R. Anderson, F. Urbach, and D. Pitts, "UVA" (Plenum, New York, 1978), p63.

[121] F. P. Bolin, L. E. Preuss, R. C. Taylor, and R. J. Ference, "Refractive index of some mammalian tissues using a fiber optic cladding method," Appl. Opt. 28, 2297-2303 (1989).

[122] T. Maeda, N. Arakawa, M. Takahashi, Y. Aizu: Monte Carlo simulation of spectral reflectance using a multilayered skin tissue model. Opt. Rev., 17 (2010) 223-229.

[123] I. V. Meglinski, S. J. Matcher, "Computer simulation of the skin reflectance spectra" *Comput. Methods Prog. Biomed*. **70**, 179-186 (2003).

[124] V. Tuchin, "Tissue Optics: Light Scattering Methods and Instruments for Medical Diagnosis" (*SPIE-The Internationa Society for Optical Engineering*, Washington DC), 2000, Chap **1**, p3.

[125] A. A. Stratonnikov, V. B. Loschenov, "Evaluation of blood oxygen saturation in vivo from diffuse reflectance spectra" *J. Biomed. Opt.* **6**, 457–467 (2001).

[126] T. Iwai, G. Kimura, "Imaging of an Absorbing Object Embedded in a Dense Scattering Medium by Diffusing Light Topography" *Opt Rev*, **7,** 436-441 (2000).

[127] I. Nishidate, Y. Aizu, and H. Mishina, "Estimation of absorbing components in a local blood layer embedded in the turbid media on the basis of visible to near-infrared (VIS-NIR) reflectance spectra," Opt. Rev. 10, 427-435 (2003).

[128] Y. Masuda, T. Yamashita, T. Hirao, M. Takahashi, "An innovative method to measure skin pigmentation" *Skin Research and Tech*. **15,** 224-229 (15).

[129] I. V. Meglinski, S. J. Matcher: Quantitative assessment of skin layers absorption

and skin reflectance spectra simulation in the visible and near-infrared spectral regions. Physiol. Meas., 23 (2002) 741-753.

[130] D. J. Newton, D. K. Harrison, C. J. Delaney, J. S. Beck, P. T. McCollum: Comparison of macro-and maicro-lightguide spectrophotometric measurements of microvascular haemoglobin oxygenation in the tuberculin reaction in normal human skin. Physiol. Meas. 15, 115–128 (1994).

[131] O. Hamdy, M. Fathy, T. A. Al-Saeed, J. El-Azab, N. H. Solouma: Estimation of optical parametres and fluence rate distribution in biological tissues via a single integrating sphere optical setup. Optik. 140, 1004-1009 (2017).

[132] D. Fukutomi, K. Ishii, K. Awazu: Determination of the scattering coefficient of biological tissue considering the wavelength and absorption dependence of the anisotropy factor. Opt. Rev. 23, 291-298 (2016).

[133] R. Ohtsuki. S. Tominaga, O. Tanno: Multiple-reflection model of human skin and estimation of pigment concentrations. Opt. Rev. 19(4), 254-263 (2012).

[134] K. Das, Y. Kobori, T. Hashisaka, T. Ohya, T. Yuasa, H. Funamizu, Y. Aizu: New library of spectral reflectance and point spread function developed by Monte Carlo simulation with nine-layered skin model. Proc. SPIE 11140, 1114001-202 (2019). doi:10.1117/12.2535451

[135] K. Das, Y. Kobori, T. Hashisaka, T. Ohya, T. Yuasa, H. Funamizu, Y. Aizu: Investigation of skin conditions producing similar reflectance spectra but different point spread functions in Monte Carlo simulation. Diffuse Optical Spectroscopy and Imaging VII, Proc. SPIE 11074, 110741W (2019). doi: 10.1117/12.2526716

[136] B. C. Wilson, G. Adam: A Monte Carlo model for the absorption and flux distributions of light in tissue. Med. Phys. 10, 824-830 (1983).

[137] R. F. Bonner, R. Nossal, S. Havlin, G. H. Weiss: Model for photon migration in turbid biological media J. Opt. Soc. Am. A 4, 423-432 (1987).

[138] M. Keijzer, S. L. Jacques, S. A. Prahl, A. J. Welch: Light distributions in artery tissue: Monte Carlo simulations for finite-diameter laser beams. Laser Surg. Med. 9, 148-154 (1989).

[139] S. T. Flock, M. S. Patterson, B. C. Wilson, D. R. Wyman: Monte Carlo modeling of light propagation in highly scattering tissue: I. Model predictions and comparison with diffusion theory. IEEE Trans. Biomed. Eng. 36, 1162-1168 (1989).

[140] I. V. Yaroslavsky, V. V. Tuchin: Light transport in multilayered scattering media. Monte Carlo modeling. Opt. Spectrosc. 72, 934-939 (1992).

[141] R. Graaff, A. C. M. Dassel, M. H. Koelink, F. F. M. De Mul, J. G. Aarnoudse, W. G. Zijlstra: optical properties of human dermis in vitro and in vivo. Appl. Opt. 32(4), 435-447 (1993).

[142] V. V. Tuchin: Laser light scattering in biomedical diagnostics and therapy. J. Laser Appl. 5(2,3), 43-60 (1993).

[143] V. V. Tuchin, S. R. Utz, I. V. Yaroslavsky: Tissue optics, light distribution, and Spectroscopy. Opt. Eng. 33(10), 3178-3188 (1994).

[144] D. Y. Churmakov, I. V. Meglinski, D. A. Greenhalgh: Amending of fluorescence sensor signal localization in human skin by matching of the refractive index. J. Biomed. Opt. 9(2), 339-346 (2004).

[145] R. Marchesini, A. Bertoni, S. Andreola, E. Melloni, A. E. Sichirollo: Extinction and absorption coefficients and scattering phase functions of human tissue in vitro. Appl. Opt. 28(12), 2318-2324 (1989).

[146] W. Cheong, S. A. Prahl, A. J. Welch: A review of the optical properties of biological tissues. J. Quantum Electron. 26(12), 2166-2185 (1990).

[147] G. Zonios, J. Bykowski, N. Kollias: Skin melanin, hemoglobin, and light scattering properties can be quantitatively assessed in vivo using diffuse reflectance spectroscopy. J. Invest. Dermatol. 117, 1452-1457 (2001).

[148] Y. Aizu, T. Maeda, T. Kuwahara, T. Hirao: Skin image reconstruction using Monte Carlo based color generation. Proc. SPIE 7851, 78510N (2010).

[149] Y. Aizu, T. Maeda, T. Kuwahara, T. Hirao: Spectral reflectance fitting based on Monte Carlo simulation using a multi-layered skin tissue model. SPIE Diffuse Optical Imaging III, Proc. SPIE 8088, 80880P (2011) [doi: 10.1117/12.889626].

[150] ISO/TR 16066:2003, Graphic technology - Standard object colour spectra database for colour reproduction evaluation (https://www.iso.org/standard/37358.html).

[151] K. Kawasaki, K. Yamanishi, H. Yamada: Age-related morphometric changes of inner structures of the skin assessed by in vivo reflectance confocal microscopy. Int. J. Dermatol. 54(3), 295-301 (2015) [doi: 10.1111/ijd.12220].

[152] Y. Ogura, K. Atsuta, E. Hase, T. Minamikawa, T. Yasui: Photonic-crystal-fiber-coupled, hand-held, polarization-resolved second-harmonic-generation microscope for in vivo visualization of dermal collagen fibers in human skin. IEEE Quant. Elec. 25(1), 6801007 (2019) [doi: 10.1109/JSTQE.2018.2865779].

[153] K. Das, T. Yuasa, I. Nishidate, H. Funamizu, Y. Aizu, “Simulated reflectance spectra and point spread functions in database constructed by moderate grouping of nine layers in skin model” *Opt. Rev.* **27**, 233–245 (2020).

[154] A. Mustari, I. Nishidate, Md. A. Wares, T. Maeda, S. Kawauchi, S. Sato, M. Sato,

Y. Aizu, “Agarose-based tissue mimicking optical phantoms for diffuse reflectance spectroscopy” *J. Vis. Exp.* **138**, e57578 (2018). [doi:10.3791/57578]

[155] R. Bezemer, A. Lima, D. Myers, E. Klijn, M. Heger, T. P. Goedhart, J. Bakker, C. Can Ince, “Assessment of tissue oxygen saturation during a vascular occlusion test using near- infrared spectroscopy: the role of probe spacing and measurement site studied in healthy volunteers” Critical Care. 13(5), S4 (2009).

List of Papers by the Author

[1] T. Yuasa, Y. Kobori, K. Das, T. Maeda, H. Funamizu, and Y. Aizu, “Effects of detection area on measurements of spectral reflectance in human skin tissue” *Asian J. Physics*. **27**, 9-12, 503-513 (2018).

[2] K. Das, T. Yuasa, I. Nishidate, H. Funamizu, Y. Aizu, “Simulated reflectance spectra and point spread functions in database constructed by moderate grouping of nine layers in skin model” *Opt. Rev.* **27**, 233–245 (2020).

[3] K. Das, T. Yuasa, T. Maeda, I. Nishidate, H. Funamizu, Y. Aizu, “Simple detection of absorption change in skin tissue using simulated spectral reflectance database” *Measurement* (Under review, 2020).